Max-Planck-Institut für Metallforschung
Stuttgart

Fatigue of Al Thin Films at Ultra High Frequencies

Christoph Eberl

Dissertation
an der
Universität Stuttgart

Bericht Nr. 160
Januar 2005

Fatigue of Al thin films at ultra high frequencies

Von der Fakultät für Chemie der Universität Stuttgart
zur Erlangung der Würde eines Doktors der
Naturwissenschaften (Dr. rer. nat.) genehmigte Abhandlung

Vorgelegt von

Dipl.-Ing. Christoph Eberl

aus Tübingen

Hauptberichter: Prof. Dr. phil. Eduard Arzt

Mitberichter: Prof. Dr. rer. nat. Oliver Kraft

Tag der mündlichen Prüfung: 13.12.2004

Institut für Metallkunde der Universität Stuttgart und
Max-Planck-Institut für Metallforschung Stuttgart

Stuttgart, Januar 2005

Danksagung

Index

Symbols

A_{elec}	cross sectional area	[m²]
α	thermal coefficient	[1/K]
b	burgers vector	[m]
$c_{disl.}$	velocity constant of dislocation process	[1/s]
$c_{extr.}$	velocity constant of extrusion growth mechanism	[1/s]
$c_{gb\_diff.}$	velocity constant of grain boundary diffusion mechanism	[1/s]
d	distance between cracks or voids	[m]
$D_{extr.}$	extrusion length distribution	[%]
D_{gb}	grain boundary diffusion coefficient	[m²/s]
D_{gb}^{0}	preexponential factor for GB-diffusion	[m²/s]
d_{grain}	grain size	[m]
E	Young's modulus	[Pa]
$\varepsilon_{a,tot}$	cyclic strain amplitude	[%]
Δf	frequency shift	[Hz]
f	frequency	[Hz]
f_0	excitation frequency	[Hz]
k	Boltzman constant $1.3807 \cdot 10^{-23}$	[J/K]
l_{elec}	electrode length	[m]
$l_{extr.}$	mean extrusion length	[m]
l_{gap}	distance between electrodes	[m]
λ	wave length	[m]
m_{elec}	electrode mass	[kg]
N	cycle number	[]
$n_{dislocations}$	number of dislocations	[]

4

$N_{extr.}$	number of extrusions	[]
N_f	cycle number to failure	[]
v_{climb}	dislocation climb velocity	[m/s]
v_{sound}	sound velocity	[m/s]
ρ_{el}^{spec}	specific resistivity	[Ohm·m]
P_{mean}	mean electrical power	[dBm] or [mW]
P_{short}	probability of a short circuit	[%]
Q_{gb}	activation energy for grain boundary diffusion	[eV]
ρ	material density	[kg/m³]
$\rho_{extr.}$	extrusion density	[1/m³]
$\rho_{void.}$	void density	[1/m³]
S_{12}	amplitude of the transfer-function	[dB]
σ	stress	[Pa]
σ_0	intrinsic film stress	[Pa]
σ_a	cyclic stress amplitude	[Pa]
σ_{crack}	stress at the crack	[Pa]
σ_n	stress normal to the GB	[Pa]
T	temperature	[K] or [°C]
T	experimental time	[s]
t_{cross}	time to cross a grain	[s]
t_f	film thickness	[m]
t_{load}	load time during experiment	[s]
τ_{xy}	cyclic shear stress in the xy-plane	[Pa]
τ_{yz}	cyclic shear stress in the yz-plane	[Pa]
w_{elec}	electrode width	[m]

CHRISTOPH EBERL:

FATIGUE OF AL THIN FILMS AT ULTRA HIGH FREQUENCIES

ABSTRACT: Ultra high-cycle fatigue at frequencies in the GHz regime leads to a characteristic void and extrusion formation in patterned metal thin films. Resulting from the microstructural damage formation a significant degradation in form of a shift of the resonance frequency and failures by short circuits in Surface Acoustic Wave (SAW) test devices take place. To study fatigue at ultra high cycles, SAW test devices were used to test continuous and patterned Al thin films at ultra high frequencies. For stress amplitudes as low as 14 MPa lifetime measurements showed no fatigue limit for 400 nm Al thin films. The resulting damage sites appeared in regions of cyclic stress concentration as identified by Finite Element Analysis. *In situ* measurements revealed that the characteristic extrusion/void formation mechanism operates on a short time scale. The post-test analysis of microstructural changes reveals extrusion and void formation concentrated at grain boundaries. This finding and the observed grain growth indicates a high material flux at the grain boundaries induced by the cyclic load. Quantitative analysis also shows a correlation between extrusion density and electrical devices performance. This direct correlation shows a functional agreement with a common theory on the influence of crack density on intrinsic stresses in thin metal films. Advanced Finite Element (FEM) calculations simulate very well the sensitivity of the resonance frequency to damage structure in interconnects such as cracks, voids and extrusions. The experimentally observed linear correlation between damage density and frequency shift is reproduced by the FEM model. The estimation of the short circuit probability from the extrusion length distribution revealed an exponential dependency on the electrode distance. The observed damage formation is explained by the combined action of dislocation motion and stress-induced diffusion processes.

FATIGUE OF AL THIN FILMS AT ULTRA HIGH FREQUENCIES

KURZZUSAMMENFASSUNG: Ermüdung in dünnen Metallschichten bei ultra-hohen Frequenzen (GHz) führt zu einer charakteristischen Poren- und Extrusionsbildung. Durch die mikrostrukturelle Schädigung kommt es zu einer messbaren Beeinträchtigung der Eigenschaften von Oberflächenwellen-(OFW)-Bauteilen, die sich in Form von Verschiebungen in der Resonanzfrequenz als auch in Form von Ausfällen durch Kurzschlüsse äußern. Um Ermüdung von strukturierten und unstrukturierten Al-Schichten (420 nm) bei ultra hohen Frequenzen zu untersuchen wurden OFW-Teststrukturen verwendet. Lebensdauermessungen mit diesen Schichten haben ergeben, dass selbst bei Spannungsamplituden von nur 14 MPa kein Ermüdungslimit auftritt. Der Vergleich mit Finiten Elemente Simulationen (FEM) zeigte, dass die resultierende Schädigung bevorzugt an den Stellen hoher zyklischer Spannungen zu finden ist. *In situ* Messungen haben gezeigt, dass die Bildung der Poren und Extrusionen innerhalb kurzer Zeit passiert. Die Mikrostrukturanalyse nach der Belastung zeigt, dass sich die Schädigung hauptsächlich an den Korngrenzen abspielt. Dieser Befund und das beobachtete Kornwachstum deuten auf einen starken Materialfluss an der Korngrenze hin. Quantitative Analysen der Schädigung haben gezeigt, dass die Defektdichte und die Verschiebung der Resonanzfrequenz direkt miteinander korrelieren. Dieser funktionelle Zusammenhang konnte mit einer Theorie, die sich mit dem Einfluss der Rissdichte auf intrinsische Spannungen in metallischen Schichten beschäftigt, erklärt werden. Um einen besseres Verständnis für den Spannungszustand in der Metallisierung und den Einfluss der unterschiedlichen Schädigungsstrukturen auf die Resonanzfrequenz der Bauteile zu bekommen, wurden FEM-Simulationen durchgeführt, die den Schädigungseinfluss sehr gut wiedergeben. Die beobachtete Schädigungsbildung kann anhand eines Modells, das auf der Kombination von Versetzungsbewegung und spannungsinduzierten Diffusionsprozessen basiert, erklärt werden.

1.   Introduction

Researching fatigue mechanisms in metals has a long tradition in material science. The key function of this research area is to prevent reliability issues in applications due to cyclic mechanic load [1, 2]. From all these studies it is well known that even if the cyclic stress amplitude is much lower than the flow stress of a metal, locally plastic deformation can be induced which leads to crack nucleation and growth. Thus in modern applications the prevention of fatigue is a well established target. The field of applications on which it is applied ranges from air plane wings to chip solderings or even Surface Acoustic Wave (SAW) devices and dimensions reach from some tens of meters to some micrometers, while the load frequency ranges from less than 1 Hz to some GHz. In this work ultra high cycle fatigue in SAW devices will be addressed.

SAW devices have been commercially used since the middle of the 80's as frequency filter devices for video and TV applications. Since the mid 90's they are commonly used in wireless applications such as mobile phones, bluetooth or wireless network devices and taking into account, that 2003 roughly 520 million mobile phones were sold worldwide [3], it is clear that their reliability has technical relevance nowadays. In these SAW frequency filter devices electromagnetic signals are transduced into acoustic waves on the surface of the piezoelectric substrate. At high electrical powers the acoustic wave can lead to a degradation of the metallization, which is used as electrode material, accompanied by a decrease in device performance [4]. As the damage formation is attributed to the cyclic mechanical stress induced by the acoustic wave and has a similar damage structure as observed in electromigration experiments, this effect is commonly called 'acoustomigration'.

Although intensive reliability evaluations of these devices are industrial standard, hardly anything is known about the fatigue mechanisms at ultra high frequencies. Since future communication devices demand more bandwidth and portability, a further increase in frequency and a reduction in device dimensions is required. This leads to a steady increase of the acoustic energy density in the metallizations and thus understanding the underlying mechanisms and correlation between microstructural changes and device performance gains in importance.

Aside from the technological challenges, SAW test devices offer an interesting playing ground for material science [4], as the stress conditions are rather enormous for the used metallization, especially compared to bulk fatigue experiments.

- The dimensions of the metallizations are limited by film thickness and feature size (e.g. electrode width) reaching from some micrometer down to some tens of nanometers. This has a significant impact on damage formation, as e.g. dislocation movement is inhibited and diffusion paths are short compared to bulk material.

- The mechanical load frequency in these devices reaches from several hundred MHz to some GHz, which is up to 10^5 times higher than in common fatigue tests. Therefore the time period of a load cycle is in the range of nanoseconds, in which the active defect mechanism has to interact with the external load.

- The cyclic stress state is rather inhomogeneous as it is induced by an acoustic wave on the surface of the substrate with a wave length which is equal to the pattern size. Thus the induced stress state has a significant gradient.

In this research work fatigue is studied at ultra high frequencies (900 MHz) by the use of SAW test devices with pure Al metallizations (film thickness 420 nm) on single crystalline piezoelectric 42°-y-cut LiTaO$_3$ substrates. The observed microstructural damage due to cyclic load will be interpreted by a model and correlated to the device performance and their influence on the reliability of SAW devices. In chapter 2 a literature overview and the motivation for this work will be given. In chapter 3 and 4 experimental observations will be presented and discussed. The focus of chapter 3 lies on *in situ* experiments which provide a better insight in the damage formation, while in chapter 4 the quantitative analysis of *ex situ* experiments will address the correlation between microstructural changes and device performance as well as the lifetime of pure Al metallizations. The correlation between damage structure and device performance will be discussed in depth in chapter 5 by the use of Finite Element simulations, and in chapter 6 a qualitative model will be presented which explains the observed damage formation due to the acoustic waves. Chapter 7 comprises the summary and conclusions.

2.   Literature review and motivation

In this chapter an introduction into the working principle of SAW test devices and the technological challenges will be presented. Next, an overview of literature concerning fatigue at ultra high frequencies and in thin films will be given. In the case of ultra high frequencies, the focus lies on the microstructural changes in SAW test devices and the resulting device degradation. The impact of the ultra high frequency and the limited dimensions on the active defect mechanisms will be discussed. Additional information can be found in the following chapters 3 to 6 as far as they were needed to discuss the experimental results.

2.1 Working principle of SAW test devices and material selection

Depending on the application different designs of SAW frequency filter devices are used. Nevertheless the working principle is always based on the transduction of a high frequency electromagnetic signal into an acoustic wave at the surface of a single crystalline piezoelectric substrate. This acoustic wave is induced by an interdigital transducer (IDT), which consists of two isolated metal comb structures gripping into each other (Fig. 2.1 a) [5]. A constant electric voltage induces an electric field between the electrodes of the two comb structures. Due to the inverse piezoelectric effect, the electric field leads to dilatation or shear deformation of the underlying piezoelectric substrate. The shape of the induced deformation depends on the induced electric field, which is determined by the geometry of the electrodes as well as by the piezoelectric coupling matrix and crystallographic orientation of the substrate. In the case of the 42°-y-cut $LiTaO_3$, which was used as substrate for this study, the electric field between the electrodes of the comb structures in x-direction primarily induces a shear strain in the xy-plane at the surface of the substrate (Fig. 2.1 b). An alternating voltage leads to an acoustic wave propagating in x-direction. The reflectors at each end of the device constrains the wave and the device acts like a resonator. The acoustic resonance frequency of the device depends mainly on the elastic properties and the density of the substrate and the metallization as well as on the geometry of the electrodes and the IDT. The material properties determine the velocity of the wave, while the pitch size of the comb structure

determines the wavelength. As the intrusion depth of a SAW lies roughly in range of one wavelength [4], the mass of the metallization on the substrate has a higher impact on the resonance frequency of the device than the Young's modulus. Thus, the resonance frequency of the device scales inversely with the film thickness of the metallization and the pitch size of the comb structure.
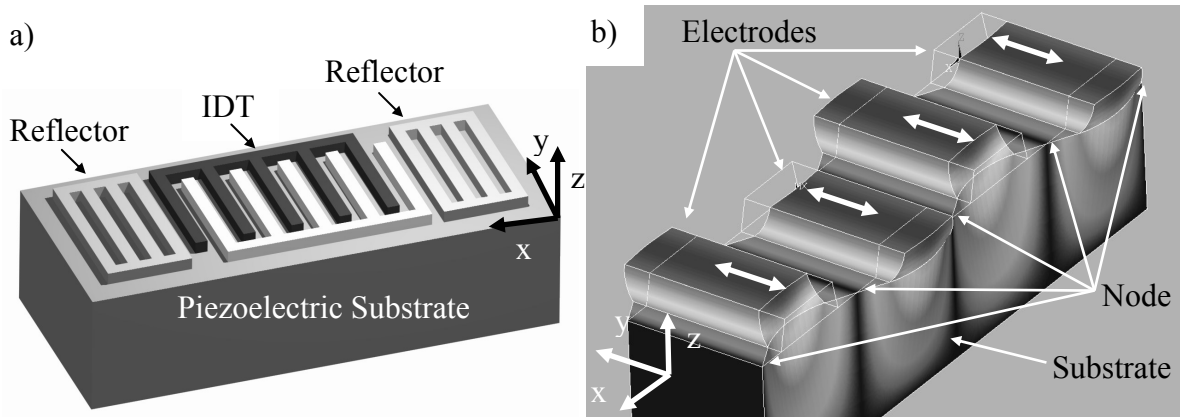
Fig. 2.1:   a) The Interdigital Transducer (IDT) consists of a patterned metal thin film on a piezoelectric substrate. The two comb structures of the IDT grip into each other and are flanked by two reflectors. b) FEM simulation of the cyclic displacement due to a standing surface wave in an IDT (chapter 5). The nodes of the standing surface wave are located between the electrodes while the highest deflection is sited in the middle of the fingers.

This explains why Al based alloys are the favorite metallizations for SAW devices: Although the electric conductivity of the metallization plays an important role for the material selection in frequency filter applications, the transition to Cu or Ag as electrode material would also increase the mass due to the higher material density. For a given design and substrate, the wave length is determined by the pitch size of the electrodes, while the velocity of the wave is primarily determined by the mass of the electrodes. Increasing the mass decreases the velocity of the acoustic wave, which decreases the frequency of the device. To provide the same mass per electrode, the thickness of the film has to be decreased, which in turn decrease the electrode conductivity of such a device.

The selection of Al as an ideal material can be substantiated by solving the optimization problem. While keeping the same electrode mass, width and length, the resistivity R should be reduced while the film thickness t_f can be changed. Thus the objective is to reduce the

electrodes resistance R, which depends on the specific resistivity ρ_{el}^{spec} of the material and the electrode dimensions:

$$R = \frac{\rho_{el}^{spec} \cdot l_{elec}}{A_{elec}} = \frac{\rho_{el}^{spec} \cdot l_{elec}}{w_{elec} \cdot t_f} \tag{2.1}$$

with w_{elec} is the width, l_{elec} is the length and t_f is the film thickness.

The constraint is that the mass of the electrode has to stay constant, otherwise the velocity of the wave would change. The mass of the electrode m_{elec} depends on the density of the material ρ and the geometry of the electrode:

$$m_{elec} = l_{elec} \cdot w_{elec} \cdot t_f \cdot \rho = const \, . \tag{2.2}$$

The free variable is the film thickness t_f, which can be eliminated by combining equation (8.1) and (8.2):

$$R = \underbrace{\left(\frac{l_{elec}^2}{m_{elec}} \right)}_{design} \cdot \underbrace{\rho_{el}^{spec} \cdot \rho}_{\substack{Material \\ selection}} \tag{2.3}$$

The optimization problem reveals that if we want to reduce the electrode resistance we have to minimize the resistivity of the material ρ_{spec} times the density of the material, ρ. The material selection map in Fig. 2.2 shows that Al seems to be the best candidate after Ca and Li for the metallization in SAW devices. As Ca and Li are rather reactive materials, its technological usage is inappropriate. Even though Cu and Ag have a higher conductivity, their density is too high to be a useful alternative. Therefore, Al based alloys can be regarded to be the best choice for SAW devices. Aside from the conductivity of the electrodes, the reproducibility of the film thickness in production is a challenge which gets harder to achieve as the film thickness is decreased. Therefore, film thickness should be maximized.
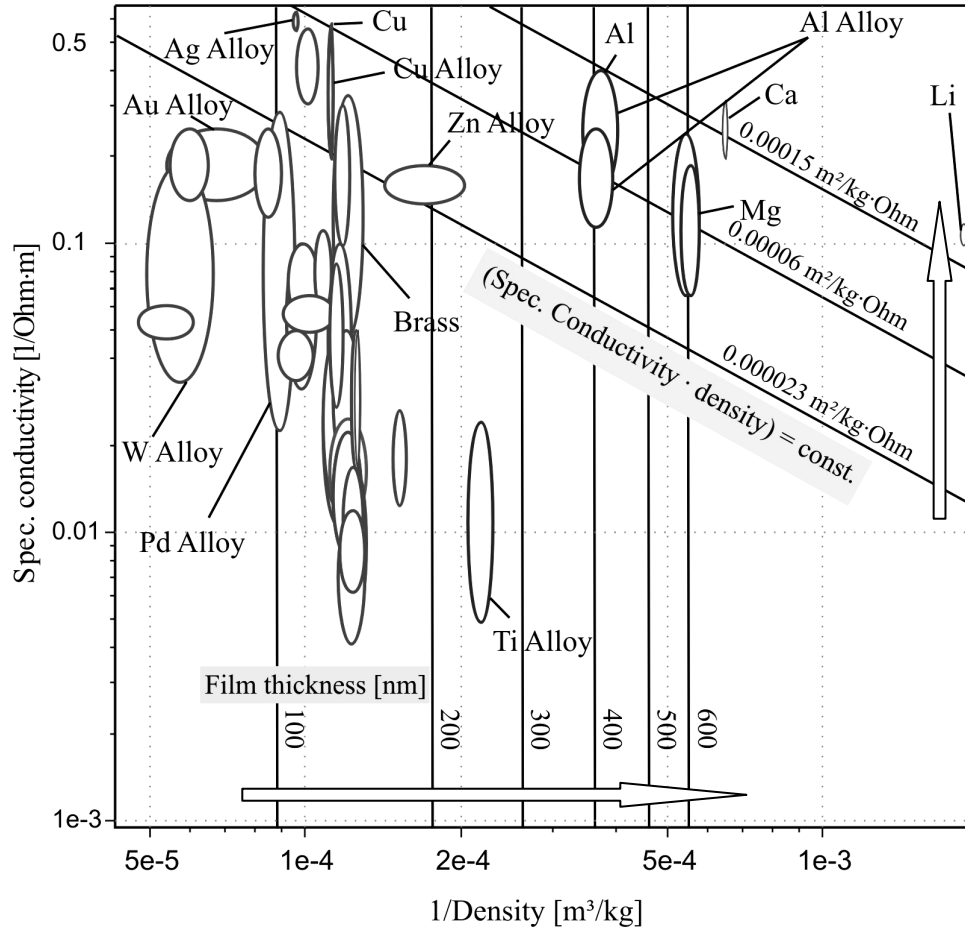
Fig. 2.2: From this material selection map (CES Selector, Granta Design, Cambridge, United Kingdom) the best material for SAW devices can be selected. The higher the value of the specific conductivity times the density is (diagonal lines), the more suitable is the material for a SAW device. The resulting film thickness (vertical lines) was calculated by the use of equation (8.2) for an electrode length $l_{elec} = 80$ µm, an electrode width of $w_{elec} = 1$ µm and a mass of $m_{elec} = 90.7 \cdot 10^{-12}$ g, which are typical values for an SAW test device working at roughly 1 GHz. The arrows point to better values.

2.2 Surface acoustic wave induced cyclic stress state

The acoustic wave on the surface of the piezoelectric substrate induces a cyclic mechanical stress in the metallization [4]. The induced stress state, though complex, will be explained briefly in this chapter and will be examined in depth in chapter 5. Due to the fact that SAW devices are mainly used as frequency filters, they are generally stressed at their resonance frequency. At the resonance frequency of such a device, a standing acoustic wave is stimulated between the reflectors. The Finite Element simulation in Fig. 2.1b shows how the substrate underneath the electrodes deforms cyclically in a sinusoidal manner due to the standing wave. In case of a patterned metallization the nodes of the standing surface wave are situated between the electrodes while the maximum deflection is sited at the center of the electrodes. During one cycle the electrodes move back and forth once in y-direction. Therefore the cyclic stress which is induced in the metallization on one hand results from the imposed deformation at the interface due to the sinusoidal deformation at the surface of the substrate and on the other hand from inertia forces in the electrode due to the cyclic movement as is shown in Fig. 2.1b. The inertia forces lead to a shear deformation of the electrodes as they are fixed at the interface to the substrate. This cyclic shear stress σ_{yz} is largest at the interface and zero at the top surface of the electrode. The deformation imposed by the substrate at the interface has mainly two stress components, namely σ_{yz} and σ_{xy} which are also largest at the interface. Combining all stress components, one finds that σ_{yz} is the stress component with the highest stress amplitude in the electrodes. The cyclic stress state at a certain site in the electrode depends on the location in x and z-direction and time [6, 7] and will be described in detail in chapter 5.

In the case of a continuous metallization, the inertia forces play a minor role and the highest shear stress can be found at the nodes of the acoustic wave. In this case, the σ_{xy} is the stress component with the highest amplitude [8]. As the wave length in the GHz regime is in the range of some μm, damage is localized at the nodes of the standing wave [9].

In both cases, patterned and continuous metallizations, the induced cyclic stress is purely deviatoric [6, 7, 8].

2.3 Microstructural changes in SAW devices

In SAW devices patterned Al thin film metallizations (ranging from some μm to several hundred nanometers in thickness) are mechanically fatigued at frequencies in the GHz regime, which induces characteristic damage in the metallization (Fig. 2.3a). Latham et al. [4] observed a significant number of dendrite-like out-growths on the surface of the metallization under the load of an acoustic wave at frequencies between 100-500 MHz. The material degraded on a short time scale and was accompanied by a frequency shift of the test frequency filter. Beside the hillock like extrusion formation, Shibagaki et al. [10] were able to observe the corresponding voids in the Al based metallization of SAW test devices (Fig. 2.3b).
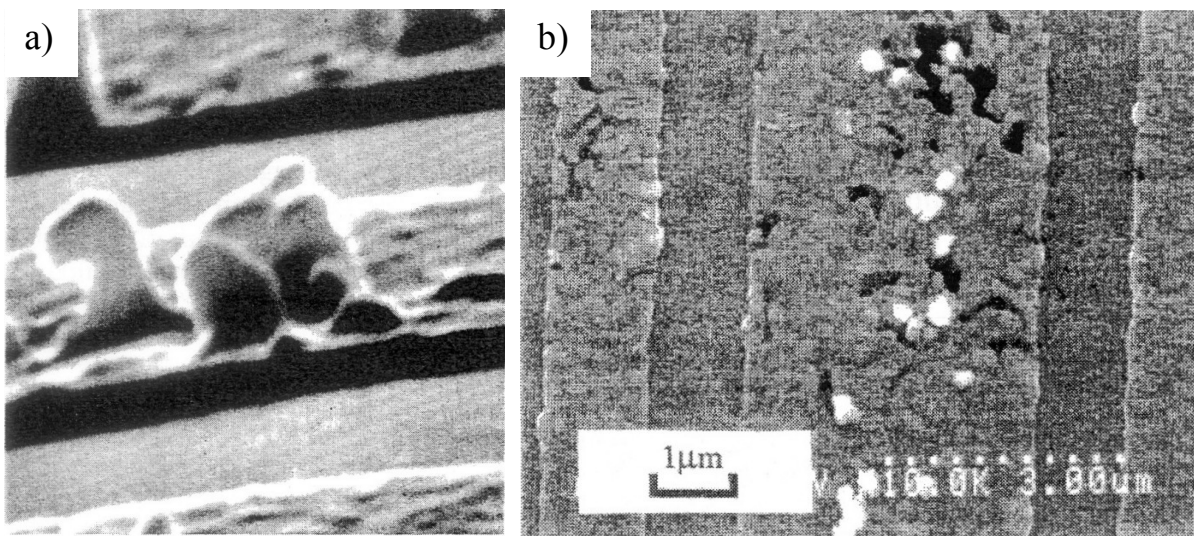
Fig. 2.3: SEM micrographs shows surface wave induced damage structures:
a) Extrusions in 130 nm thick Al electrodes of a SAW interdigitated transducer [4] (no micronbar available). b) Extrusions (bright spots) and voids (dark structures) in 100 nm thick Al electrodes [10].

The observed damage shape has a striking similarity to damage structures due to electromigration [11, 12] (Fig. 2.4), thermal fatigue in thin films [13] or thermal hillock formation [14] in Al thin films and line structures. Particularly as the induced cyclic stress state by the SAW can be purely deviatoric [8] the observed damage structure seems to be

confusing, as one would have expected a dislocation mechanism based plate like extrusion formation at the surface. Cross sections of the metallization show that the voids do not always reach through the whole metallization and can be invisible by top view SEM observations and that triple points can be possible origins for hillocks [15]. In Cu metallizations the dendrite-like out-growths do not occur, while the void formation and device degradation is also observed [16]. This is attributed to the natural closed oxide layer on the surface of Al which inhibits surface diffusion. Aside from the assumption that the required material transport in Al seems to be based on a diffusion process at the grain boundary [15], literature does not provide a consistent description of the degradation mechanisms at ultra high frequencies.
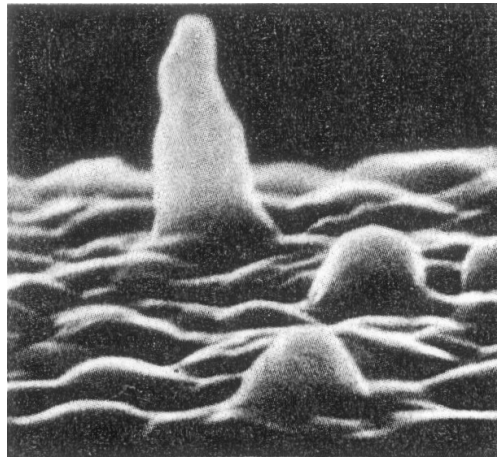
Fig. 2.4:   SEM micrograph of an extrusion due to electromigration in an Al thin film [12] (no micronbar available).

2.4 Technological challenges

From the technological point of view the damage formation in the metallization of SAW devices can lead to different failure types:

- *irreversible change of the resonance frequency* due to the degradation of the metallization [4],

- *short circuits* due to hillock-like extrusions, growing out of the side of neighboring electrodes leading to an immediate malfunction of the device [17] (Fig. 2.5),

- *increase of the insertion loss* (difference in amplitude between the in- and out-going signal) due to decreasing conductivity of the metallization during fatigue [10].

The technological challenge is to prevent these failures. Alloying of Cu to the Al metallization leads to a significant improvement in power durability of these devices. Thus a lot of work has been performed on different alloys [18, 19, 20], single crystalline films [21, 22] and multilayer systems [23, 24, 25, 26]. Nevertheless no experimental procedure was published which enables a quantitative analysis of the microstructural damage formation. Thus no study is known concerning the correlation between microstructural changes and device performance.
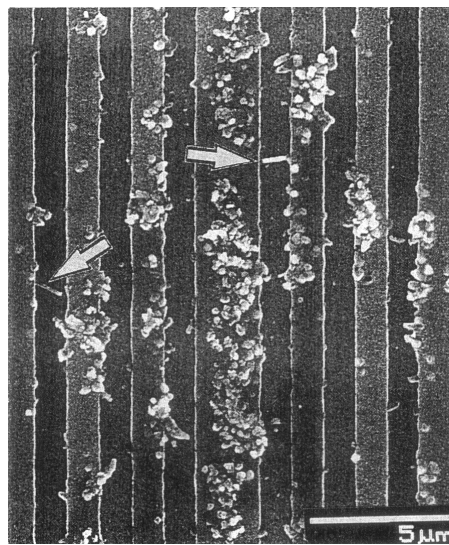
Fig. 2.5:   The arrows in this SEM micrograph aim at extrusion with lengths in the range of the clearance between neighboring electrodes of an SAW device [18].

2.5 Fatigue in thin films

It is well established that decreasing the dimensions in metal films to less then some µm has a significant impact on plastic deformation behavior, which can for example affect the flow stress, as dislocation motion is constrained [27, 28, 29]. In polycrystalline films, the flow stress often increases linearly with the inverse film thickness down to film thickness of 400 nm. It has been found that a further decrease of film thickness does not to lead to an increase of flow stress. This is accompanied by the change of active type of dislocations. In thicker films, threading dislocations which reach from the interface at the substrate to the surface of the film carry the plastic strain, while in thinner films dislocations parallel to the substrate are active [30]. Nevertheless, cyclic mechanical loading of thin films can lead to fatigue which is based on dislocation mechanisms, showing plate like extrusions at the surface similar to bulk samples and void formation at the interface to the substrate in the middle of the grains [31, 32] (Fig. 2.6). This damage formation can lead to crack nucleation in the metallization. Shrinking the film thickness from 1.5 to 0.4 µm leads to an increased lifetime due to an increased flow stress of the film [33]. The plate like extrusions at the surface of the film result from dislocations penetrating the surface of the film, while void formation at the interface can be attributed to the accumulation of vacancies from annihilated dislocation segments. In the case of very small grains with diameters of less than 300 nm, no extrusions can be observed, while the failure of the film results from cracks at the grain boundaries [33, 34].
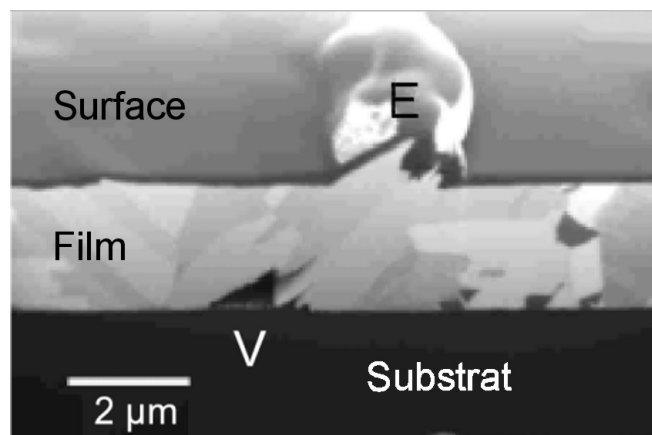
Fig. 2.6:   Cross section prepared by FIB of a 3 µm Cu thin film after cyclic load shows plate like extrusion at the surface (E) and voids at the interface (V) to the Si-substrate. For a better contrast a W layer was deposited on top of the Cu film [32].

2.6 Fatigue at ultra high frequency

Investigation of the frequency dependence of fatigue mechanisms in bulk material is the subject of several studies, as ultra high frequencies can significantly decrease the experimental time in the high-cycle regime [35, 36] ('ultra' comes from ultra sonic and means frequencies higher than 20 kHz). For bulk samples frequencies are limited to some tens of kHz which on one hand results from the technological limitations in cyclic strain control and on the other hand from an adequate sample cooling. But even at these low frequencies compared to SAW test devices which operate in the GHz regime, a frequency increase in strain controlled fatigue experiments can lead to higher fatigue lifetimes in bcc or hexagonal materials [37]. This is attributed to their strong strain rate dependence. In fcc materials like Cu [38] or Al alloys [39, 40] no statistically relevant differences could be observed for comparisons of fatigue at frequencies between 60 Hz and 20 kHz.

2.7 Defect mechanisms active at ultra high frequencies

As mentioned in chapter 2.3 it is not clear so far, which defect mechanisms can be activated by a cyclic mechanical stress in the GHz regime. While the shape of the extrusions is comparable to those found in electromigration which is diffusion based [15], the high frequency and the deviatoric character of the cyclic stresses are indicative to a dislocation mechanism. Both aspects will be considered in the following chapter.

Interaction of dislocations with cyclic stresses in the GHz regime

In order to estimate the shortest time a dislocation needs for crossing a grain with a typical size of 400 nm in a SAW test device, the velocity of sound of a shear wave in Al ($3.1 \cdot 10^3$ m/s [41]) is used as an upper limit for the dislocation velocity:

$$t_{\text{cross}} = \frac{d_{\text{grain}}}{v_{\text{sound}}} \approx \frac{4 \cdot 10^{-7} \, \text{m}}{3.1 \cdot 10^3 \, \dfrac{\text{m}}{\text{s}}} \approx 1.3 \cdot 10^{-10} \, \text{s}, \qquad (2.4)$$

with t_{cross} is the time to cross the grain, d_{grain} is the grain size and v_{sound} is the velocity of sound for a transversal shear wave. Since half of a cycle lasts $5 \cdot 10^{-10}$ s at a typical frequency of 1 GHz a dislocation has enough time during one cycle to cross the grain. From that simple point of view dislocations should be able to move through a grain during a single cycle if the local stress is high enough.

Internal friction measurements can provide a more detailed understanding of the active defect mechanisms at frequencies in the GHz regime. Gremaud stated that at frequencies in the GHz regime only dislocations can interact with cyclic load [42] (Fig. 2.7). It is expected that between pinning points free segments of the dislocations vibrate with the same frequency as the cyclic load. The frequency dependence of the cyclic excitation is described by the 'vibrating string theory' and was first suggested by Koehler and developed further by Granato and Luecke (both in [43]). From this theory it could be expected that the resonance frequency shows an inverse correlation with the dislocation segment length. The resonance frequency of

a 1 μm long dislocation segment can be calculated to be 1 GHz [43], while a 100 nm short dislocation segment would reach a resonance frequency of 10 GHz. Nevertheless, the dislocation amplitude at frequencies higher than 100 to 300 MHz is highly damped due to the strong phonon-dislocation interaction in metals. This behavior can be observed in damping spectra (Fig. 2.7). Measurements for Cu [44, 45] and Au [46] showed that the frequency of this Debye peak in metals ranges from 100 to 300 MHz [42]. This indicates that for a cyclic mechanical load in the GHz regime, the amplitude of a vibrating dislocation segment decreases with increasing frequency. But in general the dislocation segments should be able to follow the cyclically induced force by a cyclic excitation in the GHz regime.
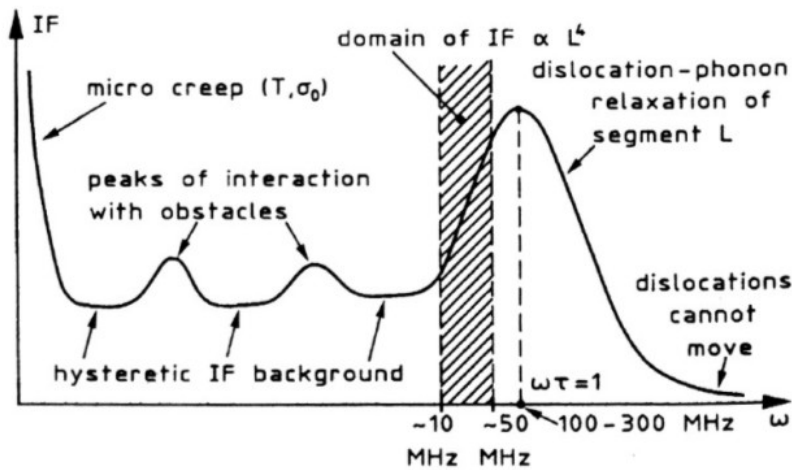
Fig. 2.7:   Schematic internal friction (IF) spectra of metals after Gremaud [42]. At low frequencies creep processes lead to high damping, while at higher frequencies the interaction of dislocations with obstacles leads to maxima in the damping spectra. At frequencies higher than some MHz, the vibrating dislocation segments lead to a peak which is cut off by dislocation-phonon interaction to higher frequencies. In metals the maximum (Debye peak) can be found at frequencies between 100 to 300 MHz. At frequencies higher than some tens of GHz dislocations cannot be stimulated to vibrate.

Are diffusional processes part of the damage formation?

Aside from the similarity of damage structures due to acoustic waves and electromigration, also the activation energies, measured from time to failure experiments, show comparable numbers. The activation energy in pure Al thin films due to electromigration of between 0.47 eV [47] and 0.55 eV [48] (measured from drift velocity experiments) is in the same range as the activation energy due to fatigue by surface waves of

0.46 eV (determined from a time to failure versus inverse temperature plot [49]). Furthermore, alloying of Al electrodes with Cu leads to a significant increase in lifetime. For electromigration experiments, the addition of 4 % Cu leads to an approximately 50 times higher lifetime [50], while in SAW devices the addition of 2 % Cu leads to a 65 times higher life time [9]. As it is well established that the material transport in polycrystalline Al metallizations induced by electromigration is concentrated at the grain boundaries it could be concluded that the same is valid for surface wave induced damage formation. Thus it can be expected, that grain boundary diffusion has an influence on the damage formation in SAW devices.

Thus we calculate how far an atom can diffuse during the time period of one stress cycle. The distance $L_{Diff.}$ an atom can diffuse during one cycle, which corresponds to a diffusion time of $t = 5 \cdot 10^{-10}$ s, can be estimated to be [51]:

$$L_{Diff.} \approx \sqrt{D_{gb} \cdot t} = 2 \cdot 10^{-12} \, m \qquad (2.5)$$

with the grain boundary diffusion coefficient $D_{gb} = 8 \cdot 10^{-17}$ m^2/s resulting from a preexponential factor $D_{gb}{}^{0} = 9.5 \cdot 10^{-13}$ m^2/s, an activation energy for the grain boundary diffusion of $Q_{gb} = 63$ eV [52] and a temperature $T = 303$ K.

As the diffusion length L_{Diff} is nearly two orders of magnitude smaller than an atomic distance, it seems unlikely that diffusion is the dominant damage mechanism in SAW devices.

2.8 Summary of literature review and aims of this study

In summary we can conclude that it is rather unclear which mechanism leads to the fatigue at frequencies in the GHz regime. On the one hand we can assume that the only defect mechanisms which are suspected to be able to interact with cyclic loads at such high frequencies are dislocations. On the other hand the literature shows that the similarity of the damage structure and the comparison of the activation energy indicate that the material transport leading to the characteristic damage structure occurs at the grain boundaries by diffusion. Nevertheless, the limited dimensions in thin films lead to a constrained dislocation motion in the metallization which indicates that, compared to bulk material, the fatigue lifetime of SAW devices could be increased, similar to the observations of Schwaiger et al. [33]. Quantitative measurements of the microstructural changes and the correlation to device performance are currently not available.

Therefore, the aim of this work is to study in detail microstructural changes and damage formation in pure Al metallizations of SAW test devices and their influence on device performance and reliability. Frequencies at one GHz will be used to provide general lifetime predictions of Al thin films in the ultra high-cycle regime ($> 10^{12}$ cycles). The application of quantitative measurements and *in-situ* experiments will be used to enhance the insight into the active defect mechanism and will also enable us to correlate the microstructural damage to device performance. By the use of FEM simulations the correlation between typical damage structures and the device performance will be studied in depth. From the result of this study and in consistence with the findings in literature we want to present a model which explains the damage formation at ultra high frequency fatigue in thin films.

3   *In situ* observations of ultra high cycle fatigue in patterned Al thin films

Abstract - The mechanical requirements of MEMS devices (Micro Electro Mechanical Systems) increase due to shrinking size, rising frequencies and driving power. This chapter focuses on new fatigue mechanisms that arise when small structures (100 nm) are tested at ultrahigh frequencies. The resulting damage sites appeared in regions of cyclic stress concentration as identified by Finite Element Analysis. *In situ* measurements revealed a characteristic extrusion/void formation mechanism operating on a short time scale. Quantitative post-test analysis of the *in situ* tested samples also showed a correlation between extrusion density and electrical devices performance. The observed damage formation is explained by the combined action of dislocation motion and stress-induced diffusion processes.

3.1 Introduction

Micro electro-mechanical systems can be subject to alternating mechanical stresses. They work at frequencies ranging from kHz up to the GHz regime. Cyclic mechanical stresses lead to novel fatigue effects in the metallizations due to the small dimensions and ultra high frequencies. Even at room temperature these mechanical loads can cause the formation of voids and hillocks, leading to device degradation or sudden failure because of short circuits [4, 10, 17].

One example are Surface Acoustic Wave (SAW) frequency filters, which are based on the conversion of electromagnetic waves into acoustic waves by spatially periodic electrodes on a piezoelectric substrate [5]. Latham et al. [4] observed hillock-like extrusions at the surface of the Al metallization that covered the substrate. The damage was located at the maxima of the standing surface wave. Damage formation was attributed to the cyclic mechanical stresses. By the use of a combined scanning electron and atomic force microscope Shibagaki et al. [10] observed that SAW induced hillock-like extrusion formation in Al is accompanied by void formation. In Cu metallizations only void formation was observed by Menzel et al. [16], which was attributed to the fact that Cu unlike Al does not form a continuous oxide layer.

SAW devices have become increasingly important in the wireless industry. Thus a considerable research effort has been undertaken to increase the reliability of high performance devices. A variety of performance enhancing approaches include the use of alloying elements such as Cu, Ti and W [18, 19, 20] and epitaxial [21, 22] or multilayer metallizations [23, 24, 25, 26]. But, until now, no detailed analysis of the damage formation process has been carried out.

In this chapter, we will focus on the development of microstructural damage induced by surface waves in pure Al metallizations. It will be discussed how the damage structure is influenced by the surface wave induced local cyclic stress state as calculated by Finite Element simulations (FEA), the limited dimensions due to the submicron film thickness and the ultra high frequencies.

3.2 Experimental

A Ladder-type (L-type) SAW test device was used to study the damage formation during ultra high frequency loading. Fig. 3.1 shows the schematic of the metallization on the piezoelectric substrate of such a device. The test sample consisted of two Inter Digital Transducers (IDT) (B), where the upper one was set up in a serial configuration, whereas the lower one was in a parallel configuration. The AC electromagnetic signal was fed into the IDT (B) by contact pads on the left hand side (A). The electric field lines in direction of the y-axis between the fingers of the two comb structures of the IDT induce a shear deformation in the xy-plane of the piezo-crystalline substrate. Thus, the two comb structures move in anti parallel manner to each other in the direction of the y-axis. In the case of an alternating voltage this leads to an oscillating motion of the comb structures into and out of each other. The excitation amplitude of the comb structures relative to each other depends strongly on the exciter frequency. Using the resonance frequency of the metallization/substrate system for the AC signal frequency results in a standing SAW. A standing SAW can reach high amplitudes, inducing high cyclic stresses in the metallization. Other frequencies than the resonance frequency would produce traveling SAWs with much lower amplitudes. As the resonance frequency is different for the two IDTs, a standing SAW only develops in one of them, depending on the frequency of the function generator signal.

We used pure Al thin films with a thickness of 420 nm as a metallization layer. The piezoelectric substrate was single crystalline 42° rotated Y-cut $LiTaO_3$. The Al structures were created by the use of a lift-off process. The pitch size (the distance between the centers of neighboring fingers of the two comb structures) was roughly 2 μm, which led to a resonance frequency of about 900 MHz. After the lift-off process an isothermal annealing for several hours was performed in air at approximately 540 K. For better handling, the samples were mounted onto a circuit board with a size of 20·20 mm² and an electrical connection was established by unshielded bond wires.

The texture of the Al metallizations on $LiTaO_3$ was determined by X-ray diffraction (XRD), namely *θ-2θ* scans and pole figures using Cu-K$_\alpha$ radiation. The measurements were performed on fully metallized $LiTaO_3$ wafers which showed the same microstructure but a much higher metallization volume than the structured films.
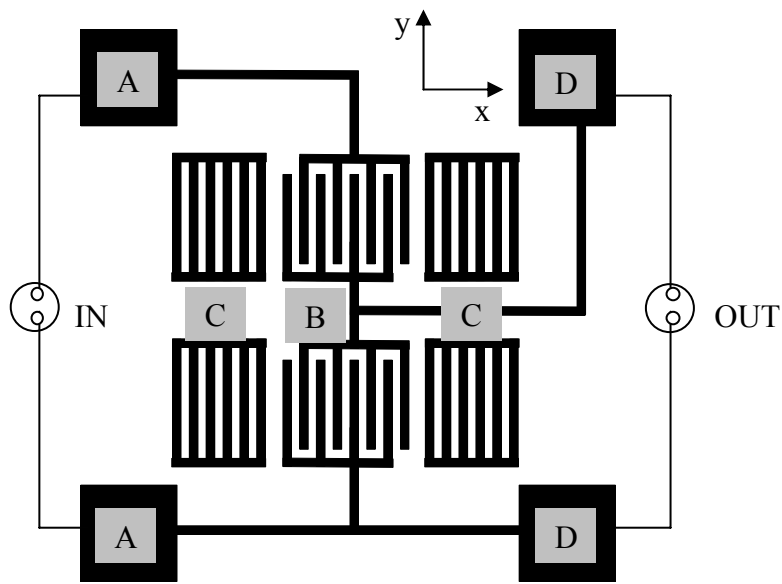
Fig. 3.1: Schematic of a L-type SAW resonator metallization. The devices are composed of the following logical components: A, D: contact pad, B: metal comb structure (Inter-digital transducer IDT), C: reflectors. The pitch size of the fingers of the comb structure (B) is equal to the pitch size of the resonator (C). The upper IDT is in a serial configuration, while the lower IDT is in a parallel. The pitch sizes of the two IDT's are slightly different as well as their resonance frequency.

The transfer function S_{12} (Fig. 3.2) is commonly used to measure the frequency filter properties of SAW devices. The transfer function describes the particular output level (measured at D) which corresponds to a given input (A) for a range of frequencies (in this case from 800 to 870 MHz). Temperature changes lead to a reversible frequency shift of the transfer function, while a frequency shift due to decreasing device performance is irreversible [49]. The frequency shift of the left edge of the transfer function was measured at two different amplitudes relative to the maximum amplitude (-3 or -6 dB), to account for shape changes in the transfer function. The main error in measuring the frequency shift was caused by the shape change of the transfer function. This error was estimated to be +/- 0.1 MHz. The plot in Fig. 3.2 shows the transfer function of the sample at 341 K before (dashed line) and after (continuous line) the *in situ* experiment. Both edges of the transfer function (arrows) were shifted to lower frequencies.
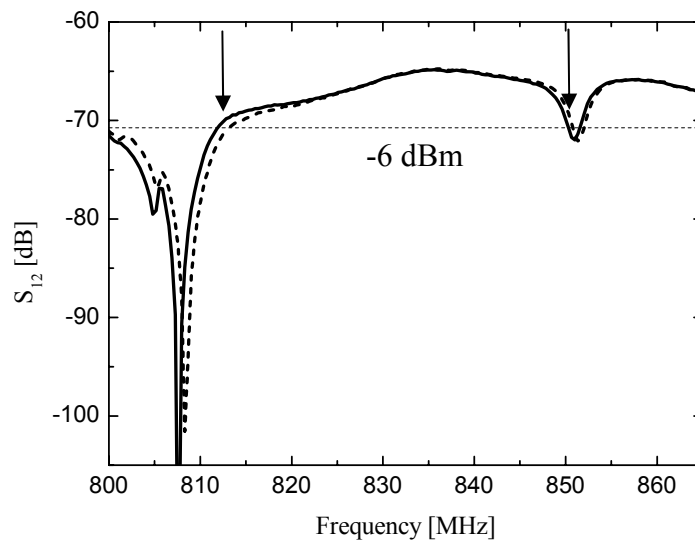
Fig. 3.2: The dashed line shows the transfer-function (S_{12}) before the *in situ* experiment, while the continuous one shows the transfer-function after the *in situ* experiment. The shift of the edges of the transfer-function (arrows) is a result of the microstructural changes in the IDT fingers. The shift of the transfer function was measured at -3 and -6 dB relative to the maximum. The horizontal dashed line is plotted at the level of -6 dBm relative to the maximum.

The *in situ* measurement system in the SEM (Leo 1530 VP, LEO) (Fig. 3.3) consisted of a function generator, an amplifier, a bidirectional coupler, a power meter, a network analyzer and a heating stage, onto which the sample was mounted. The function generator produced the AC-signal at the desired frequency. This signal could be amplified and fed into the test sample. During the load sequence, the transfer function S_{12} of the test sample could be monitored by the network analyzer. The heating stage inside the SEM enabled measurements at elevated temperatures.
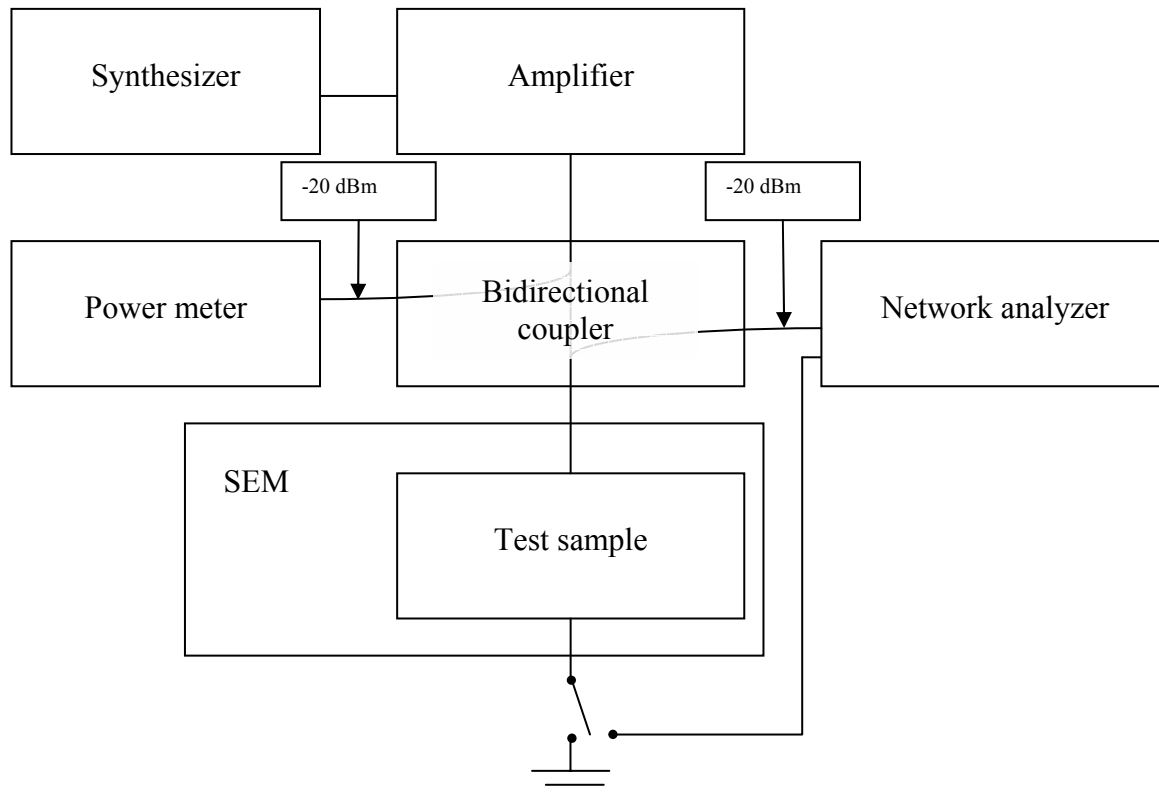
Fig. 3.3: The schematic shows the electronic setup of the *in situ* measurement system. The signal from the synthesizer gets amplified and is than induced into the test sample. By the use of a bidirectional coupler, the electrical power of the amplified signal can be controlled with the power meter during the test. The transfer function can be also measured during the test by the network analyzer. The power meter and the network analyzer are both protected by an attenuation of the signal. The sample is placed in the vacuum chamber of the SEM during the experiment. After each load sequence the sample was imaged with the SEM and the transfer function of the sample was again measured by the Network Analyzer.

A detailed description of the instrumental measurement setup for the *ex situ* experiment provided for comparison in Fig. 3.8 can be found in Raml *et al.* [9]. The sample was loaded with a resonance frequency of the testing device transfer function. Frequency shifts of the resonance frequency due to temperature changes as well as damage formation were adjusted by the change of the load frequency. Thus, the stress maxima of the standing surface waves stayed at the same spot of the metallization.

The AC-load was interrupted for imaging, because the SEM image was distorted by the high frequency signal during load. Between the load sequences the transfer function S_{12} was measured. For imaging and measurement of the transfer function about 90 s were needed. The load time was increased during the experiment, ranging from a few seconds up to 1000 seconds. The cumulative load time for each sample was in the range of 2000 to 3000 seconds. The error of time measurement for each load sequence was in the range of +/- 2 s. The target value for the electrical power for the load was 22 +/- 0.2 dBm (equivalent to 158 mW) at a frequency of 815 MHz. Experiments were carried out at three temperatures (297, 321, 341 K).

The post-test microstructure was analyzed by a focused ion beam (FIB) microscope (FEI FIB 200xP). Different tilt angles between the crystallographic orientation of a grain and the ion beam generate different amounts of secondary electrons. This leads to a contrast between grains of different crystallographic orientations. To get a good channeling contrast the native oxide layer of the Al metallization was sputtered away by the ion beam in the FIB. The FIB micrographs were all imaged with a tilt angle of 35° to the sample normal.

3.3 Results

XRD measurements combined with FIB characterizations of the Al microstructure of fully metallized wafers revealed a (111) fiber texture. The grain size differed slightly between the fully metallized and the structured Al layer. From a qualitative FIB characterization, the grain size was roughly equal to the film thickness. The extrusions in Fig. 3.4 were classified into three different extrusion categories:

- *high aspect ratio extrusions* (HA) nucleate at grain boundaries and reach significant lengths while their height (z-axis) is equivalent to their width (y-axis)

- *grain-like extrusions* (GL) reach widths comparable to the average grain size, but smaller lengths and heights of the film thickness

- *half-height extrusions* (HH) reach widths of the average grain size, heights of the half film thickness and lengths in the range of their width.
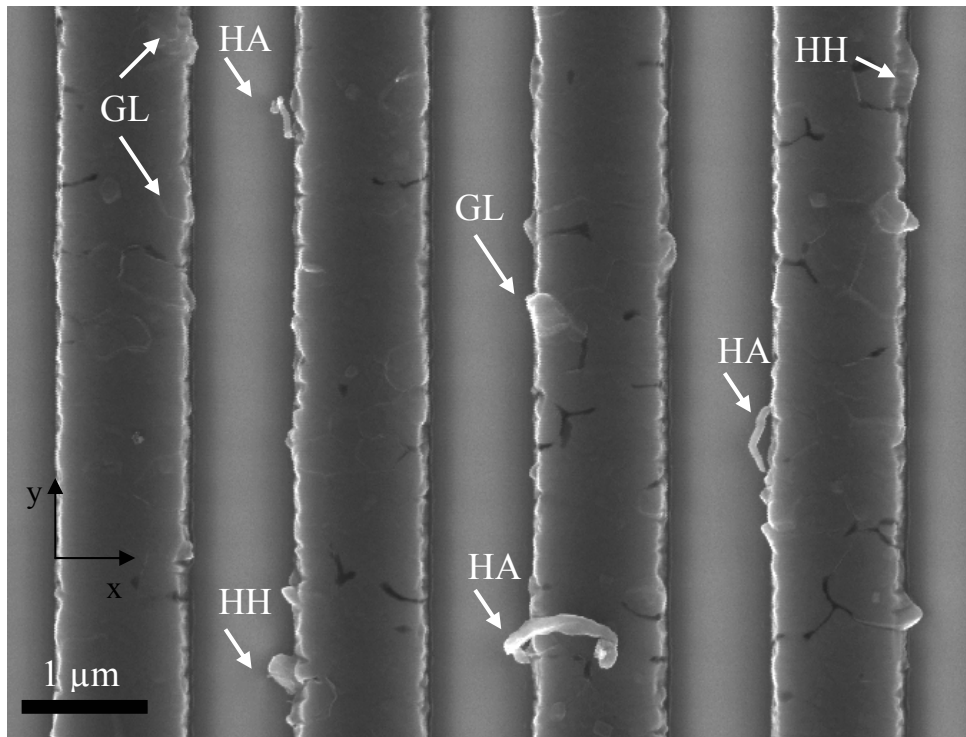
Fig. 3.4:   SEM micrographs show details of the damage formation by surface waves. An AC power of 22 dBm (equal to 158 mW) at 815 MHz was applied at a temperature of 341 K for 3084s (equal to $2.5 \cdot 10^{12}$ cycles). HH stands for *half-height extrusion*, HA stands for *high-aspect ratio extrusion* and GL stands for *grain-like extrusion*.

The dark areas on the fingers are voids reaching the surface of the metallization. Voids and extrusions were always observed to be located close to each other. The two SEM micrograph sequences in Fig. 3.5 and 3.6 give a qualitative picture of the surface wave induced damage formation in thin films versus time. The areas were chosen because they showed a typical damage evolution.

Before the nucleation of the extrusion G in the micrograph sequence of Fig. 3.5, slit-like voids (A to E) with a visible length ranging from 20 to 50 nm and a small extrusion (F) appeared at the edge of the finger. From 492 s on, each load step led to a further increase in the length of the extrusion G, except the last one. The extrusion G needed about 1000 s for its growth process. After 3084 s the material had been loaded for nearly $3 \cdot 10^{12}$ cycles and the finger had changed its shape considerably. Slit-like voids and light lines on the surface between the points A, C and G, which nucleated at the edges of the finger, advanced into the middle of the finger. The FIB micrograph showed that all white and black lines were located at grain boundaries and extrusions could be observed between the grains. Protruding lips at point D and C belonged to whole grains. Between C and A a cavity could be observed.

In Fig. 3.6 after 132 s a 400 nm wide segment of the edge of the finger was pushed out of the finger. A light line between II and III got clearly visible after 252 seconds. Also the edge segment of the finger at arrow III had moved significantly, while a slit-like grain-boundary void had opened. After 300 s the edge segment at arrow III stopped moving. The so far described damage stayed stable during the rest of the 2592 s, while four other extrusions appeared. At the end of the experiment, after 3084 s, the shape of the edge of the finger got strongly facetted. The FIB micrograph showed that the three slit-like voids as well as the light lines on the surface corresponded very well to the grain structure. The protruded edge segment of the finger (arrow III) belonged to a single grain.
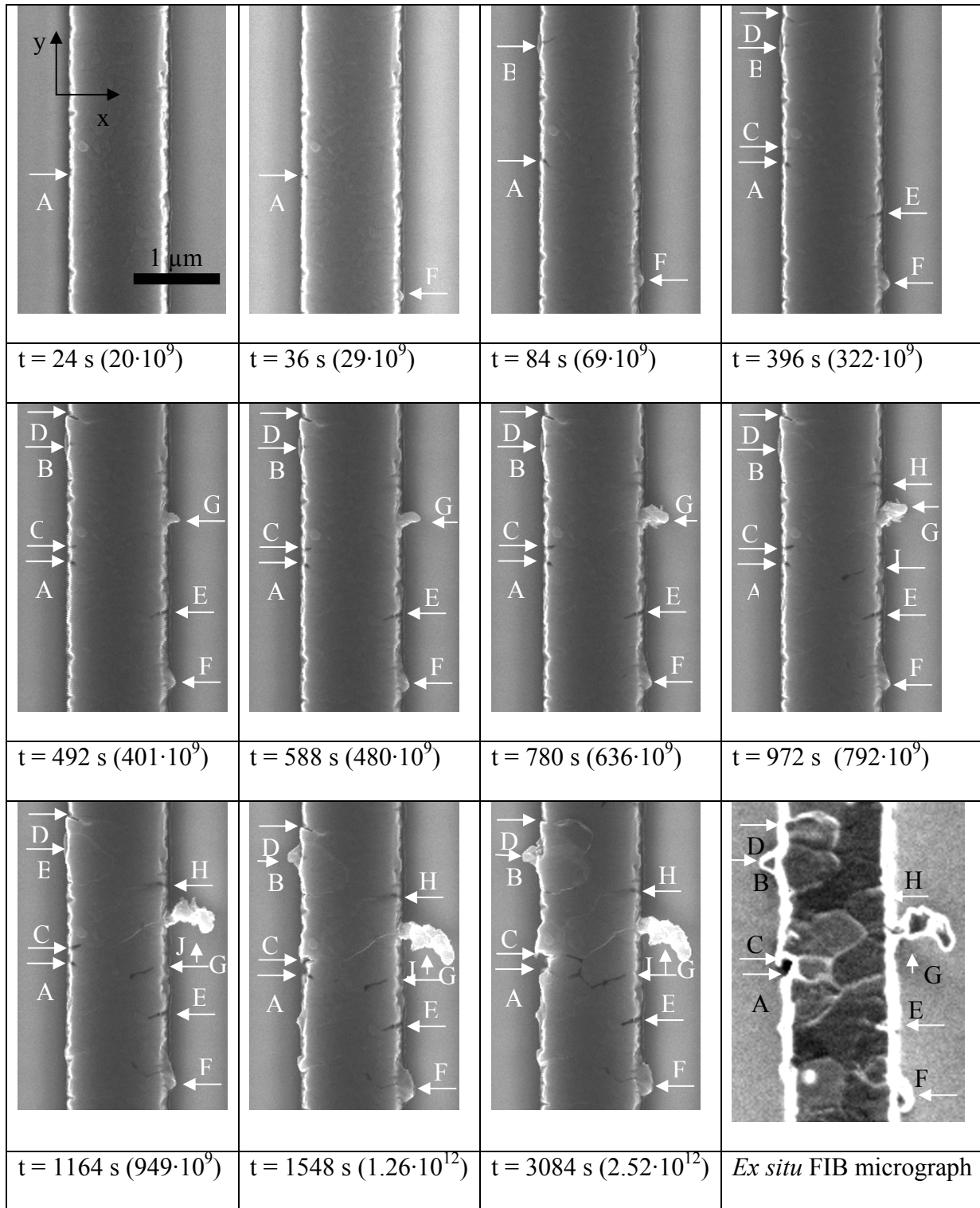
Figure 3.5: Series of SEM micrographs showing details of the microstructural changes during the interrupted *in situ* experiment at the same location. The FIB micrographs were imaged at a tilt angle of 35°. The channelling contrast in the *ex situ* FIB micrograph shows the grain structure after the experiment. The average line width was 1.1 μm. Under each micrograph the experimental time (number of cycles) is given. An AC power of 22 dBm (equal to 158 mW) at 815 MHz was used at a temperature of 341 K. Not all micrographs of the experiment are presented here.
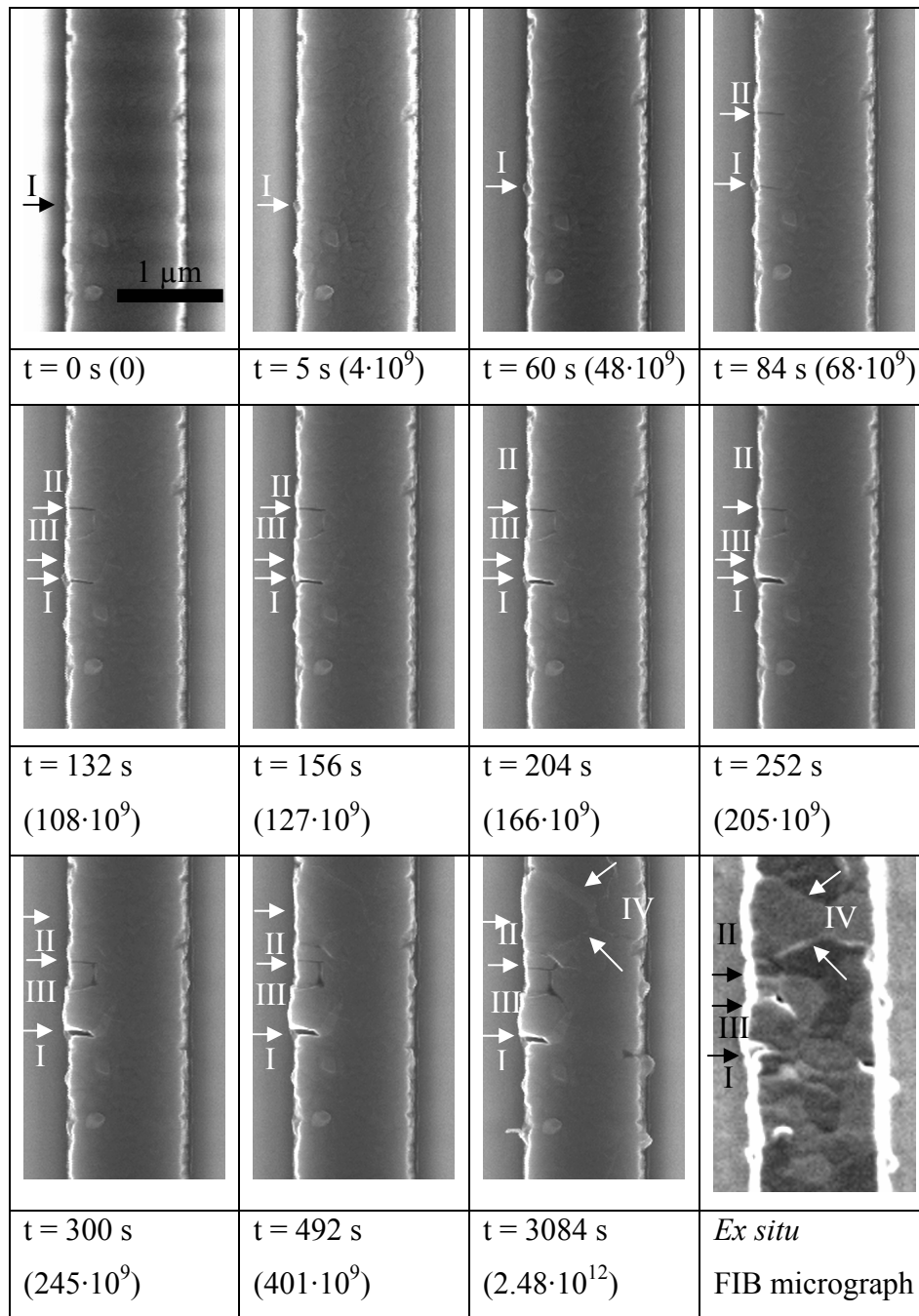
Fig. 3.6:   This series of SEM micrographs shows the surface wave induced damage formation at a finger from the same experiment as in Fig. 3.5 but at a different location.

The plot in Fig. 3.7 shows the frequency shift versus time. The upper horizontal line at 1 MHz represents a commonly used failure criterion [9]. The lower line represents the limitation by the measurement error of +/- 0.1 MHz. In a double logarithmic plot the absolute value of the frequency shift increases linearly with time. The interrupted *in situ* measurements at different temperatures (301, 321 and 341 K) followed the same trend for a frequency shift higher than 0.1 MHz. The measurement at 321 and 341 K showed only a small difference in the absolute values. The slope of the apparent linear fit is in the range of 0.5 corresponding to a square root dependency.
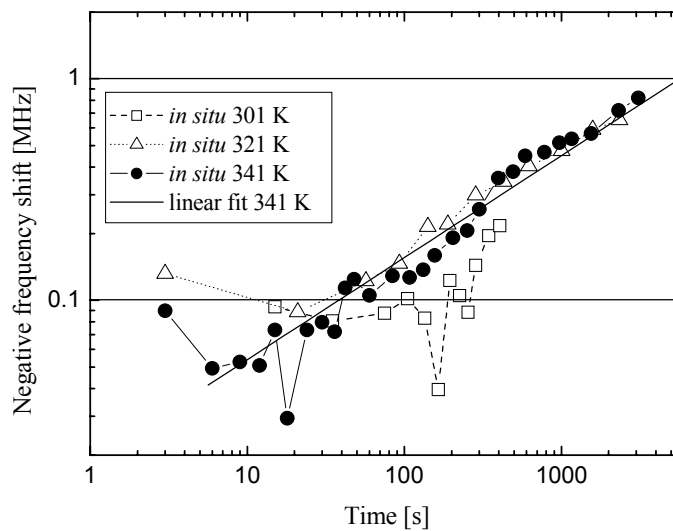
Fig. 3.7:   The negative frequency shift of the left edge of the transfer function S_{12} versus time includes the results of all *in situ* experiments (Tab. 8.1- 8.3). The horizontal line at 0.1 MHz marks the error of the measurement. The apparent linear fit of the *in situ* measurement at 341 K showed a slope of 0.5 in the log-log plot.

While the frequency shift is an integral measurement which contains all types of damage formation affecting the transfer function S_{12}, the surface wave induced material migration in the Al metallization itself can directly be measured by the number of extrusions per electrode length. This is defined as the extrusion density and was measured from top view images made during the *in situ* tests with the SEM. To be able to measure the change of extrusion density for each load sequence, the last SEM micrograph of the stressed sample was analyzed (e.g. for the sample at 341 K the micrograph after 3084 s of load was used). For that, each extrusion was framed by a small box which fit to the width and length of the extrusion by the use of a vector graphics program. After that, the previous micrograph was loaded and the size of each

box was changed until they fitted again to the size of the extrusions. This procedure was applied to all SEM micrographs. Extrusions present before the first load sequence were discarded. The linear correlation of the frequency shift and the extrusion density is shown in Fig. 3.8. The extrusion density and the frequency shift of the *ex situ* measurements (chapter 4), which are shown for comparison (symbol: open stars), and of the *in situ* experiments are in the same range.
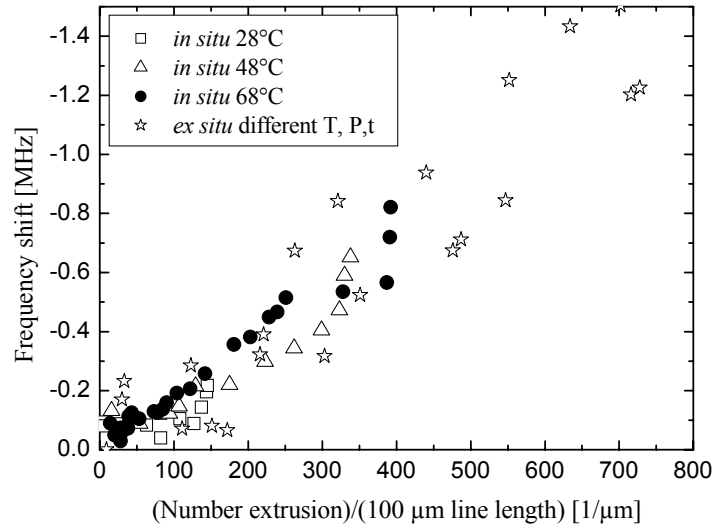
Fig. 3.8:   Frequency shift versus the extrusion density of the *in situ* experiments (Tab. 8.1- 8.3) compared to *ex situ* measurements. The *ex situ* experiments were carried out at different temperatures (303, 333, and 358 K) and powers (12, 30 and 50 mW) for times (2, 8, 16 h, which is equal to $6 \cdot 10^{12}$, $23 \cdot 10^{12}$, $47 \cdot 10^{12}$) (for details see chapter 4).

3.4 Finite Element Analysis

The calculation of the relative stresses in the fingers was done by the use of an FEA program (Multiphysics module of ANSYS 7.0). Fig. 3.9 shows the model. For the finger a Young's modulus of 70 GPa and a density of 2.7 g/cm³, while for the substrate a Young's modulus of 233 GPa [53] and a density of 7.46 g/cm³ [54] was used, neglecting the elastic anisotropy. The width of the finger was 1 μm, its height was set to 420 nm and its length to 2 μm. The dimensions of the substrate were 2 μm in width, 2 μm in height and 2 μm in length. The outer planes of the substrate in positive and negative x-direction as well as in negative z-direction were fixed in their position. In x-direction, the outer areas of the finger and the substrate were set to antisymmetric boundary conditions. Cubic elements with 8 nodes (brick 45) were used for the simulation of the elastic properties of the finger and the substrate. The edge length of the elements was set to 100 nm. So the finger consisted of $50 \times 12 \times 5$ elements. The interface between the substrate and the finger was defined as 'always bonded' with the elastic properties of the finger. The eigenfrequency analysis was solved with the Lancosz algorithm of the 'nodal analysis', included in the FEA program. The analysis was performed between frequencies of 850 MHz and 950 MHz. The 'postprocessor' of the FEA program was applied to display the stress deviation in the finger.

Fig. 3.9 shows the cyclic deformation by the surface wave at the maximum deflection of the oscillation. The inertia led to a force on each part of the finger in the x-direction. The maximum cyclic shear stress τ_{yz} could be found at the interface between the finger and the substrate. As the two comb structures always move in opposite direction to each other, the plane between two adjacent fingers does not move because of symmetry conditions. Between two of these planes the substrate is cyclically deflected in y-direction as can be seen in Fig. 3.9. Because the substrate is much stiffer than the metallization, the bending is impressed onto the finger at the interface between finger and substrate. The resulting stress state, combined with the shear stress induced by inertia, yields the whole surface wave induced stress state in the finger. The surface wave induced cyclic stress tensor only contained deviatoric components. The highest cyclic shear stress values are the τ_{yz} components. The von Mises stress was used to show the local stress concentration in the finger (Fig. 3.10). The

maximum cyclic stress developed at the edges of the finger, while the minimum cyclic stress was found at the top surface in the center of the finger.
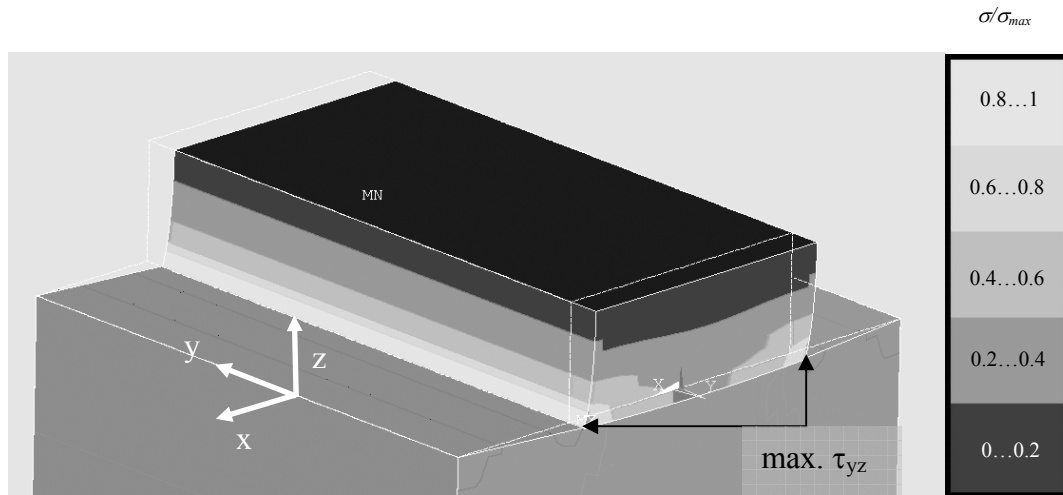
Fig. 3.9:   The eigenfrequency analysis with an FEM program shows the cyclic deformation and the resulting stress. The white lines show the different shapes between the unstressed state and at the maximum deflection. The lower figure shows the resulting stress state in the finger. Maximum cyclic shear stress by the standing surface acoustic wave could be found at the lower left and right edge. Hydrostatic stresses were not observed.
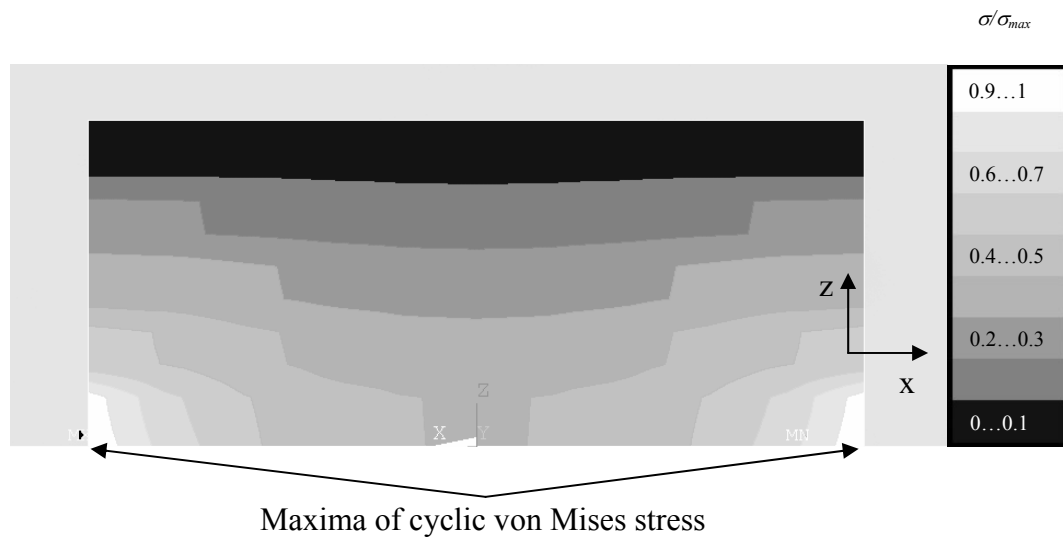
Fig. 3.10:   Maximum cyclic shear stress by the standing surface acoustic wave could be found at the lower left and right edge. Hydrostatic stresses were not observed.

3.5 Discussion

The first part of the discussion will address the morphology of the surface wave induced damage structure and the underlying defect mechanisms like dislocations or diffusion. The second part of the discussion will focus on the quantitative results and their interpretation.

Latham et al. [4] compared the hillock-like extrusion formation to electromigration [55] instead of fatigue effects. The underlying mechanism was called a material migration process, although the damage formation was caused by cyclic mechanical stresses. For this reason other authors called the damage formation by acoustic waves 'acoustomigration'. Obviously this is related to the shape of the damage, which is completely contrary to what is known from fatigue effects in ductile bulk samples. In bulk samples, surface artifacts due to fatigue normally exhibit plate-like extrusions penetrating the surface of grains, indicating dislocation mechanisms. Regardless of the developing damage structure, however, the damage formation induced by acoustic waves in thin films is a form of fatigue, as device degradation is solely due to cyclic mechanical stresses.

The damage morphology in SAW devices was quantified by the measurement of the extrusion density. Voids at the interface between finger and substrate could not be detected by SEM micrographs, as they only became visible when reaching the top surface of the finger. As Fig. 3.8 shows, the frequency shift and the extrusion density are directly correlated. To understand this correlation we first have to address the influence of the elastic properties of the metallization on the transfer function S_{12} (Fig. 3.2). The form and the location of the transfer function S_{12} corresponds among other things to the resonance frequency of the two comb structures (Fig. 3.1) [23]. A shift of the resonance frequency of the comb structures causes a shift of the transfer function (Fig. 3.2). The stability of the resonance frequency of the comb structure is critically influenced by the properties of the metallization. It depends on the amount of oscillating masses and the Young's moduli of the metallization and substrate. The formation of surface wave induced damage shifts material from voids to extrusions and thus changes the effective elastic properties of the metallization. Slit-like voids (Fig. 3.5 and 3.6) lead to a decrease of the average stress in the finger. The stiffness of the fingers decreases linearly with increasing defect density. This is equivalent to a decrease in Young's modulus of the metallization, leading to a lower resonance frequency of the entire comb structure.

Thus, the defect density at the finger and the frequency shift of the transfer function are correlated. All *in situ* measurements showed the same dependency as the *ex situ* measurements that are plotted here for comparison. The *ex situ* measurements were performed in air, while the *in situ* experiments were performed in high vacuum. This seems to have no significant influence on the defect mechanism induced by surface waves.

The discussion of the surface waves induced damage structure (Fig. 3.5 and 3.6) and their underlying mechanisms has to consider the *differences in stress state*, the *small dimensions* and the applied *ultra high frequencies (GHz),* leading to different damage structures compared to the structures known from fatigue in bulk materials:

The eigenfrequency analysis by FEA of the surface acoustic wave induced stress showed three important differences in the cyclic stress state compared to tensile testing fatigue experiments. While tensile testing in principle induces a homogeneous uniaxial stress state over the whole sample, the surface wave induced stress state consists only of deviatoric components, which vary as a function of space resulting in stress gradients. The highest cyclic stress values were found at the interface between the substrate and the metallization at the outer edges of the finger (Fig. 3.10). As can be seen in the two image sequences (Figs 3.5 and 3.6), the nucleation of the defects primarily takes place at the side of the fingers. Slit-like void formation always starts at the side and advances into the finger. The direction of the progress of void formation is then determined only by the geometry of the grain boundary. As the grain boundaries in these Ladder-type structures are mainly oriented perpendicular to the edge of the fingers, the void formation normally follows this direction.

The main cyclic stress induced by acoustic waves in Ladder-type structures as used for these experiments is the τ_{yz} component. This shear component preferentially activates dislocation movement parallel to the substrate. As XRD measurements revealed a (111) fiber texture for the Al metallization, the glide planes are also oriented parallel to the substrate, which can lead to a shearing in x-direction, depending on the in-plane orientation of the grains. The resulting relative displacement of grains could induce normal stresses at the grain boundary. A plate-like extrusion formation out of the top surface of the grains like in bulk samples [56] is not expected due to the difference of the cyclic stress state. Our results could confirm this prediction.

Assuming that void formation is indicative of tensile stresses and extrusion formation reflects compressive stresses, we expect to find evidence for the presence of neighboring regions that had been subject to compressive and tensile stresses. Fig. 3.11 represents this

correlation between the extrusion and void formation. The white arrows indicates the grain shift that induced tensile stresses at the location of the observed voids (A, C, H, J) and compressive stresses at the location, where the extrusion (G) grew.
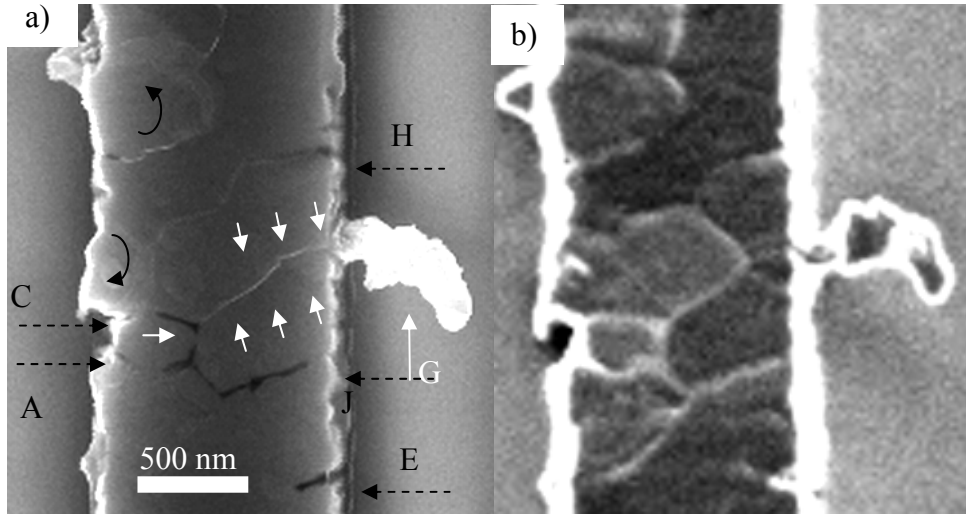
Fig. 3.11:   a) SEM micrograph shows the same location as Fig. 5 after 3084 s of load. The white arrows indicate grain shifts. The black arrows indicate grain rotations. b) FIB micrograph of the same site showing the grain as comparison.

In addition to the surface wave induced cyclic shear stresses the thermal treatment also induces stresses. As the thermal expansion coefficients of the metallization and the substrate are different, a temperature change will induce thermal stresses [27]. The 42° Y-cut LiTaO$_3$ has a coefficient of thermal expansion between 0.9 to $1.6 \cdot 10^{-6}$ 1/K [54], depending on the crystal orientation, while Al has a coefficient of thermal expansion of $23.5 \cdot 10^{-6}$ 1/K. Cooling down the test sample from an annealing temperature of 540 K to RT leads to a tensile stress. The tensile stress can enhance the nucleation of voids, which would lead to a preferred void formation at lower temperatures where thermal stresses are higher. So far this could not be confirmed by our observations.

As small dimensions have a significant influence on plasticity [27] we should also discuss their influence on fatigue. The difference of fatigue induced damage formation in thin films (with thicknesses smaller than 1 μm) and bulk material is that in thin films no characteristic dislocation structures can form. This is due to the limited dimension of thin films, which are smaller than the typical dimensions of dislocation structures observed in bulk material. Even though, plate-like extrusions develop at the surface of the grains of Cu [31] and Ag [33] thin

films, they correspond to crystallographic glide planes and scale with the film thickness. We can assume that small dimensions could restrict dislocation motion but will not inhibit fatigue completely.

Up to now, no other fatigue experiment is capable of reaching frequencies in the GHz regime. Fatigue experiments with bulk samples are limited to a maximum frequency of 20 kHz [36] because of the increasing heat dissipation. Only internal friction experiments using very low amplitudes can give some information about the active defect mechanisms at these high frequencies. For pure Cu [44, 45] and pure Au [46] the mechanical damping by dislocations decreased for frequencies higher than 100 MHz. This means that the oscillation amplitude of the dislocations decreases with increasing frequency, which may lead to a deceleration of dislocation based damage formation at ultra high frequencies.

3.6 Summary

In situ fatigue tests on 420 nm thin Al films at ultra high frequencies (900 MHz) by Surface Acoustic Wave (SAW) devices were performed. From the discussion we can summarize:

- The damage formed by 'acoustomigration' corresponds to the definition of fatigue since the damage formed in the metallization is induced by a cyclic mechanical stress.

- The performance (i.e. the frequency shift) of the SAW filter and the defect density of its metallization show a direct correlation. This is due to the change of the stiffness of the metallization by slit-like void formation.

- Extrusions and voids usually occur at the lower part of the electrode's sidewall, which is the location of highest cyclic shear stress as determined by Finite Element Analysis.

- The cyclic shear stress led to the observed slit-like void and extrusion formation at grain boundaries which were assumed to correspond to sites of high tensile and compressive stresses.

4 Damage analysis in Al thin films fatigued at ultra high frequencies

Abstract: Thin film metallizations fatigue data suffers from ultra high cycle results. To study fatigue at ultra high cycles, Surface Acoustic Wave (SAW) test devices were used to test continuous and patterned Al thin films at ultra high frequencies. For stress amplitudes as low as 14 MPa lifetime measurements showed no fatigue limit for 400 nm Al thin films. The analysis of microstructural changes revealed extrusion and void formation concentrated at grain boundaries. This finding and the observed grain growth indicated a high material flux at the grain boundaries induced by the cyclic load. The direct correlation between device performance and defect density showed a functional agreement with a common theory on the influence of crack density on intrinsic stresses in thin metal films. The estimation of the short circuit probability from the extrusion length distribution revealed an exponential dependency on the electrode distance. This is the first analysis which provides quantitative insight concerning active damage mechanisms and fatigue life time at ultra high frequencies.

4.1 Introduction

Fatigue measurements at ultra high frequencies (20 kHz) have been used to study lifetime limits of metal bulk samples [36] to obtain a more profound knowledge on fatigue mechanisms in the regime of 10^{10} cycles to failure. The limiting factor in these experiments is the achievable cyclic load frequency. For bulk samples the highest frequency which can be reached is in the range of 10^4 to 10^5 Hz due to difficulties of inducing the cyclic load amplitude and the heat dissipation from the samples. These problems can be solved by reducing the sample size for example by the utilization of Micro Electro Mechanical Systems (MEMS) as shown for Si-based devices [57, 58]. Due to the miniaturization of resonant devices, loading frequencies can be increased from some kHz to several MHz and the resulting higher surface to volume ratio resolves issues related to heat dissipation. Working at such high frequencies, cycle numbers of 10^9 to 10^{12} can be reached within several hours, which was realized by several authors measuring fatigue properties of pure Si [59].

In this chapter, we will focus on characteristic fatigue effects (Fig. 4.1) in structured and continuous metal thin films at ultra high frequencies in SAW test devices which are used for frequency filtering. In these resonators electric energy is transduced by an Interdigital Transducer (IDT) into acoustic energy in form of acoustic waves at the surface of a piezoelectric crystal [5]. By the use of SAW resonators working at 900 MHz we explore fatigue in the regime between 10^{10} to 10^{15} cycles with experiments lasting from 10 seconds to 12 days.

- The induced cyclic mechanical load results in a characteristic damage formation in the metallization on a short time scale at room temperature (RT) (Fig. 4.1). Qualitatively, three different failure types have been observed so far:

- Latham et al. [4] observed a matrix of dendrite-like extrusions in pure Al films accompanied by an *irreversible change of the resonance frequency* of the device.

- Hosaka et al. [17] found that hillock-like extrusions, growing out of the side of neighboring electrodes, can result in *short circuits*, which lead to an immediate malfunction of the SAW device.

Beside the formation of extrusions Shibagaki et al. [10] also observed voids by combining a scanning electron microscopy (SEM) with a scanning tunnel microscope (STM). Resistivity measurements at degraded stripe pattern revealed a correlation between surface wave induced void formation and resistance increase. They concluded that the observed *increase of the insertion loss* (which is the fraction between the input and output amplitude) of the SAW device was caused by the increasing resistance of the electrodes.

Up to now, these failure types observed in SAW devices were only qualitatively correlated with the microstructural damage formation.
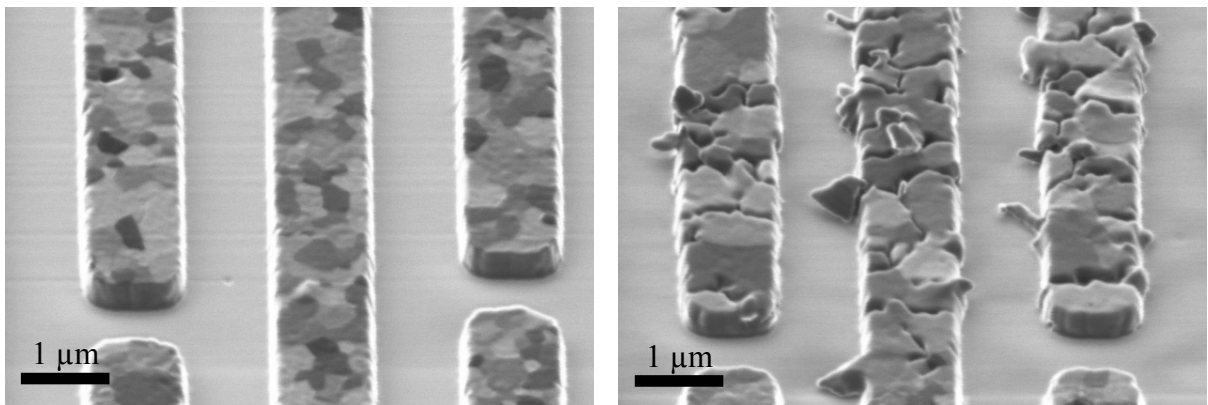
Fig. 4.1:   FIB image of two comb structures of an L-type SAW-resonator showing the microstructural changes by surface waves as was shown in chapter 3. Both interdigital transducers (IDT) belong to the same test device but only the structure on the right hand side was loaded at its resonance frequency. Details will be explained in section 4.2.

Therefore, in this chapter, we will aim for a detailed analysis of the microstructural changes and damage formation in continuous and structured Al metallizations due to cyclic load at ultra high frequencies (900 MHz). The qualitative and quantitative analysis of the microstructural changes due to fatigue gives a more detailed insight into the active fatigue mechanisms and the possibility to estimate the lifetime of Al metallizations.

4.2 Experimental

Sample preparation

For this study, we have chosen pure Al as electrode material, to exclude complicating effects of alloying elements. The piezoelectric substrate was single crystalline 42° rotated Y-cut $LiTaO_3$, which is typically used in commercial SAW devices. The pure Al thin films were vapor deposited onto the $LiTaO_3$ substrate. The Al films were patterned by a lift-off process. Subsequently the samples were annealed for eight hours at approximately 540 K in air.

Working principle and test designs

The working principle of the used SAW test devices is based on the transduction of an electromagnetic AC signal into a surface acoustic wave on the piezoelectric substrate by a metal thin film Inter Digital Transducer (IDT) (e.g.: B and D in Fig. 4.2 a). The IDTs consist of two comb structures of metal thin film finger electrodes on a piezoelectric substrate. Applying an electric voltage between the two comb structures induced an electric field between the electrodes of the IDT. Therefore the substrate surface underneath the metallization deforms roughly sinusoidal. An AC signal, induced into the IDT, leads to a cyclic displacement of the substrate surface. The propagation of this surface acoustic wave is restricted by the reflectors at each side of the IDT (E and L in Fig. 4.2 a and b). If the frequency of the AC signal is the same as the resonance frequency of the device, a standing wave develops at the surface. The nodes of the standing wave are localized between the electrodes. The highest cyclic displacement is cited at the centre of the electrodes which leads to a cyclic movement of the electrodes in y-direction. On the one hand inertia forces induce a cyclic shear stress into the electrodes since the electrodes are free to vibrate, stimulated by the cyclically deflected substrate. On the other hand the cyclic sinusoidal deformation of the substrate imposes shear deformation into the metallization. Details for the stress state in patterned and continuous films induced by surface waves were calculated by Kubat [6, 7, 8] and will be discussed in detail in chapter 5. The AC-induced cyclic strain leads to the formation of damage in the metallization.

a)   b)
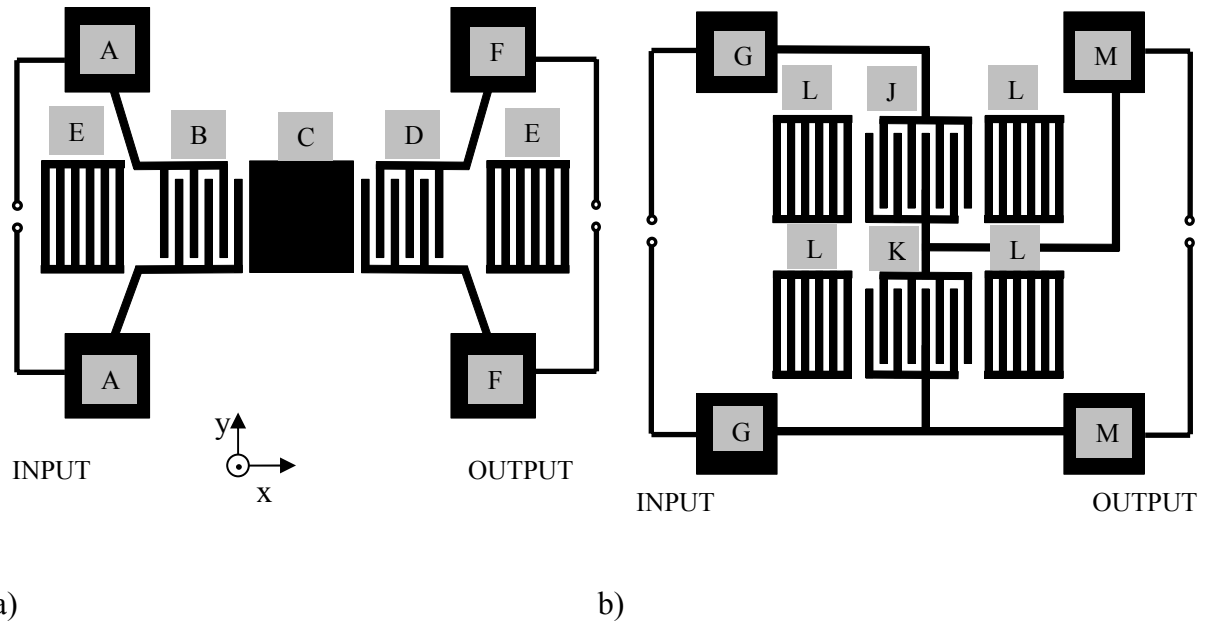
Fig. 4.2:   a) Schematic of a 2-port SAW resonator. The devices consist of the following components: A: contact pads for input, B: input Inter-digital transducer (IDT), C: continuous Al film (Cavity), D: output IDT , E: reflectors F: contact pads for output. b) Schematic of a L-type SAW resonator. The devices consist of the following logical components: G: contact pads for input, J: serial IDT, K: parallel IDT, L: reflectors, M: contact pads for output.

Two different test designs were used to study the surface wave induced damage formation. A 2-port design (Fig. 4.2 a) with a continuous film (C: cavity) in the middle was used to study damage formation in continuous Al metallizations and an Ladder-type (L-type) design (Fig. 4.2 b) was used to study the damage formation in structured Al metallizations.

The 2-port design (Fig 4.2 a) for the SAW test device was designed by Ruile *et al.* [49] in order to test different metallizations independent of the design of a device. The maximum cyclic stress was induced into the continuous film region of the metallization. The pitch size of the IDT electrodes (distance between the center of the electrodes in x-direction) was about 2.2 µm, the electrode width roughly 1 µm, electrode length approximately 90 µm and the metallization thickness was 420 nm, which led to a resonance frequency of about 900 MHz.

The L-type design is shown in Fig. 4.2 b. In this device each of the two IDTs (J, K) was situated in between two reflectors (L). Just like in the case of the 2-port resonator, stimulating the IDT (serial IDT: J or parallel IDT: K) with its resonance frequency led to a standing surface wave between the reflectors (L). For the case that the used frequency is equal to the resonance frequency of IDT (J) (i.e. in a serial configuration), the frequency filter has a low

resistance and the signal is transmitted. If the used frequency is equal to the resonance frequency of IDT (K) (i.e. is in a parallel configuration), the frequency filter reacts like a short circuit and the signal is not transmitted. For lower or higher frequencies, the resistance of the device is high. Thus the frequency filter properties, like the upper and lower cut-off frequency of the bandpass depend on the resonance frequency of the two IDTs [60]. In their function as a fatigue testing device, the two IDTs could be loaded separately, because their pitch sizes and thus their resonance frequencies were slightly different. Thus, the choice of load frequency determined which of the two IDTs was mechanically stressed by a standing surface wave. Each IDT consisted of 93 electrodes with a length of roughly 90 μm. Similar to the 2-port resonator, the pitch size of the two IDT's was roughly 2 μm and the metallization thickness was 420 nm, which led to a resonance frequency of roughly 850 MHz.

Experimental setup

For both test devices, the same experimental setup was used. The automated setup consists of a frequency synthesizer as signal source, an amplifier, a power meter to measure the electric power P_{mean}, which is induced into the test sample, and a network analyzer to measure the transfer function. A detailed description of the instrumental measurement setup is given in [9]. The filter properties (band pass or S_{12} transfer function) of the test devices were measured by a network analyzer.

The shape of the transfer function depends among other things on the chosen design of the SAW device, the pitch size of the IDT, the elastic properties and density of the substrate and the metallization as well as on the thickness of the metal thin film. Due to temperature changes, the transfer function can show a reversible shift [49]. Device degradation leads to an irreversible shift of the transfer function. The error for the measurement of the frequency shift out of the transfer function was roughly +/- 0.2 MHz. This error resulted from the fact that due to device degradation the shape of the function changed.

The samples were loaded at the resonance frequency of the testing device. During loading, frequency shifts due to temperature changes as well as damage formation were compensated by changing the load frequency. Thus the stress maxima and nodes of the standing surface wave stayed at the same locations within the metallization. 27 tests were carried out for both designs at three different ambient temperatures (303, 333 and 357 K), three different experimental times (2, 8 and 16 h, equal to $6.1 \cdot 10^{12}$, $24 \cdot 10^{12}$ and $49 \cdot 10^{12}$ cycles at 850 MHz) and three different powers (10, 30 and 50 mW).

Microstructure and damage analysis

For both SAW test device designs a FIB microscope (FIB 200xP, FEI) was used for the qualitative microstructural analysis. The quantitative grain size analysis was performed by image analysis on FIB micrographs. Before imaging, the oxide layer was sputtered away by the ion beam. For better contrast, a tilt angle of 35° between sample normal and the ion beam was used. The grain size was automatically analyzed by the use of an image analysis tool (Quantimet, Leica). For the grain size analysis, an area of about 45 µm² was examined, which is equivalent to more than 165 grains per sample. The average grain size was defined as a diameter of a circle with an area equal to the measured average grain area.

Quantitative damage analysis at the 2-port device

The quantitative measurement of the extrusion in the continuous film was performed using an AFM (Explorer TMX 2000, Topometrics). To be able to differentiate extrusions protruding close to another, a tip with a high aspect ratio and a cone angle of 15° was used (SuperTip, Thermometrics). The examined area was 400 µm² per sample.

Commonly, the fatigue lifetime of metals is measured as a function of nominal strain amplitude. Unfortunately the cyclic strain or stress induced by surface waves can not directly be measured. However, Kubat et al. [8] were able to calculate the strain amplitude for the 2-port resonator as a function of the applied electrical power. The calculated cyclic surface displacement amplitude could be verified by the use of *in situ* AFM measurements [8]. Hence we are able to calculate the stress amplitude from the applied electrical power in the continuous metallization of the 2-port resonator. Because the damage formation and the frequency shift of the device are directly correlated (see chapter 3), a frequency shift of -0.6, -1.0 and -2.5 MHz was defined as "fatigue lifetime". The number of cycles to reach these limits was extracted from frequency shift versus time plots.

Quantitative damage analysis at the L-type device

For the quantitative analysis of the damage structure at the finger elements of the L-type device, FIB micrographs were used. From top view FIB micrographs the projected length and width of the extrusions were measured by a vector based graphic program. Measuring the projected extrusion length could result in an error if the extrusion was bent relative to the substrate. The error of the length measurement also depended on the calibration of the FIB

microscope and the resolution of the images. This error could be roughly estimated to be +/- 5%. The examined electrode length amounts roughly to 700 μm per sample.

For the measurement of the extrusion density distribution parallel to the wave propagation direction (x-axis), each of the 108 electrodes was examined along a length of about 17 μm per electrode.

A log-normal distribution function was fitted to the measured extrusion length distribution by the use of a data visualization program (Origin 7, OriginLabs)

4.3 Results

4.3.1 Microstructural damage analysis in 2-port devices

Fig. 4.3 shows the stressed metallization (temperature T = 358 K, mean electrical power P_{mean} = 1.1 mW, experimental time t = 1 h which is equal to $3.2 \cdot 10^{12}$ cycles) of the continuous film in the cavity of the 2-port resonator. The damage structure can be categorized into 4 different types:

(1) voids at the grain boundaries,

(2) extrusions at the surface (*high aspect ratio extrusions*),

(3) disappeared grains and

(4) whole grains protruding out from the surface (*grain like extrusions*).

Cross section (5) and (6) (prepared and imaged by FIB) show the difference between the extrusions growing out of the grain boundaries and grains growing out of the top surface. The height of extrusions growing out of the grain boundaries often reaches more than the film thickness, while their diameter is only half the film thickness. The height of the grains protruding out of the surface of the metallization reaches typically 1.5 times the film thickness while their diameter is larger than the film thickness. These grains (4) have a characteristic shape: the section protruding out of the surface of the metallization has the form of a frustum of a pyramid. Cross section (6) shows that this is also true for the diameter of the grains at the interface to the substrate. In most cases these two types of extrusions can easily be differentiated from tilted top view images by their height/width aspect ratio and their shape.

Cross section (7) and (8) shows that voids are localized at the grain boundaries. They can be found at the interface to the substrate as well as near to the surface or even at the middle of the grain boundary. As can be seen in the cross section (7), the voids at the grain boundary (1) also reach from the surface of the metallization to the interface between the metallization and the substrate.
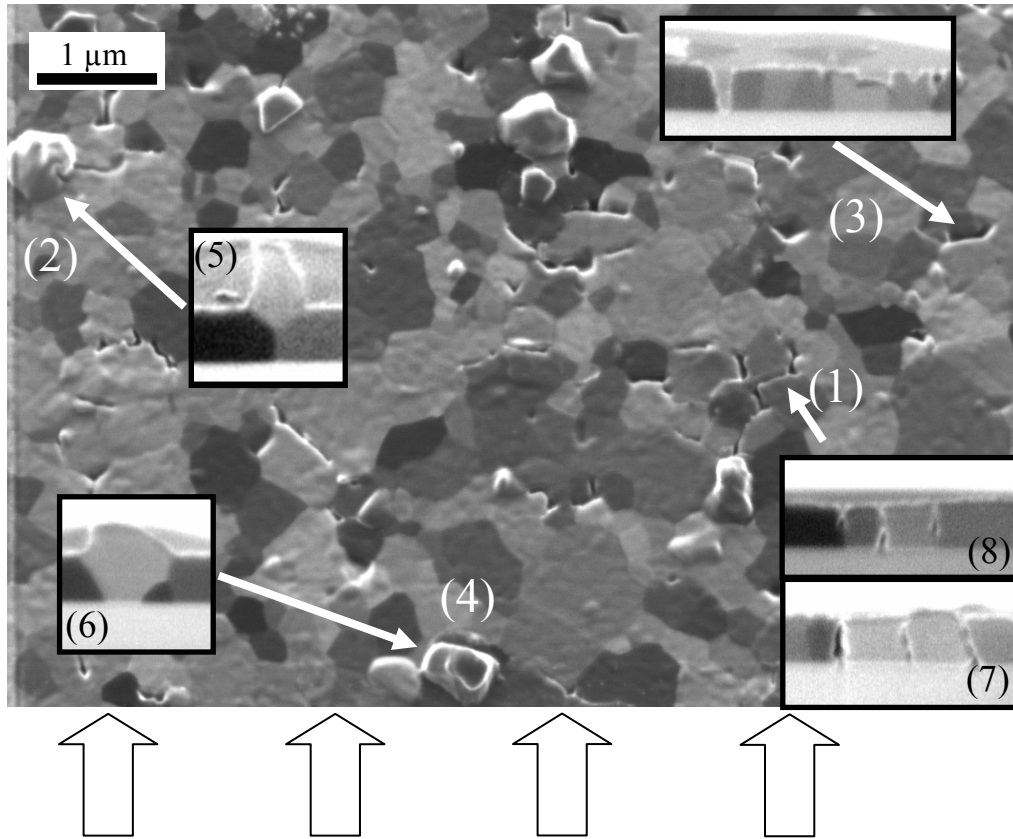
Fig. 4.3: FIB image of a 400 nm thin pure Al film stressed by standing surface wave (cavity of the 2-port resonator, $T = 358$ K, $P_{mean} = 1.1$ mW, $t = 1$ h ($3.2 \cdot 10^{12}$ cycles), $\Delta f = -1.86$ MHz) with a tilt angle of 25°, after sputter cleaning. The damage structure consists of grain boundary grooving (1), extrusion squeezed out of the surface (2), disappeared grains (3) and grains growing out of the surface (4).

The 5 small inlays show cross sections of similar damage structures of this Al thin film. These images were taken at a tilt angle of 45°. Therefore, the height of the images was stretched by a factor of 1.41 and the contrast adapted. The extrusions at the surface are localized at the grain boundary of the metallization (5). Grain growth leads to grains protruding out of the surface (6). Pores can be found at the grain boundary (7, 8).

As the test device was stressed its resonance frequency, the maxima of the acoustic wave stayed at the same site. The four arrows at the bottom of the figure point to sites of the stress maxima induced by the standing SAW.

For the quantitative analysis of the damage formation in thin Al films induced by SAW the developing extrusions at the surface were measured by the use of an AFM. The plot of the frequency shift versus the number extrusion per film volume, which is defined as the extrusion density, in Fig. 4.4 shows a linear dependency for the continuous film.
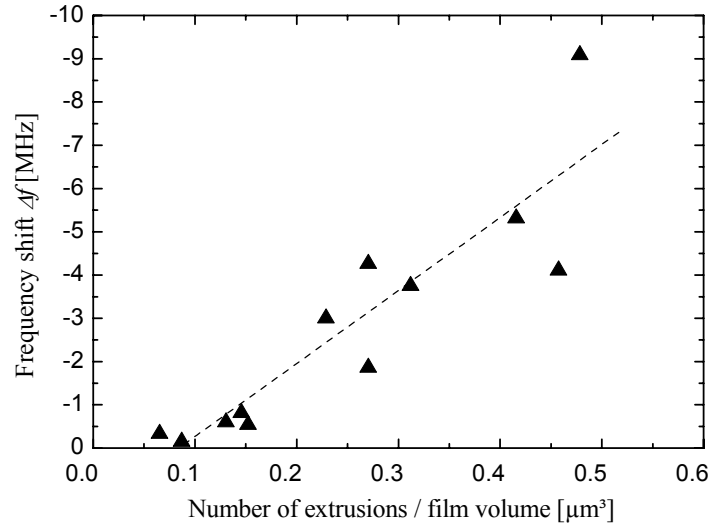
Fig. 4.4: The frequency shift of the transfer function (with an error of +/- 0.2 MHz) plotted versus the extrusion density (number of extrusions per film volume) for the continuous film (Tab. 8.4). The dashed line is a linear fit of the number of extrusions.

The fatigue lifetime N_f (number of cycles to failure) of Al thin films is shown in Tab. 4.1 for the three different frequency shifts of -0.6, -1 and -2.5 MHz. At lower electric powers higher number of cycles to failures were reached.

P_{mean} [mW]	σ_a [MPa]	$\varepsilon_{a,\,tot}$ [%]	N_f at -0.6 MHz	N_f at -1 MHz	N_f at -2.5 MHz
1.6	13.8	$2.0 \cdot 10^{-2}$	$1.3 \cdot 10^{13}$	$2.6 \cdot 10^{13}$	$9.4 \cdot 10^{13}$
3	19.1	$2.7 \cdot 10^{-2}$	$3.88 \cdot 10^{12}$	$8.1 \cdot 10^{12}$	$2.8 \cdot 10^{13}$

Tab. 4.1: P_{mean} is the mean electrical power induced into the sample device, from the cyclic stress amplitude σ_a which was estimated from P_{mean} after [8]. $\varepsilon_{a,\,tot}$ is the cyclic mechanical strain amplitude, calculated by the use of Hooke's law from cyclic stress amplitude σ_a (with a Young's modulus of 70 GPa for Al). As failure criterion three frequency shifts of the transfer function (-0.6, -1, -2.5 MHz) were used (Fig. 8.1). N_f is the number of cycles after which the fatigue criterions was reached.

4.3.2 Microstructural changes in L-type devices

Both FIB images in Fig. 4.1 were taken from the same L-type device after the fatigue experiment. Due to the L-type design both IDTs of the device were stressed at the same frequency, in this case with the resonance frequency of the IDT in Fig. 4.1b. In the resonant case, the Surface Acoustic Wave amplitudes were much higher and led to a massive degradation of the metallization: the grains grew, voids and extrusions formed.
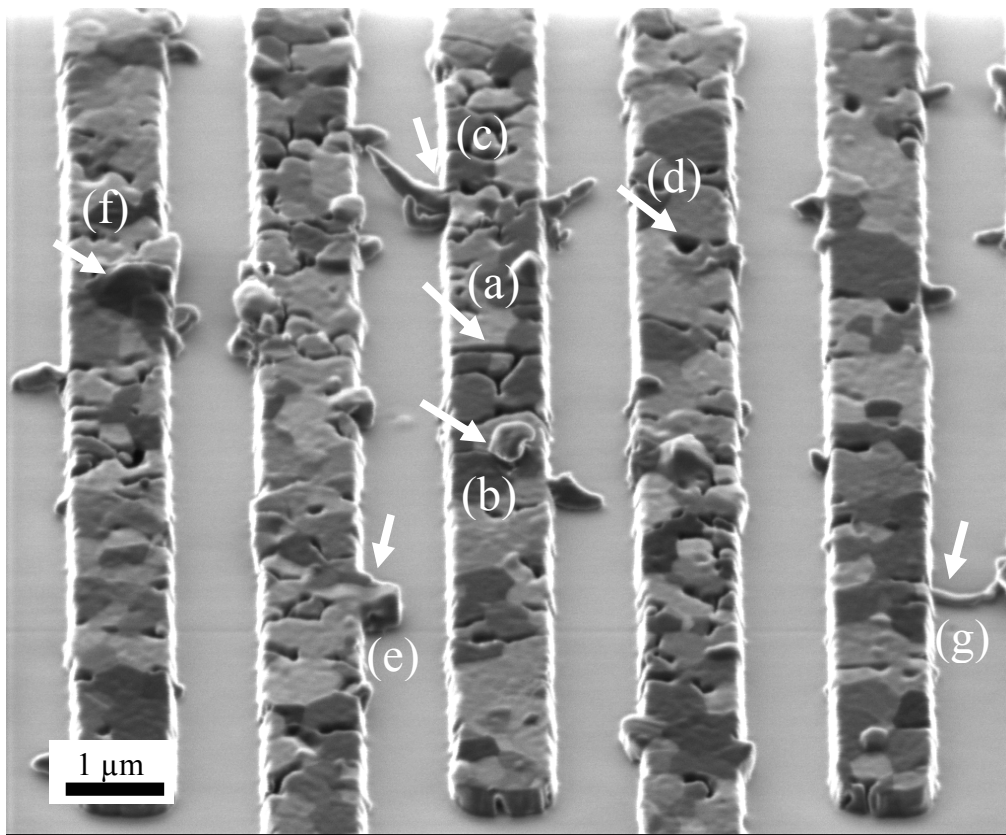
Fig. 4.5:   FIB image of 400 nm thin pure Al electrodes stressed by a standing surface wave (comb structures of the serial IDT of an L-type SAW resonator, $T = 358$ K, $P_{mean} = 31$ mW, $t = 2$ h equivalent to $3.2 \cdot 10^{12}$ cycles). Different damage formations can be seen: (a) voids at grain boundaries, (b, c) extrusion squeezed out of the surface, (d) sunken grains and (e, f) grains protruding out of the surface. High aspect ratio extrusion at the side of the electrodes can be even longer than the distance between the fingers (g).

The resulting damage structure in the electrodes of the L-type device is only slightly different from the continuous film in Fig. 4.3. In Fig. 4.5 the four types of damage formation observed in the continuous film can also be found in the electrodes: (a) void formation at the

grain boundaries, (b, c) extrusion formation at the surface, (d) sunken grains and (e, f) grains protruding out of the surface. The extrusions at the side of the fingers (c) are longer than the extrusion at the top (b), while their width is comparable. These *high aspect ratio extrusions* at the side of the electrodes can get even longer than the gap between the fingers of the comb structures (g), leading to short circuits. All of these *high aspect ratio extrusions* are located at grain boundaries, as verified by analyzing the channeling contrast from FIB images at different tilt angles, similar to the cross section (5) in Fig. 4.3 for some extrusions growing out of the surface of a continuous film.

The result of the microstructural damage can be seen in Fig. 4.6. The FIB micrograph shows a detail of a stressed IDT with the lower comb structure (dark) being isolated while the upper one (bright) is grounded. For an as deposited structure the fingers of the comb structure are expected to be alternating bright and dark for this condition. In the case of the fatigued IDT, some of the lines lost connection as visible from the change from light to dark e.g. at arrow (I). The arrow (II) points to a line that is expected to be dark but appears bright. This effect is caused by an extrusion that has grown across the gap between the electrodes leading to a short circuit.
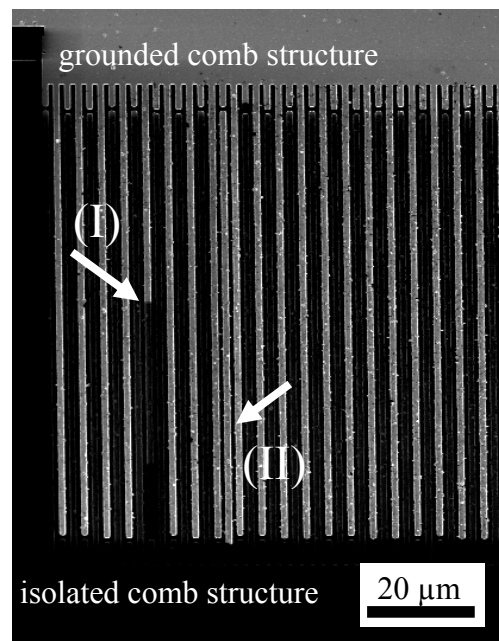
Fig. 4.6: The FIB image shows a detail of a stressed L-type IDT with the lower comb structure being isolated while the upper one was grounded. Two effects which can directly be observed are the occurrence of an open circuit (I) of the electrodes by grain boundary voiding and short circuit formation (II). The tested metallization was pure Al on a $LiTaO_3$ substrate

For the quantitative microstructure and damage analysis we compare measured values for grain size, extrusion length and density to the observed frequency shift of the device. The grain growth in the electrodes of the L-type device due to the ultra high frequency load is shown in Fig. 4.7 (see chapter 8.1 for data table). With decreasing device performance a significant increase of the grain size is observable. The measured grain size is plotted versus the frequency shift of the device in Fig. 4.8. The frequency shift of the transfer function is a commonly used value to observe the sample state. The average grain size of the 420 nm thin pure Al in the electrodes of the L-type device before loading is 320 nm. With increasing degradation the grains grow up to a size of roughly 550 nm. From that point on, grain growth saturates at a frequency shift of -1.2 MHz. Test devices which are stressed until the frequency shift reaches -2.5 MHz and more do not show further grain growth. The distribution function of the grain size was measured for a number of samples, for which a log normal function fitted very well (Fig. 8.2).

Ion beam induced grain growth, reported for Cu and Au [61], was not observed in the degraded samples. In the case of as deposited metallizations a small but observable ion beam induced grain growth could be observed during grain growth analysis.

Frequency shift [MHz]	Al (420 nm) 500 nm
- 0.0	
- 0.5 +/-0.2	
- 0.9 +/-0.2	
- 1.7 +/-0.2	
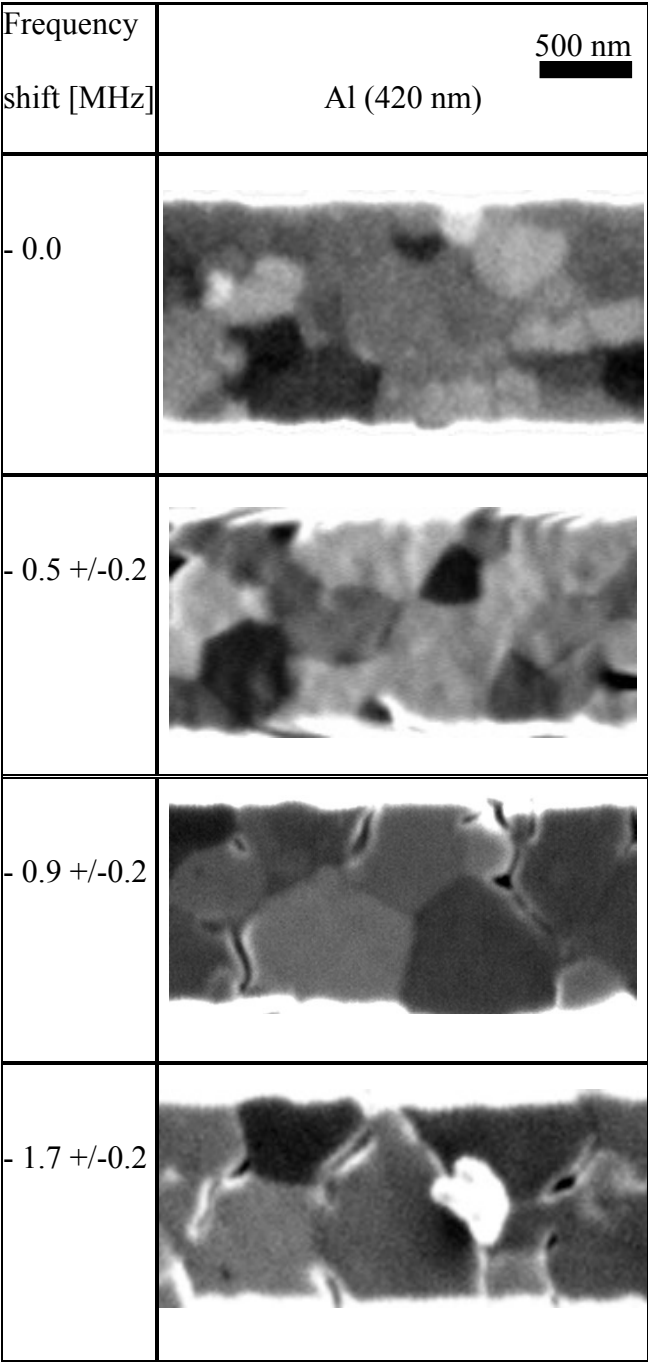
Fig. 4.7:   FIB micrographs of L-type fingers show the grain structure at different device performance states (0, 0.5, 0.9 and 1.7 MHz frequency shift of the transfer function, see data Tab. 8.7).
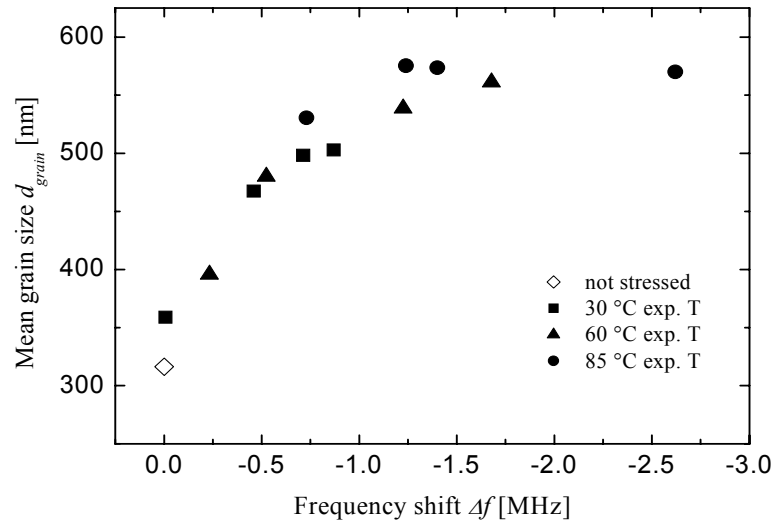
Fig. 4.8: The mean grain size versus the frequency shift (with an error of +/- 0.2 MHz) of the transfer function of an L-type test device (Tab. 8.7). Each data point represents the measurement of one test sample (see table 8.7). For the grain size analysis an area of about 45 μm² was analyzed which is equivalent to between 165 and 644 grains per sample. The degradation was reached by different test powers and testing times.

4.3.3 Quantitative analysis of damage formation in L-type devices

For the quantitative analysis of the damage formation in patterned Al thin films (L-type resonator) induced by surface waves, the number of extrusions at the electrodes were measured by the use of FIB images.

The extrusion density for each electrode in direction of the (x-axis) in Fig. 4.9 for a Cu containing Al metallization showed a plateau in the middle of the IDT of an L-type structure. This measurement shows that the extrusion density does not change too much in the middle of the IDT. At the boundary to the reflectors the extrusion density decreased. The average extrusion length does not show a significant dependence on the location in the device.
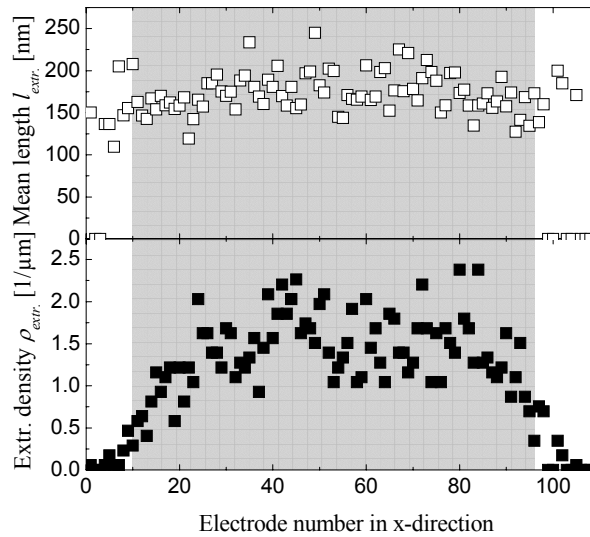
Fig. 4.9:   Extrusion density and the mean length of extrusions distribution across the IDT of a L-type device with a Cu containing Al metallization are plotted as a function of position on the device. The grey area marks the IDT while the white areas on the left and right hand side of the IDT are dedicated to the reflectors (compare Fig. 4.2b).

In Fig. 4.10 the frequency shift as well as the number of extrusions per unit volume is plotted versus the load time for an L-type test device. It can be seen that the number of extrusions developed the same way as the frequency shift. Both functions show a decreasing slope versus time.
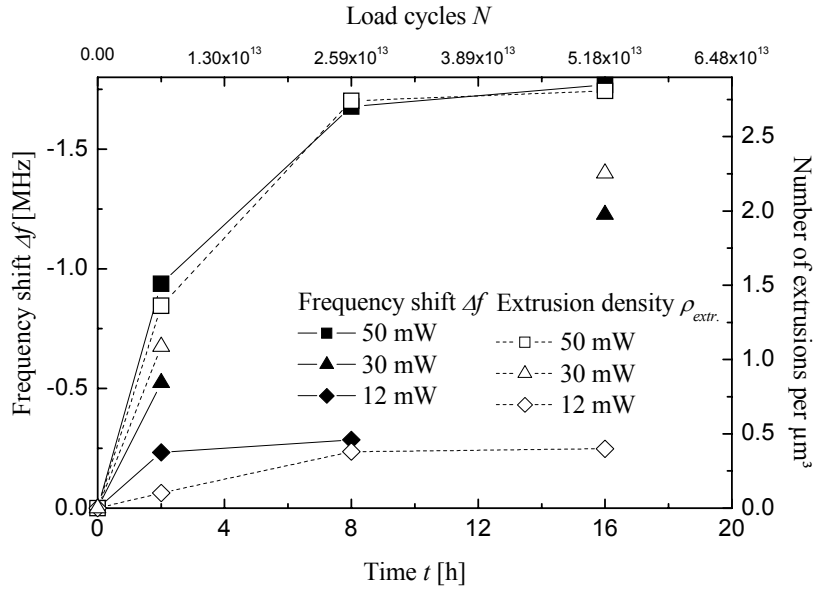
Fig. 4.10:   The frequency shift of the transfer function (with an error of +/- 0.2 MHz) of the L-type test device as well as the extrusions density for the three electrical powers is plotted versus the testing time. The sample temperature was 333 K. The sample which was loaded for 8 h at 30 mW was destroyed during the experiment.

By plotting the frequency shift versus the extrusion density, the linear correlation between these two values can be seen in Fig. 4.11 (full circles). The slope is much higher than in the case of a continuous film. In this plot all measurements are combined, regardless of their different parameters such as temperature, time or electrical power. There are no preferred deviations for the different temperatures, powers or times used in the particular experiment. The average extrusion length does not change with extrusion density. It should be noted that prior to testing a certain number of extrusions were present which are most likely formed during the annealing at 543 K.
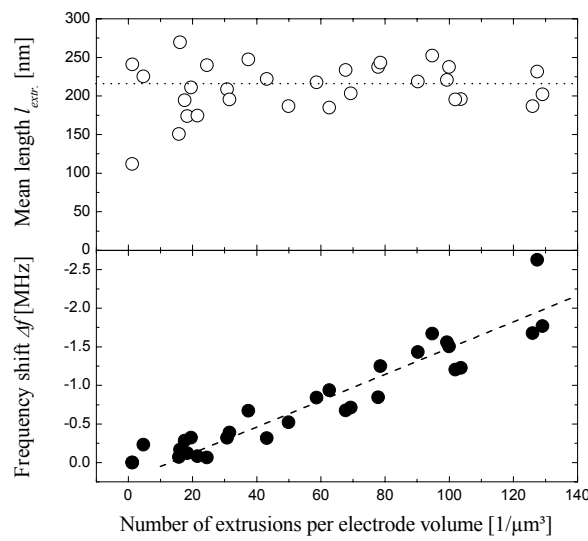
Fig. 4.11: The frequency shift of the transfer function (with an error of +/- 0.2 MHz) and the average length of extrusions plotted versus the extrusion density. The closed symbols represent the measurements of the number of extrusions for L-type test devices. The open circular symbols represent the measurements of the average extrusion length of the L-type devices. The dashed line is a linear fit of the number of extrusions. The doted line is the average length of all extrusions. For this plot, the length and width of more than 10000 extrusions have been measured. The tested metallization was pure Al on a LiTaO$_3$ substrate.

The distribution function of the extrusion length is plotted in Fig. 4.12. The distribution function shows a linear character on the logarithmic scale. From this plot the probability for an extrusion being larger than a certain value can be estimated. The results for a length of 800, 900, 1000, 1100 and 1200 nm are listed in Tab. 4.2.
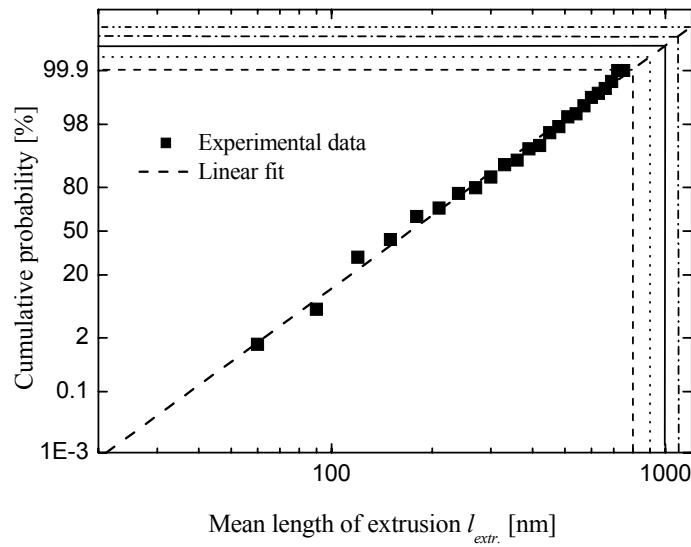
Fig. 4.12:   Measured distribution function of the extrusion length. The dashed line is a linear fit to extrapolate the cumulative probability to higher extrusion lengths. The extrapolation was used to determine the probability of different extrusion lengths in Tab. 4.2.

Extrusion length $l_{extr.}$ [nm]	Probability of an extrusion to be shorter than $l_{extr.}$ [%]	Probability of an extrusion to be longer than $l_{extr.}$ [%]
800	99.900	0.100
900	99.960	0.040
1000	99.983	0.017
1100	99.992	0.008
1200	99.996	0.004

Tab. 4.2:   Probability of certain extrusion lengths, estimated from Fig. 4.12 for later discussions.

4.4 Discussion

Surface Acoustic Wave devices enabled us to study fatigue effects at ultra high frequencies (900 MHz) in 400 nm thin Al metallizations. This cyclic mechanical load leads to a characteristic damage structure which will be discussed with respect to its characteristics and their influence on lifetime.

4.4.1 Continuous Al thin films

Lifetime approaches in continuous Al thin films

The present lifetime measurements at frequencies in the GHz regime have shown that Al thin films can reach up to 10^{14} cycles to failure for stress amplitudes of 14 MPa (Tab. 4.1). Even though the limitations by the film thickness [27, 28] and the influence of ultra high frequency on dislocation mechanisms [42] could be expected to reduce the fatigue process this did not lead to an inhibition. Therefore it can be followed, that even at these low stress amplitudes no fatigue limit is reached which was expected, since fcc-metals do not show a fatigue limit.

As there were only two different stress amplitudes used, a general statement concerning the influence of the stress amplitude on the fatigue life time could not be made. Therefore a comparison with other fatigue data should make it possible to estimate if the measured values are useful. Because film thickness significantly affects the fatigue behavior of metals [31], [33], [34], it is not possible to directly compare the fatigue lifetime of Al thin films loaded at ultra high frequencies with bulk fatigue data. Unfortunately no fatigue data is available for Al thin films fatigued at high stress amplitudes so far. For Cu thin films, fatigue data for 100 and 300 nm thin films are available [34] from thermal fatigue experiments. Also bulk Al and Cu fatigue data is available from cyclic tensile testing experiments [62]. By the comparison of the Al and Cu bulk data we are able to estimate the fatigue lifetime of Al thin films from the Cu thin film data.

Even if this comparison cannot provide a precise lifetime prediction, it can help to get an estimate of fatigue behavior over several magnitudes. In Fig. 4.13 the comparison between the

experimentally observed lifetimes of Al thin films with experiments of Cu thin films and experiments with bulk Cu and Al is shown. Due to the extensive character of the comparison the fatigue data derives from three different experimental setups with different cyclic stress states and different fatigue criteria. In the case of the bulk tensile test a uniaxial cyclic tensile stress was applied until the test sample broke. The thermal fatigue experiment induces a biaxial tensile or compressive stress which was applied until a crack propagated through the conducting line. In the case of the SAW devices the standing surface acoustic wave induced a cyclic shear stress leading test device degradation which was measured by the frequency shift.

The comparison between the Al and Cu bulk data shows only minor differences in fatigue lifetime compared to the thin film samples. Schwaiger et al. [31] expected that the fatigue strength scales with the increasing yield strength and strain hardening rate as film thickness is decreased. Extrapolating the Cu thin film data over several magnitudes, the extrapolation points to the Al data measured in the ultra high cycle regime.
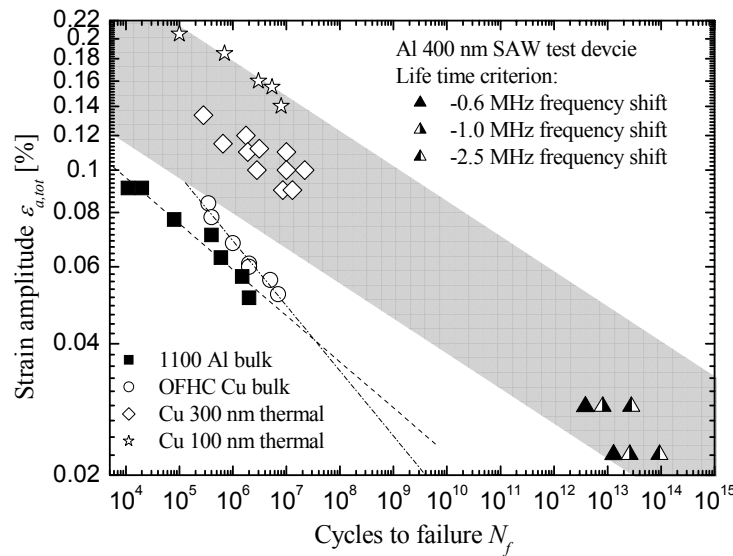
Fig. 4.13: The lifetime plot shows fatigue data of Cu thin films and 1100 Al and OFHC Cu bulk material to compare the results to the results of the Al metallization (fatigued at 900 MHz). The fatigue data of the 1100 Al and OFHC Cu bulk material data was taken from Thomson and Backofen [62], who used a tensile testing apparatus for the fatigue experiments (at several Hz). For the Cu thin film fatigue data Mönig et al. [34] used a thermal fatigue testing technique (at 100 Hz).

From that examination it might be concluded that for pure Al the linear relationship between the strain amplitude and the cycles to failure on a log-log plot is valid up to more than 10^{14} cycles.

Microstructural changes

The detailed microstructural analysis (Fig. 4.3) revealed different types of extrusions in Al metallizations:

High aspect ratio extrusions always grow out of grain boundaries and more or less look like squeezed out spikes (cross section (5)), while *grain like extrusions* are grains growing out of the surface of the metallization (cross section (6)) and *voids* (cross section (7) and (8)) are always localized at the grain boundaries and appear near to the surface as well as near to the substrate.

In-situ experiments combined with Finite Element simulations of the stress state in the metallization of L-type SAW devices in chapter 3 showed that the void and extrusion formation preferentially takes place at sites of high cyclic stresses. For continuous films we also expected damage localization since the load frequency was adjusted during the experiment [49] and thus the maxima and nodes of the standing surface waves stayed always at the same sites during experiment, even though the microstructural damage formation led to a frequency shift. The stress distribution in the 2-port resonator was calculated by Kubat et al. [6]. At a frequency of $f_0 = 900$ MHz the wavelength of the standing surface waves is roughly $\lambda_0 \approx 4$ µm and so the distance between the maxima of the standing wave is $\lambda_0/2 \approx 2$ µm. For the examined 420 nm Al thin film a slight damage localization at the cyclic stress maxima was observed in Fig. 4.3. Due to the fact, that the grain size is on the order of half of the wave length, the damage structure at the stress maxima is spread out.

4.4.2 Patterned Al thin films

Microstructural changes

Aside from the extrusion and void formation the material flux at the grain boundaries also leads to significant grain growth. With increasing frequency shift the grain size increases even in pre-annealed films (Fig. 4.7). Up to a frequency of 0.8 MHz, the measured grain size scales very well with the frequency shift as can be seen in Fig. 4.8. For frequency shifts higher than 1 to 1.2 MHz the grain size does not increase further which can be related to the voids at the grain boundaries (Fig. 4.8). Grooves and voids pin grain boundaries and inhibit further grain growth. Even though the experiments were carried out at significantly different temperatures, powers and times (see Tab. 8.7) the grain size was strongly correlated to the frequency shift.

Quantitative damage analysis

The frequency shift of the band pass of L-type devices and their measured extrusion density at the electrodes show the same progression with time (Fig. 4.10). The decreasing slope of the frequency shift and the extrusion density in Fig. 4.10 leads to the formation of a plateau, which indicates that only a limited amount of material can be activated to migrate. As the height of this plateau depends on the power and temperature, it seems that the amount of activated volume depends on the sample temperature and cyclic stress amplitude.

The good agreement between the frequency shift and the extrusion density curve denotes a direct correlation which is shown in Fig. 4.11. From the fact that the average extrusion length does not change and assuming that the measured average length is an indicator for the average extrusion volume, we can conclude that the diffused volume is proportional to the extrusion density (Fig. 4.10). Assuming that the volume of the extrusions is equal to the volume of the voids, we can conclude that the frequency shift is directly correlated to the porosity of the metallization.

Independent of the testing conditions like temperature, electrical power or testing time, all measurements show this direct correlation (Fig. 4.10). This can only be the case if the damage mechanism does not change in the examined regime of experimental parameters. It shows that our lifetime criterion i.e. of a certain frequency shift is useful because it corresponds independent of the loading conditions to the same amount of microstructural damage. Therefore it can be concluded that damage accumulation in a linear manner and in principle a Palmgren-Miner rule could be applied [63]. It has to be remarked that this behavior can change in the case of a pulsed load, where the break between the load periods can lead to stress relaxation in the metallization.

From the extrusion density distribution across the IDT and the reflectors in Fig. 4.9, the cyclic stress distribution can be estimated. In the middle of the IDT the cyclic stress level seems to be constant. Near to the reflectors the cyclic stress level decreases. This is similar to calculations of the standing wave profile in equivalent SAW structures (1-port resonator) by Ebata and Mitobe [64]. Their calculation seems to predict a small decrease of the cyclic stress from the middle of the IDT to the reflectors with an abrupt decrease at the crossover between IDT and reflector. Again, the estimated stress distribution and the extrusion length distribution show nearly no correlation.

4.4.3 Damage density and frequency shift correlation in structured films

As the relative stiffness change of the metallization is proportional to the relative frequency shift of the IDT's resonance frequency as will be shown in chapter 5 the question is how the elastic properties relate to the extrusion density. In chapter 3 it was shown that void formation always starts at sites of high cyclic stress, which are located at the lower edge of the electrodes. The void growth follows grain boundaries which are perpendicular to the electrode axis (y-direction). Thus the voids will be treated equivalent to parallel cracks in thin films which can lead to the reduction of intrinsic stresses [65]. Xia and Hutchinson solved the problem of parallel cracks in a thin film on a substrate for an equibiaxial stress state. Although in this case we have a cyclic stress state of pure shear, we can use the solution to explain the observed correlation between extrusion density and frequency shift of the band pass. Gao [66] reformulated the equation for the energy release rate at a crack tip to calculate the average intrinsic film stress $\sigma(d)$:

$$\sigma(d) = \sigma_0 - \left(\sigma_0 - \sigma_{crack}\right)\left(\frac{4 \cdot t_f}{d} \tanh\left[\frac{d}{4 \cdot t_f}\right]\right) \tag{4.1}$$

where d is the crack distance, σ_0 is the intrinsic film stress in the uncracked state, σ_{crack} is the stress at the crack and t_f is the film thickness. For the case that the stress at the crack $\sigma_{crack} = 0$, equation (4.1) can be simplified:

$$\sigma(d) = \sigma_0 \cdot \left(1 - \frac{4 \cdot t_f}{d} \tanh\left[\frac{d}{4 \cdot t_f}\right]\right). \tag{4.2}$$

This can be written as:

$$\frac{\sigma(d) - \sigma_0}{\sigma_0} = -\frac{4 \cdot t_f}{d} \tanh\left[\frac{d}{4 \cdot t_f}\right]. \tag{4.3}$$

By the use of Hooke's law we get the relative stiffness reduction of the metallization:

$$\frac{E_{effective} - E}{E} = \frac{\Delta E}{E} = \frac{\sigma - \sigma_0}{\sigma_0} = -\frac{4 \cdot t_f}{d} \tanh\left[\frac{d}{4 \cdot t_f}\right] \tag{4.4}$$

where E is the Young's modulus of the metallization and $E_{effective}$ is the virtually reduced Young's modulus because of the stiffness decrease due to the presence of cracks. For low crack densities the hyperbolic tangent is roughly 1 and the relative change of the stiffness increases linearly with crack density as Fig. 4.4 and Fig. 4.11 shows:

$$\left|\frac{\Delta E}{E}\right| \sim \frac{1}{d} \tag{4.5}$$

Assuming that the crack distance d of equation (4.4) is inverse proportional to the void density ρ_{void} and assuming, that the extrusion $\rho_{extr.}$ and void density ρ_{void} is also proportional, we can formulate the correlation between the relative frequency shift and the extrusion density:

$$\left|\frac{\Delta f}{f}\right| \sim \left|\frac{\Delta E}{E}\right| \sim \frac{1}{d} \sim \rho_{void} \sim \rho_{extr.} \, . \tag{4.6}$$

with f is the working frequency of the L-type resonator and Δf is the irreversible frequency shift.

We can now use data points from Fig 4.11 to compare the model with the experiment. The extrusion density for a 1 MHz frequency shift (which correlates to a relative frequency shift of only 0.1 % for a load frequency of 900 MHz) is equivalent to an extrusion density of $\rho_{extr.} = 0.7/\mu m$. Contrary to the low relative frequency shift at this damage density the stiffness of a thin film under static tensile stress with parallel cracks would decrease for roughly 80 % as is shown in Fig. 4.14.
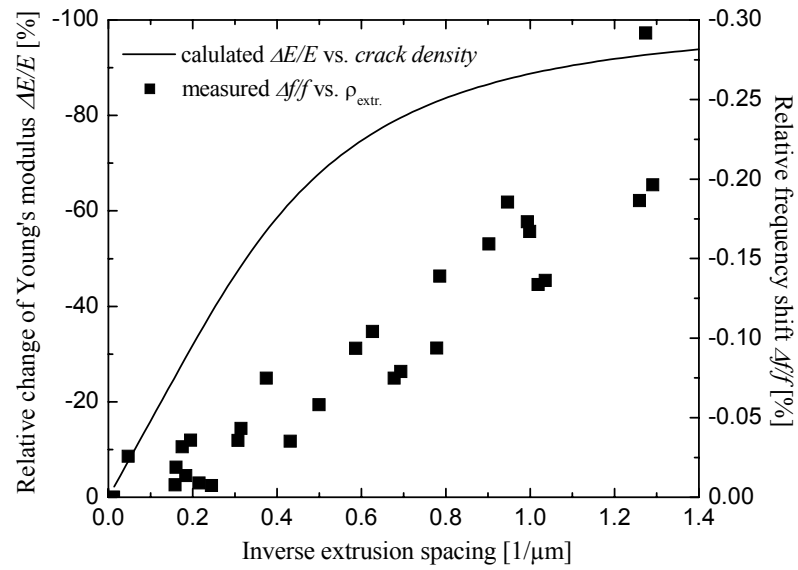
Fig. 4.14: The solid line is the calculated effective stiffness change of the metallization, plotted versus inverse crack distance (which is assumed to be equivalent to the inverse extrusion spacing) after equation (4.3), with film thickness t_f = 420 nm. The full boxes are the measured relative frequency shift versus inverse extrusion spacing of the L-type SAW devices (calculated from ρ_{extr} in Fig. 4.11 for an electrode with w_{elec} = 1.2 μm and a film thickness t_f = 420 nm).

This difference is due to three reasons:

- Only about 10 % of the acoustic wave's potential energy is located in the metallization [4]. Thus the frequency of the SAW test device is mainly determined by the substrate properties, which do not change due to the observed damage formation.

- The model of Xia and Hutchinson calculated the case where the cracks were oriented perpendicular to a static tensile stress in the film. Fig. 4.15 shows that in the case of a tensile stress the crack gets opened, and the tensile stress level at the crack decreases to zero. In a resonant device the voids can not lower the dynamic τ_{xy} stress significantly, because the stress in the metallization is induced by the inertia due to the acceleration during cyclic movement and is applied also at each atom at the crack interface. Both sides of a void at a grain boundary which is oriented perpendicular to the electrode's longitudinal axis feel the inertia forces pointing in the same direction. Thus the stress at the crack does not decrease to zero as in the case of a static tensile stress.

71

- The observed voids often do not span the whole metallization. Thus the impact of the observed voids on the stiffness of the metallization is much lower than in the case which was calculated by Xia and Hutchinson.

a)   b)
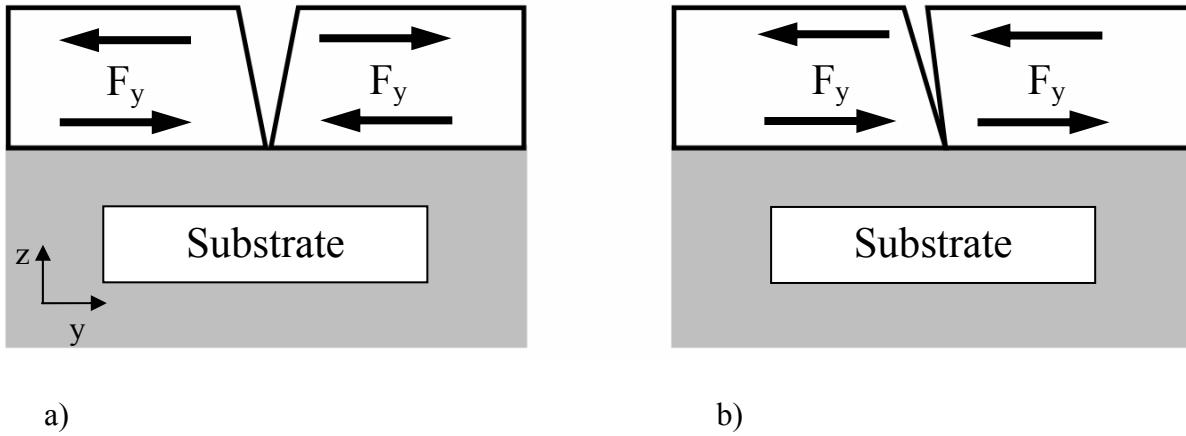
Fig. 4.15:   Schematics of the shape of the metallization near to a crack deformed by a tensile stress a) and a surface wave induced stress. b) The arrows indicate the forces in the metallization.

The direct correlation between frequency shift and extrusion density also seems to be valid for the continuous film as is shown in Fig. 4.4. However, the slope of the frequency shift versus extrusion density between the continuous and the structured film differs significantly. For an equivalent extrusion density in continuous films, the resulting frequency shift is roughly 15 times higher than in structured films. This can be attributed to two main differences:

- At the location of the kinetic energy maximum of a standing surface wave, the mass of the system plays the most important role, while at the location of the potential energy maximum the stiffness plays the major role. In L-type test structures as used in our experiments the electrode is sited at the location of the maximum deflection of the standing surface wave (location of kinetic energy maximum). The continuous film in the 2-port resonator also feels the potential energy maximum of the standing surface wave where much higher cyclic stresses are induced [6]. Thus the stiffness decrease due to the damage formation at the sites of highest cyclic stress (location of the potential energy maximum) has a much stronger influence than in the case of the patterned thin films.

- In contrast to the stress in the electrodes of the L-type resonator, the maximum cyclic stress in the continuous film of the 2-port resonator is the τ_{xy} component [6] For a columnar grain structure as was found in the used test devices, the grain boundaries and thus the voids can be oriented parallel to the induced shear stress as can be observed in Fig. 4.3. Hence the voids in the continuous film have a much higher influence on the effective stiffness.

- From a mechanical point of view, the theoretical minimum of the relative eigenfrequency shift is reached when all the grains of the electrodes material are disconnected from each other due to void formation at the grain boundary. This limit depends only on the grain size of the metallization material.

4.4.4 Short circuit probability

Since it was shown that the *high aspect ratio extrusions* can reach lengths which enables them to bridge the gap between the electrodes l_{gap} [17], they can have a high influence on device reliability. In Fig. 4.6, this could be observed in one of the L-type resonators. Thus we will define the existence of one extrusion which is able to bridge the gap between two neighboring electrodes to be enough for a fatal failure of a test device. This is a very conservative reliability criterion since qualitative observations showed that for a short circuit leading to a sudden failure of a test device usually more than one extrusion is needed.

The short circuit probability mainly depends on the probability $P_{extr.>gap}$ of an extrusion reaching l_{gap} and the total number of extrusions $N_{extr.}$. Assuming that the probability of a certain length of an extrusion is independent of the rest of the extrusions, we can calculate the probability $P_{extr.<gap}$, which is the probability that there is no extrusion being longer than l_{gap}:

$$P_{extr.<gap} = \left(1 - P_{extr.>gap}(D_{extr.}, l_{gap})\right)^{N_{extr.}} \qquad (4.7)$$

The probability P_{short} of a short circuit in a device can be written as:

$$P_{short} = 1 - P_{extr.<gap} . \qquad (4.8)$$

P_{short} can than be calculated by combining (4.6) with (4.7):

$$P_{short}(N_{extr.}, l_{gap}) = 1 - \left(1 - P_{extr.>gap}(D_{extr.}, l_{gap})\right)^{N_{extr.}} \tag{4.9}$$

For a quantitative comparison of the short circuit probability for different electrode gaps l_{gap}, we can estimate the probability $P_{extr.>gap}$ (l_{gap}) from the measured distribution function of the extrusion lengths (Fig. 4.12). By the use of the measured probability $P_{extr.>gap}$ in Tab. 4.2 and from the total electrode length times the extrusion density we can calculate the total probability of a short circuit. Fig. 4.16 shows how the short circuit probability function scales with the frequency shift for different electrode gaps. With increasing damage density, which is proportional to the frequency shift, the probability of a short circuit increases exponentially. Typically, the life time is defined by the filter properties i.e. by a maximum frequency shift of 1 MHz as is shown in Fig. 4.16 by the grey box. For an electrode gap of 1000 nm the short circuit probability in the test device increases significantly for frequency shifts higher than 0.1 MHz. In this regime, the prevention of short circuits gets the major reliability criterion as short circuits significantly reduce the lifetime of SAW test devices.
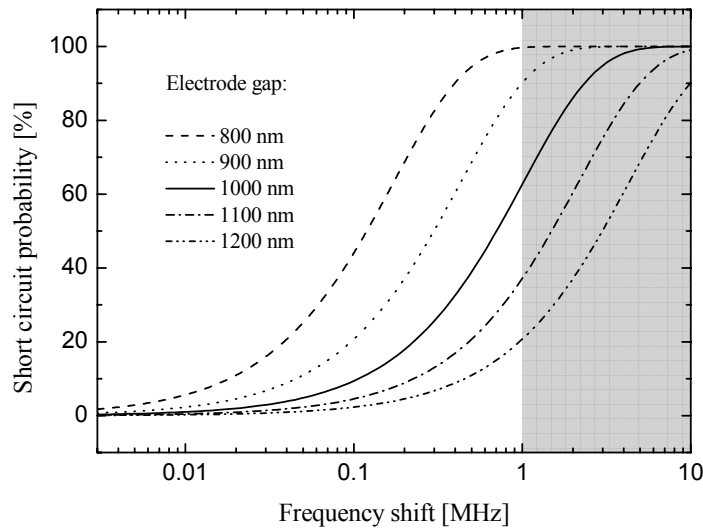
Fig. 4.16:   Probability of a short circuit for different electrode gap lengths of an L-type test device. The total extrusion number was calculated from the measured extrusion density and the total electrode length of the device (93 electrodes times 90 μm length and 0.7 / μm extrusion density taken from Fig. 4.14).

Aside from the electrode distance as a design parameter for the device, it is also important to control the microstructural parameters, especially the distribution function of the extrusion length. Two parameters are important for the extrusion length distribution and thus important for the probability of a short circuit: the mean extrusion length and the standard deviation of the distribution. A change of the mean extrusion length leads to a shift of the distribution function to smaller extrusion lengths, while a decrease of the standard deviation would increase the slope of the distribution function as is shown in Fig. 4.12. From qualitative observations we know that there is an interrelation between the extrusion length and the grain size distribution. This interrelation can be utilized to control the extrusion length distribution and thus control the reliability of SAW devices by changing the mean grain size and distribution.

4.5 Summary

By the use of SAW devices, fatigue experiments with Al thin films were performed at ultra high frequencies (900 MHz).

- The detailed damage analysis of continuous and structured thin Al films revealed that extrusion and void formation, induced by cyclic mechanical load at ultra high frequencies, is always located at the grain boundaries.

- Cyclic load at these frequencies leads to a considerable grain growth even at room temperature.

- For patterned metallization in SAW devices a direct correlation was observed between device performance (frequency shift of the band pass) and the microstructural damage density in the electrodes. This direct correlation can be explained by the stiffness decrease of the metallization due to void formation at the grain boundaries.

- The measurement of extrusion length distributions enabled us to estimate the probability of failure of SAW devices due to extrusions bridging the gap between the fingers depending on the damage density and electrode distance.

- At stress amplitudes of 14 MPa the Al thin films (420 nm) reach up to 10^{14} cycles to failure and do not show a fatigue limit which was expected, since fcc-metals do not show a fatigue limit.

5 Fatigue damage and frequency shift at ultra high frequency: a Finite Element analysis

Abstract: Ultra high-cycle fatigue at frequencies in the GHz regime leads to a characteristic void and extrusion formation in patterned metal thin films. Resulting from the microstructural damage formation a significant degradation in form of a shift of the resonance frequency in Surface Acoustic Wave (SAW) test devices takes place. In the present chapter, we analyze in detail how the damage density leads to the observed frequency shift. It will be shown that advanced Finite Element (FEM) calculations simulate very well the sensitivity of the resonance frequency to damage structure in the interconnects such as cracks, voids and extrusions. The experimentally observed linear correlation between damage density and frequency shift is reproduced by the FEM model. Furthermore, the FEM simulations predict a significant deviation from the linear correlation for very high damage densities.

5.1 Introduction

Cyclic mechanical load at ultra high frequency induces characteristic damage in metal thin films. In previous work [4, 10] the formation of extrusions and voids in Surface Acoustic Wave (SAW) frequency filter devices has been observed, accompanied by a shift of the frequency of the band pass. The Al thin film interconnects in these devices had to withstand a cyclic mechanical load at frequencies of several hundred MHz to some GHz. In chapter 3, we described a direct correlation between damage density and frequency shift. In this chapter, we aim to explain this correlation by way of Finite Element modeling.

It is assumed that the decrease of stiffness due to void formation is the main cause for the frequency shift. The correlation between porosity and stiffness for bulk materials is well established. The major factors beside the amount of porosity are the shape of the pores and their orientation with respect to the major components of the stress state [67, 68]. In the case of thin films, the rigid bond of the film to the substrate with a high Young's modulus plays an important role because the substrate provides a stiff support near a crack or a pore. Thus, a single crack lowers the effective stiffness only in a region with a size of the order of the film thickness [65]. In chapter 4 a model of Xia and Hutchinson [65] is applied to describe the stiffness decrease in the electrodes by void formation induced by fatigue at ultra high frequencies. This model provides an analytical solution for the tensile stress relaxation in a thin film on a substrate due to parallel cracks. In chapter 4 this model is used to predict qualitatively the experimentally observed linear correlation (chapter 3) between damage density and device performance. Nevertheless, a quantitative comparison with experimental data is not possible on the basis of the analytical model, because the substrate effects needs to be included in order to predict the decrease in stiffness of the interconnect/substrate composite.

In this chapter, we focus on the correlation between the characteristic microstructural damage, described in the previous chapters, and its influence on the resonance frequency by the use of a Finite Element Method (FEM) analysis. In order to obtain a detailed understanding of the influence of the damage morphology on the device performance cracks, voids and extrusions will be examined separately. It will be shown that the comparison of the

simulation to the experimental observations give important insight which damage situations are most detrimental for device performance.

5.2 FEM model

The influence of damage induced by the cyclic stress at ultra high frequencies on the eigenfrequency of the system was calculated by the use of a commercial FEM program (multiphysics module, ANSYS 7.0). The eigenfrequency of the system was calculated by a modal analysis [69]. For visualization of the resulting modes, the post processor of ANSYS 7.0 was used, and the relevant modes of the model were determined.

The geometry of the FEM model is shown in Fig. 5.1. Absolute numbers for line width and height are chosen in the typical regime for a SAW device with a height of 420 nm and a width of 1 μm. The substrate was twice as wide as the interconnect with a width (x-direction) of 2 μm representing a spacing between interconnects being equal to the interconnect width. The thickness of the substrate (z-direction) was limited to 4 μm in order to reduce computation time. An increase in substrate thickness by the factor of 2 lead to a relative frequency shift of the model of less than one percent (Fig. 8.3). The length (y-direction) of the FEM model has been varied for the modeled segment in order to simulate different damage densities. As boundary conditions, the surfaces of the substrate normal to the x-axis, and the bottom surface of the substrate (normal to the z-axis) were fixed in their position. The latter reflects the fact that in a real device the substrate is much thicker providing a rigid body. For the simulation, it is sufficient to model the surface only because the surface wave affects only a small volume. All outer surfaces normal to the y-axis were set to anti-symmetric conditions. 8-noded cubic elements (brick45) were used. By using an edge length of 100 nm for the elements, a regular mesh of prismatic elements was created. A decrease of the element size to 50 nm edge length resulted in a relative decrease of the eigenfrequency of $\Delta f/f = 5 \cdot 10^{-4}$, while the number of elements increased by the factor of eight. A further decrease was not possible, since computational time increased with an even higher factor. Therefore the absolute numbers of the eigenfrequency contain a systematic failure in the range of $\Delta f/f = 5 \cdot 10^{-4}$. The interface between the electrode and the substrate was simulated by contact elements. This allows for an easy change of the geometry when introducing damage such as voids or cracks into the structure. The properties of the contact elements were defined as 'always bonded'.

For the metallization a Young's modulus of 70 GPa, a Poisson ratio of 0.34 and a density of $2.7 \cdot 10^6$ g/m³ was used, which corresponds to the polycrystalline, quasi-isotropic material properties of Al. For the substrate a Young's modulus of 233 MPa [53], a Poisson ratio of 0.23 and a density of $7.45 \cdot 10^6$ g/m³ [54] was used, which corresponds to the material properties of LiTaO₃, again neglecting elastic anisotropy. For the contact elements, the substrate properties were chosen.
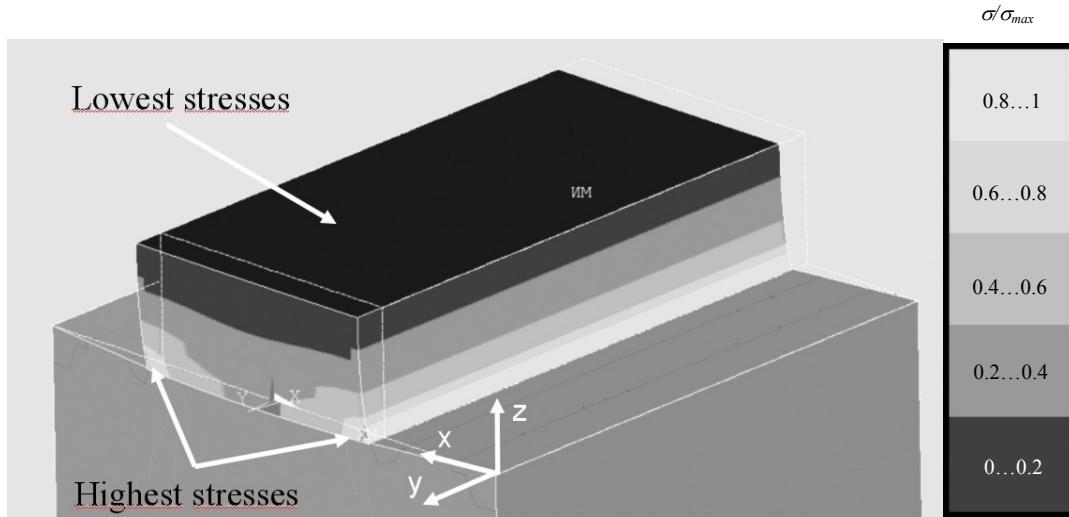
Fig. 5.1:   Calculated cyclic stress σ_{yz} at the maximum deflection in an electrode of the FEM model at an eigenfrequency of 918 MHz. Highest cyclic stresses are located at the lower edges of the electrode.

In order to validate the reduced model of only one electrode and the corresponding boundary conditions, a simulation with four electrodes (Fig. 5.2) was conducted. The electrodes had the same dimensions as in the case of the simplified model, while the substrate was two times wider. All other settings like material properties and symmetry conditions were identical. It can be assumed that at least the two inner electrodes are not affected by the boundary conditions set at the two outer surfaces with the normal parallel to the x-directions. The eigenfrequency of the larger FEM model (Fig. 5.2) was calculated to be equal to the simplified model (Fig. 5.1). The nodes of the standing surface wave in the large FEM model had exactly 2 μm distance as is simulated by the boundary conditions in the simplified model.

Therefore, the model has been reduced to the one electrode model with fixed modes at these positions for all other calculations. The smaller model allows for a finer meshing with reasonable computation times.
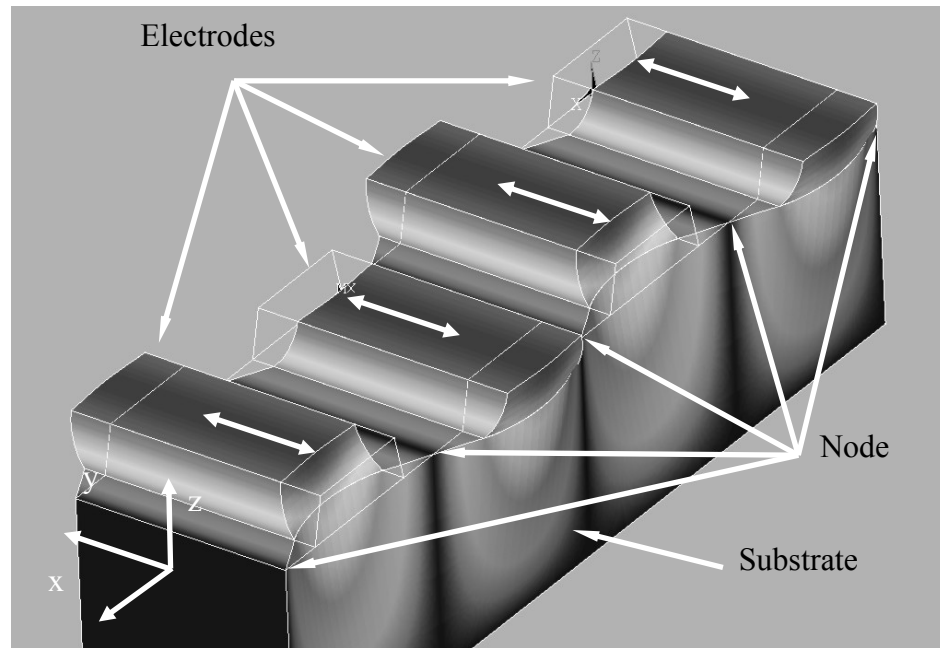
Fig. 5.2:   Calculated maximum deflection of a larger FEM model with 4 electrodes. The eigenfrequency was calculated to be 918 MHz. The white arrows aim at the nodes of the standing surface wave.

5.3 FEM simulation results

The calculated eigenfrequency of the simplified FEM model was 877 MHz (Fig. 5.1). Cracks, voids and extrusions were simulated by changing the geometry of the electrode. The geometry of the substrate and the symmetry conditions were kept unchanged. The simulations focused on changes of the device performance as a function of damage size and morphology. They are not intended to calculate stress concentrations at voids or cracks. In this chapter the effect of the material properties and the observed voids and extrusions on the acoustic properties of the electrode/substrate system will be separately simulated.

5.3.1 Inhomogeneity of cyclic stress state

First, we demonstrate the role of the compliance of the substrate for the acoustic properties of the device. For this, we calculate the cyclic stress state in the interconnect due to the inertia forces while all nodes at the bottom of the electrode are fixed. Thus the electrode behaves as if it were fixed on a perfectly rigid substrate.

As can be seen in Fig. 5.3, the electrode is sheared in y-direction exhibiting an increasing deflection with increasing height (z-axis). The cyclic stress state consists only of one component, namely σ_{yz}, The amplitude of this component depends only on the height z. The highest stresses can be found at the interface to the substrate, while the stress is zero at the top surface of the electrode. The eigenfrequency of the fixed electrode was 1960 MHz which is about twice as high as from the electrode/substrate composite.

To calculate the cyclic stress in the electrode which results from the deflection of the substrate due to the surface wave a static simulation of a deformation of the electrode at the interface was used (Fig. 5.4). For the deformation of the substrate surface at the maximum excitation of the surface wave a quadratic function was used to approximate the deflection of the nodes at the bottom face of the electrode. Therefore the nodes at the bottom of the electrode were deflected in y-direction with a quadratic function which had its minimum in the middle of the electrode.
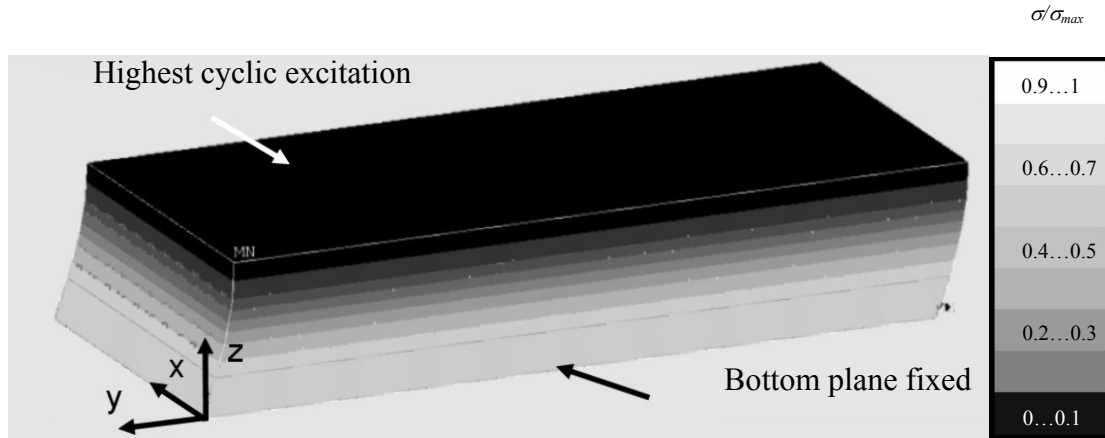
Fig. 5.3:   Cyclic stress σ_{yz} at the maximum deflection of a single electrode. The calculated eigenfrequency of the electrode, which was fixed at each node of the bottom plane, was 1960 MHz. The stress only varies with the height (z-direction).

The resulting stress state in the electrode consists of two components (Fig. 5.5, 5.6), namely the σ_{yz} and the σ_{xy} stress. The amplitude of both components decreases in z-direction. The cyclic shear stress σ_{yz} in the middle of the electrode has an opposite sign compared to the cyclic stress σ_{yz} at the edges of the finger. The cyclic stress σ_{xy} is zero in the middle of the electrode and shows its highest values at the edges of the finger where the opposite sides have opposite signs. The elements at the substrate have to sustain the highest shear stresses.

The cyclic stress state of the electrode on the substrate results from to the combination of the two stress states described above. The combination affects only the cyclic stress σ_{yz}. By the combination of the two stress states, the shear stress σ_{yz} gets larger at the edges while it gets reduced in the middle of the electrode. Thus the highest cyclic stress can be found at the edges of the electrodes.
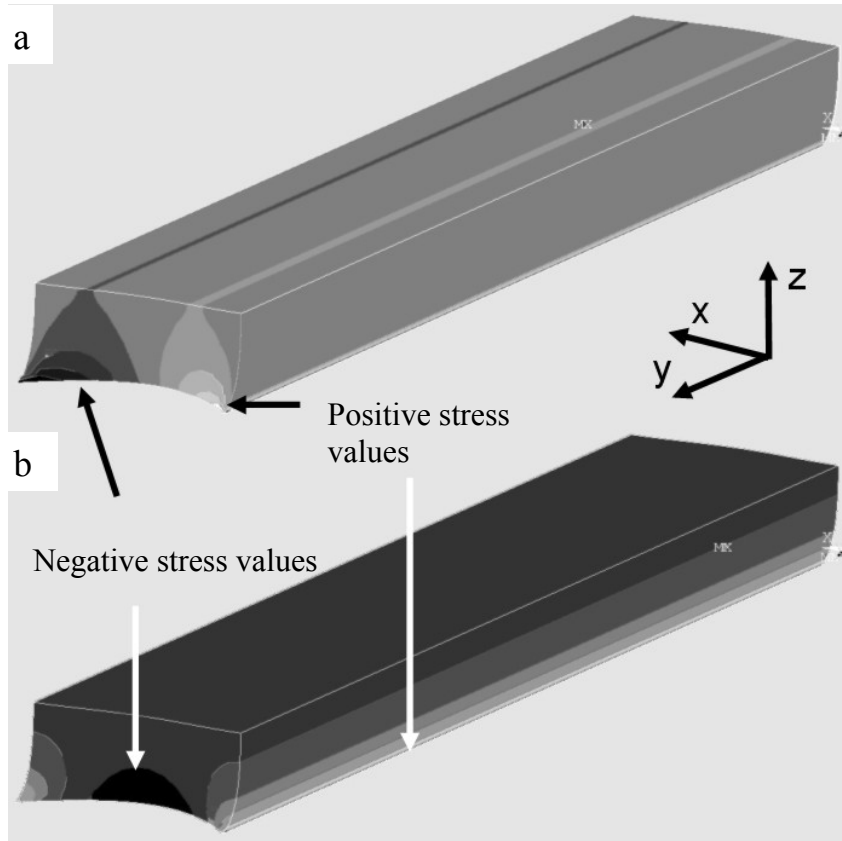
Fig. 5.4: a) Calculated static stress σ_{xy} imposed by the substrate. In the center of the electrode the cyclic shear stress is zero. The legend for the grey scale can be found in Fig. 5.5.

b) Calculated static stress σ_{yz} impressed by the substrate. The shear stress at the lower edge of the finger has the same sign like the cyclic shear stress induced by inertia forces, while the cyclic shear stress in the middle of the electrode has the opposite sign. The legend for the grey scale can be found in Fig. 5.6.
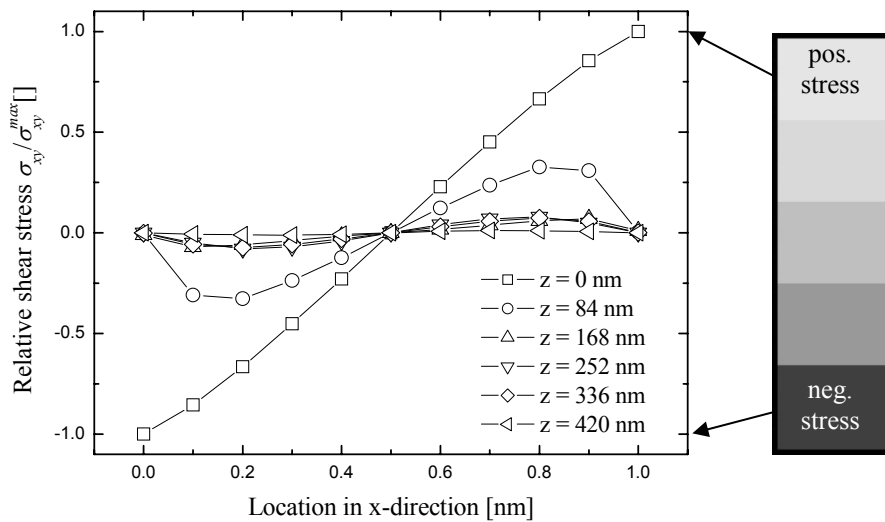
Fig. 5.5: Calculated static stress σ_{xy} imposed by the substrate versus the location in x-direction for different z-values. The stress distribution has an inversion symmetry.
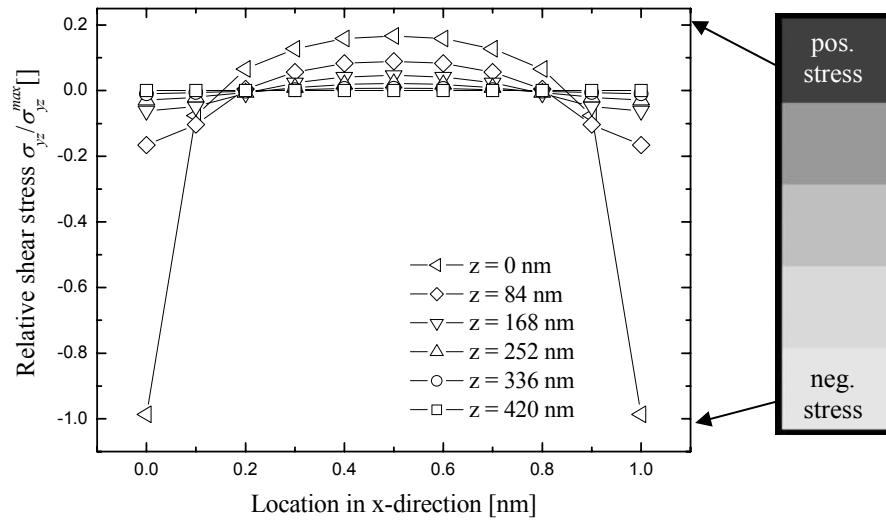
Fig. 5.6: Calculated static stress σ_{yz} imposed by the substrate versus the location in x-direction for different z-values. The stress distribution has a mirror symmetry.

5.3.2 Young's modulus and mass density changes

In order to clarify the influence of the material's stiffness and density, Young's modulus and density of the metallization were varied. As shown in Fig. 5.7 the eigenfrequency shifts linearly for small relative changes of density and Young's modulus. The sensitivity of the eigenfrequency to changes in density is much higher than to changes in Young's modulus. For relative changes in Young's modulus larger than 10 %, the function of the eigenfrequency deviates from the linear dependence. The relative density change on the other hand does not show a deviation from linearity over the entire regime investigated.
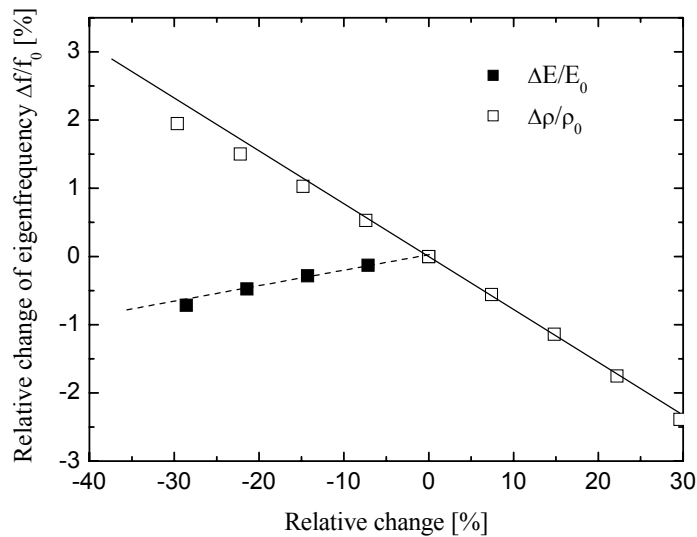
Fig. 5.7:   Relative eigenfrequency shift due to changes of the density and the Young's modulus. The lines in the plot should guide the eye.

5.3.3 Stiffness decrease

Cracks

A simple way to simulate a crack in the electrode of the FEM model is to separate the electrode at the middle by a plane normal to the y-axis, on which the nodes of the FEM model are disconnected. (Fig. 5.8). The virtual length of the used FEM model was 2 µm. The eigenfrequency of this geometry is 875 MHz compared to 877 MHz for the uncracked model. Fig. 5.8 shows that the cyclic stresses near the crack are reduced compared to the undamaged part of the electrode.
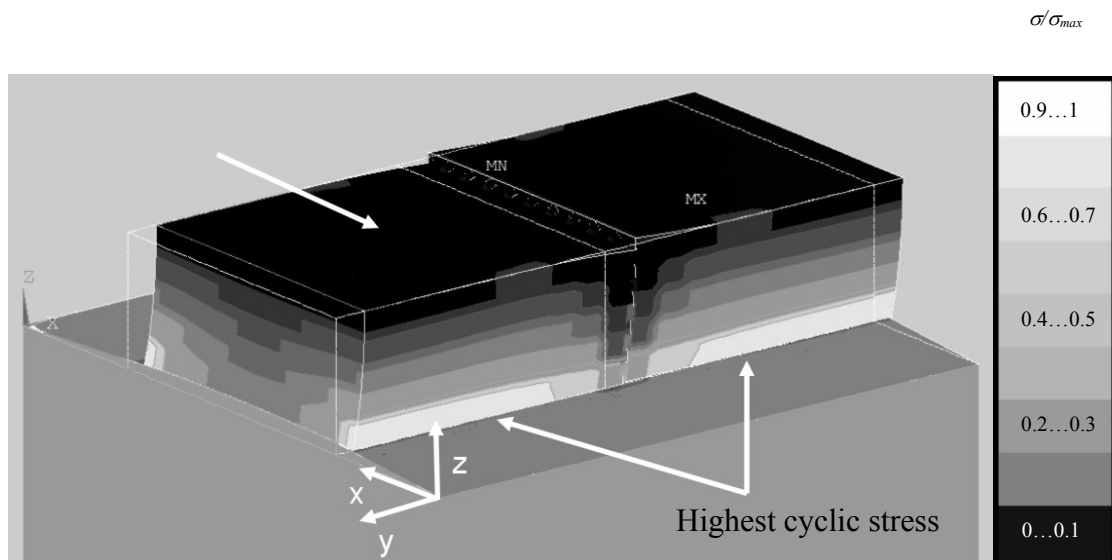
Fig. 5.8:   Calculated cyclic stress σ_{yz} at the maximum deflection in an electrode with a crack in the middle at an eigenfrequency of 875 MHz. In the region around the crack the stress amplitude is reduced.

Fig. 5.9 shows that the stress σ_{yz} at the crack location (y = 1 μm) decreases significantly but does not reach zero. The zone affected by the crack is almost one and a half times the film thickness in each direction away as highlighted by the grey area in Fig. 5.9. In this zone the cyclic stress induced by the surface wave is reduced, while the induced strain at the interface is the same as in an intact electrode.
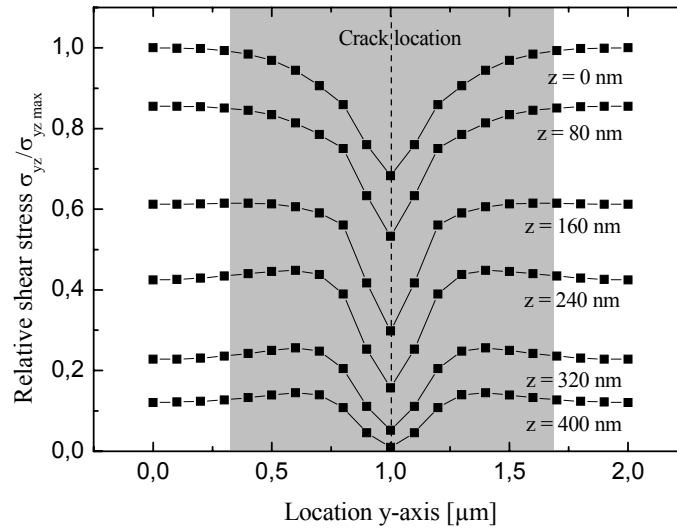
Fig. 5.9:   Stress distribution at the crack location. The grey area highlights the region next to the crack in the model where the stress is reduced.

Cracksize and location

In order to study the effect of exact crack size and location the eigenfrequency of the FEM model was calculated for different crack lengths in y-direction and crack heights in z-direction. The length of the simulated model was 2 μm for all simulations and the substrate thickness was set to 2 μm. With respect to crack length two cases were studied: first, the length of a single crack extending from one side of the electrode to the other was stepwise increased and, second, the length of two cracks from opposite sides of the electrode were increased.

The influence of the total length of a crack on the relative frequency shift is plotted in Fig. 5.10. The relative eigenfrequency shift decreases linearly with total crack length, regardless whether the crack consists of a single crack or two opposite cracks.
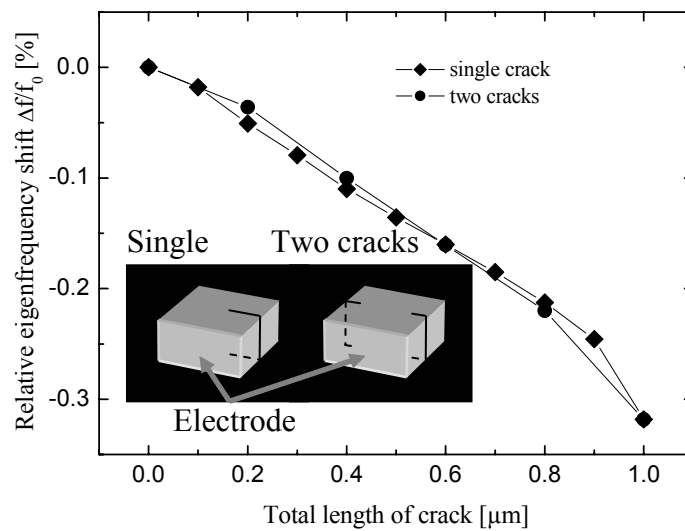
Fig. 5.10:   Relationship between total crack length and the relative eigenfrequency shift of a single crack propagating through the electrode and two cracks propagating from opposite sides of the electrode to the middle.

Also with respect to crack height, two cases were investigated: first, propagation of a crack down from the top surface to the interface, and second, from the bottom up to the surface was simulated.

The influence of the crack height on the relative eigenfrequency shift is shown in Fig. 5.11. No matter if the crack propagates up or down, the relative eigenfrequency shift decreases with an increasing slope. The comparison of the two cases shows that the crack propagating from the interface to the top surface has a stronger influence on the relative eigenfrequency shift for small crack heights.
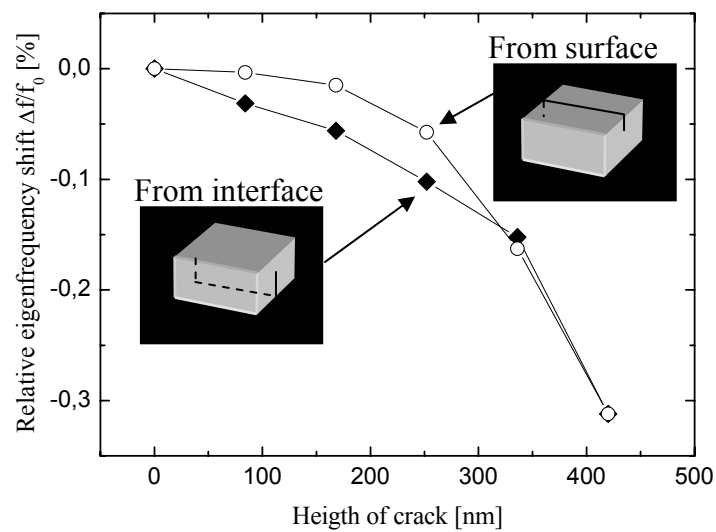
Fig. 5.11:   Influence of the crack height on the relative eigenfrequency shift. One crack propagated from surface to the interface, the other crack in the opposite direction.

5.3.4 Mass changes

Voids

In the following, the crack in the FEM model was widened to simulate a void. The total length of the simulated system was 3 µm, while the substrate thickness was 4 µm. The result is shown in Fig. 5.12, where the eigenfrequency shift is plotted versus the mass change of the electrode material. The crack itself lowers the stiffness of the electrode and the eigenfrequency of the system compared to a system without a crack. Increasing the void width leads to a linear increase in eigenfrequency with a slope of -0.0375, as the mass of the electrode decreases. The dashed line represents the relative eigenfrequency shift due to a change of the density of the electrode material as is plotted in Fig. 5.7.
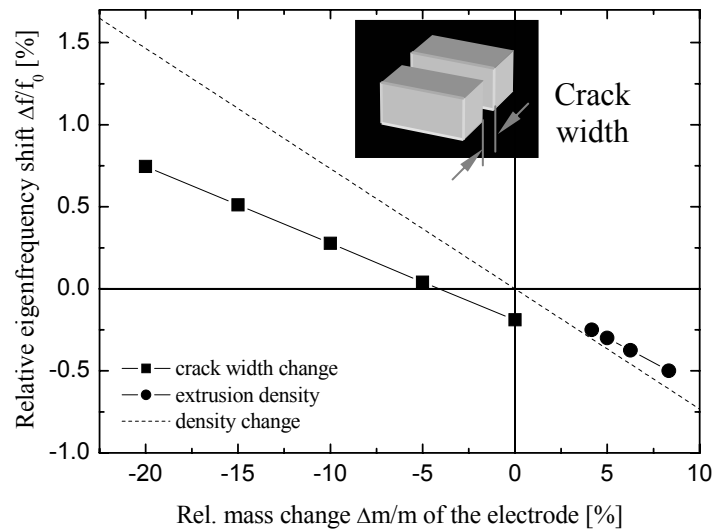
Fig. 5.12:   Relationship between the relative eigenfrequency shift and the relative mass change of the electrode for extrusion density, crack width and material density changes (Fig. 5.7). For the simulation of voids the crack width in the model was changed (closed boxes) and for the extrusion density the model length was changed while the number of extrusions were kept constant (closed circles).

Extrusions

To simulate the influence of the extrusion density on the eigenfrequency of the model, two extrusions were mounted at opposite sides of the electrodes with their center of gravity at a height of 150 nm. The width, height and length was chosen to be comparable to a grain like extrusion (300 width, 300 height and 230 length). Due to the symmetry conditions of the FEM model, an increase of extrusion density could be simulated by decreasing the length of the model in y-direction.

With increasing extrusion density, the mass of the electrode in the model increases in contrast to reality, where extrusion formation is accompanied by void formation and the mass of the electrode does not change. With an increasing extrusion density the eigenfrequency shifts linearly to lower frequencies as shown Fig. 5.12. For the situation here, the slope amounts to -0.056.

However, the influence of extrusion formation on the eigenfrequency shift depends on a number of geometrical details including their length and position in height. Therefore, models with different extrusion lengths and extrusion fixing heights (in z-direction) at the side of the electrode were simulated.

The eigenfrequency shift of the FEM model shows a strong dependence on the extrusion length as can be seen in Fig. 5.13. The grey areas in the figure mark the regime where the eigenfrequency can be calculated, while in the range of the white areas no solution has been found, since the behaviour of the FEM model is mainly determined by the extrusions in that range. In between the simulated range of extrusion length, the extrusions vibrate with three different modes as can be seen in Fig. 5.13.
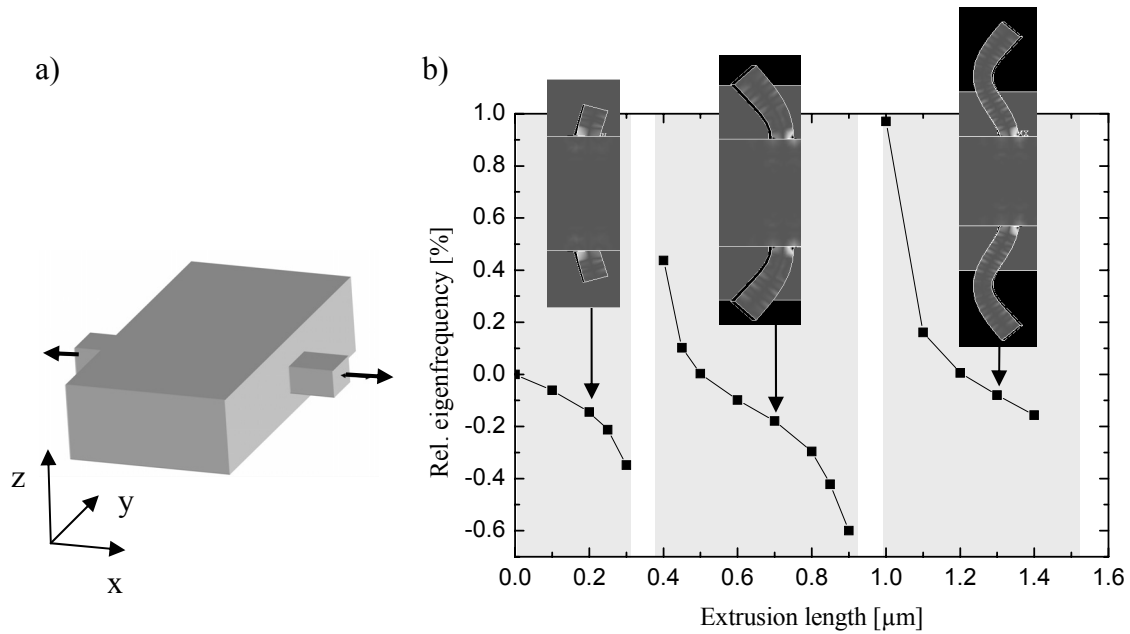
Fig. 5.13:   a) Schematics shows that only the length of the extrusions at the side of the electrode was increased. The height and the width was kept at 200 nm while the extrusion length was varied. b) Relative eigenfrequency shift for different extrusion lengths. White areas highlight the regime where the eigenfrequency of the FEM model could not be calculated. The extrusions vibrate in three different modes as is showed by the three inlays.

Fig. 5.14 shows the relative frequency shift as a function of fixing height of the extrusion at the side of the electrode. It can be clearly seen that with increasing fixing height the eigenfrequency shift increases significantly. This is because of a larger moment of inertia when the extrusion is attached near the top of the electrode (compare to Fig. 5.3).
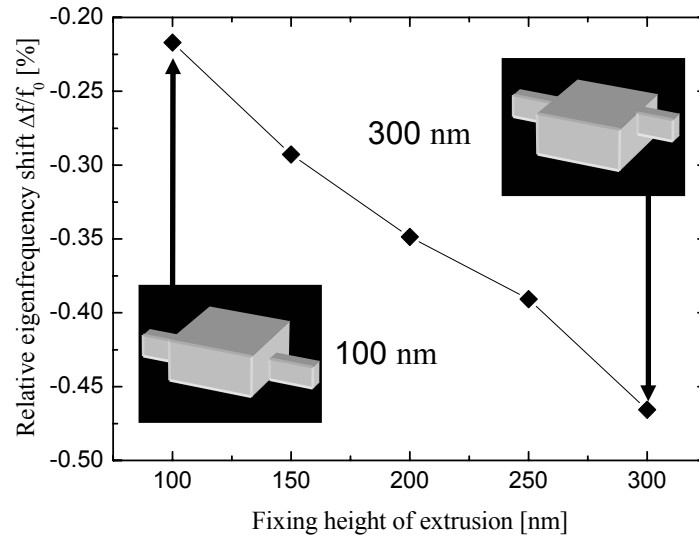
Fig. 5.14:   Relation between the fixing height of the extrusion at the sidewall of the electrode and the calculated relative eigenfrequency shift. The extrusions had width and height of 200 nm and a length of 300 nm.

5.3.5 Damage density

The influence of a crack on the eigenfrequency of the electrode can be simulated by dividing the electrode in the middle by a plane normal to its longitudinal axis (y-axis). Due to the chosen symmetry conditions in the FEM model, the crack distance is equal to the length of the FEM model. By scaling the length of the electrode and the substrate, we were able to calculate the relative eigenfrequency shift as a function of the inverse crack distance which is equal to the crack density.

For small densities, the shift in the relative eigenfrequency decreases linearly with the crack density as can be seen in Fig. 5.15. To simulate different void densities, the crack was widened to a width of 100 nm and the eigenfrequency of the FEM model was calculated for different model lengths in y-direction. The relative eigenfrequency shift of the FEM model increases linearly with increasing void density. This behavior can be attributed to a decrease in mass of the electrode. For void densities higher then $0.6/\mu m$ the function deviates from the linear behavior.

Since mass is conserved in a real electrode, the mass of the electrode does not change by void formation. Instead, mass is redistributed, namely extrusions grow at the expense of voids. Therefore, the two simulations in this context combine extrusion and voids in one model. In both experiments the void was simulated by a 100 nm wide crack in the electrode. This width was chosen since the used element size has 100 nm and therefore the nodes of the elements in the electrode and the substrate fitted well to each other. In the first experiment, the extrusions a high aspect ratio was chosen which is characteristic for hillock like extrusions. The two extrusions at the opposite sides of the electrode had a height of 200 nm and a width of 200 nm and a length of 520 nm. In the second experiment the aspect ratio of width or height versus the length of the extrusions was below 1 which is characteristic for grain like extrusions. They had a width and height of 300 nm and a length of 230 nm. In both experiments the extrusions were fixed at the half height of the film thickness of $z = 210$ nm at the side of the electrode. The schematics in Fig. 5.15 shows the structure of the FE model. The void was placed at 1/3 of the length of the FEM model on the y-axis, while the extrusions were fixed on the opposite sides of the electrodes at 2/3 of the length of the FEM model.

The relative eigenfrequency shift of the FEM model decreases linearly with increasing defect density for defect densities smaller then 0.6/µm. In the case of a crack, the relative eigenfrequency of the model decreases with increasing defect density, while for void densities smaller than 0.6/µm the relative eigenfrequency increases due to the mass reduction of the electrode relative to the substrate. In the combined model, the extrusions compensate the mass loss by the voids. In the case of high-aspect ratio extrusions the relative frequency shift for low defect densities is nearly zero. In the case of the grain like extrusion, the slope is negative and even lower than in the case of the crack. For larger defect densities the relative eigenfrequency shift deviates from the linear connection in all cases.
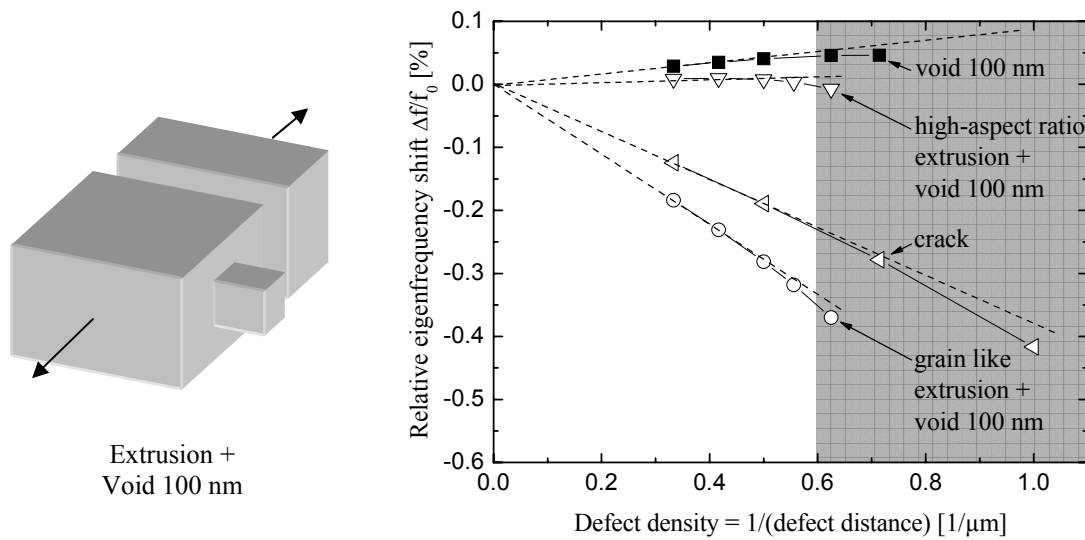
Fig. 5.15:   Relationship between the calculated relative eigenfrequency shift of the FEM model and the damage density. Four different cases were calculated: the damage consisted of a crack with zero crack width, with 100 nm crack width and two combined model of a crack with 100 nm width and extrusions with the same volume. In the case of the high-aspect ratio extrusions the width and height of the extrusion was 200 nm and a length of 520 nm while in the case of the grain like extrusion a width and height of 300 nm and a length of 230 nm was chosen. The grey area highlights the region where a slight deviation from the linear correlation between frequency shift and damage density is observable.

5.4 Discussion

The FEM investigations provide a better insight on how frequency shift and damage structure observed at the electrodes of SAW test devices correlate. The main focus of this chapter is to show trends how the damage alters the eigenfrequency rather than to provide an accurate numerical description of frequency shifts in SAW devices. Thus, the resulting eigenfrequency shift will be discussed as relative changes normalized to the eigenfrequency of the undamaged electrode. This enables a comparison of experimental data with the results of the presented FEM calculations even if the initial resonance frequency of the device differs from the initial eigenfrequency of the model.

The eigenfrequency of the FEM model was calculated to be 877 MHz, which is in the same regime as the resonance frequency of roughly 840 MHz from experimental measurements of L-type devices in chapter 3 and 4. The nearly 4 % difference between the model and the experimentally measured frequency of the testing device results from the different dimensions and shape of the FEM model which were used for this study. To reduce mesh complexity, the shape of the electrodes of our FEM model were chosen to be rectangular which was not the case for the electrodes of our test samples, due to used lift-off process. The smaller pitch size of the electrodes used for the FEM model leads to a shorter wave length and thus increases eigenfrequency. Also the limited depth of the substrate, which was used as a simplification to reduce computation time, increases the eigenfrequency because the substrate reacts stiffer when it is thinner and fixed at the bottom plane.

5.4.1 Principal considerations

From our simple calculations, where the Young's modulus and the density of the electrode were varied (Fig. 5.7), we can learn the following:

- The density or mass change of the electrode has a much higher impact on the frequency of SAW devices than the Young's modulus for the considered resonant case. To achieve a relative frequency shift of 0.5 %, the relative Young's modulus

has to be changed for roughly 20 %, while changing the relative mass for 7 % has the same result.

- As expected, the decrease of the Young's modulus leads to a decrease of the eigenfrequency while a decrease of the density changes the eigenfrequency in the opposite direction.

- The relative eigenfrequency shift correlates linearly to small variations of Young's modulus and density of the electrode's material.

In chapter 4 it has been shown that voids as observed in electrodes of SAW devices have a much lower influence on the stiffness compared to the situation of intrinsic tensile stresses in a thin film [65]. It was argued that among other reasons this is related to the fact that cyclic shear stress does not vanish in the presence of a crack. This argument has been confirmed by the FEM simulation of a crack in an electrode (Figs 5.6 and 5.7). Neither component of the cyclic stress state σ_{yz} and σ_{xy} decreases to zero at the crack location. The shear stress σ_{yz} at a certain level parallel to the substrate in the electrode results from the inertia forces of all material above. Thus, a void which separates the electrode perpendicular to the y-axis observed in SAW test devices can only reduce the cyclic load transmission through the crack, but not eliminate it. Decohesion of the film, i.e. a crack at the interface between the electrode and substrate would significantly lower the induced cyclic shear stresses. However, such a situation has not been observed experimentally.

The cyclic stress state induced by a surface wave is rather complex, which results from the fact that, on the one hand, the stress is induced by inertia due to the vibration of the electrode and, on the other hand, by the strain of the substrate, which gets cyclically deformed by the SAW itself. To differentiate the two components from each other, two model calculations were performed (Figs. 5.3 and 5.4). It is not obvious, however, to judge from these results at which location a crack would cause a maximum change in stiffness since the maxima in σ_{xy} and σ_{yz} are found at different locations. Nevertheless, a trend can be seen that a crack starting from the bottom of the electrode causes a more significant change in frequency (Fig. 5.11) than a crack starting from the surface. This may be related to the large stress components near the interface induced by the substrate strain shown in Fig. 5.4b. Further, it can be argued that the stresses induced by the inertia of the electrode itself do not change much by the introduction of a crack because the mass and the amplitude of the deflection of the electrode remain unchanged.

5.4.2 Extrusion length variation

The extrusions behave like vibrating beams fixed at one side. However, the eigenfrequency of the beams themselves depends on their length. These beams are forced to vibrate at the resonance frequency of the whole FEM model. Scaling the length of these beams can lead to the case where they have a similar eigenfrequency as the whole model, which is true for the white areas in Fig. 5.13. The length of the extrusions in the white areas of the plot correlates to the first, second and third mode of the beams. As the amplitude of the vibrating beams is rather high, the resonance frequency of the whole system shifts even if the mass of the whole system is much larger than the mass of the extrusions. This effect is only obtained in an FEM model, because all extrusions virtually have the same length due to symmetry conditions. In a real electrode, the length of the extrusions is statistically distributed as shown in chapter 4. Most extrusions have a length which is lower than the 300 nm, where the first transition of the mode appears. Thus the most extrusions will lead to a decrease of the eigenfrequency as is shown in Fig. 5.13. In any case the extrusions are forced to vibrate at the testing frequency of the device independent of its length. A forced vibration leads to a phase shift of the cyclic amplitude between source and vibrating system [70], if the source frequency is different compared to the resonance frequency of the vibrating system. Assuming that a small region of the electrode/substrate system around each extrusion has a slightly different eigenfrequency, parts of the electrode vibrate with a small phase shift relative to the vibrating amplitude of the test device. Due to the distribution of the extrusion lengths in the test device, each region around an extrusion vibrates with a slightly different phase shift. With increasing extrusion density this leads to a decrease of the vibration amplitude and a broadening of the resonance frequency peak of the SAW test device.

5.4.3 Damage density variation in the FEM model

For small values, the relative eigenfrequency depends linearly on the damage density, as shown in Fig. 5.15. While cracks without volume (open triangles) reduce the eigenfrequency of the FEM model, cracks with a width of 100 nm (full boxes), which are equivalent to voids in test samples, increase the eigenfrequency. The comparison between these two cases is equivalent to the simulation (chapter 5.3.2) where the Young's modulus and the mass of the electrode were varied. The cracks without volume reduce the eigenfrequency due to the stiffness decrease of the finger. In the case of voids, not only stiffness but also the mass of the

finger is reduced with the increase of the damage density. This leads to an increase of the eigenfrequency of the FEM model when the damage density is increased.

However, in the electrodes of SAW test devices extrusions and voids appear at the same time next to another as was shown in chapter 4, and the mass of the electrode needs to be conserved. The realistic combination of voids and extrusions in one model (open circles and triangles in Fig. 5.15) shows a negative slope of the relative eigenfrequency as a function of damage density in the case of the grain like extrusions. Since the volume of voids and extrusions is the same, the main effect on the eigenfrequency is related to the decrease in stiffness of the electrode. Nevertheless, the decrease in the frequency is less significant in the case of high aspect ratio extrusions compared to cracks indicating that the situation is more complex and the eigenfrequency shift can not only be explained by the stiffness decrease due to void density. The redistribution of mass, from voids to extrusions changes the geometry of the resonant system and causes an additional influence on the eigenfrequency.

The eigenfrequency of the model reacts very sensitively to geometrical changes as can also be observed in the case of changing the fixing height of the extrusion at the side of the electrode (Fig. 5.14). The higher the extrusion is fixed the more the extrusion has to move during each cycle as the deflection of the upper parts of the electrodes has a higher amplitude. Thus, the eigenfrequency shift of the FEM model increases with increasing fixing height.

5.4.4 Comparison with experimental data

The comparison between experimental data of SAW test devices from chapter 4 and FEM simulation given in Fig. 5.16 shows that the eigenfrequency shift of the test samples and the FEM model are in the same regime. However, this comparison is not straightforward because defect density and frequency shift are differently defined in the experiment and the simulation.

The frequency shift of the experimental data does not represent the shift of the resonance frequency of an electrode/substrate system like it was simulated in the presented FEM study. In the experiment the shift of the bandpass of a whole frequency filter was measured. The used SAW test devices consist of two resonant devices (Interdigital transducers, IDT) with slightly different resonance frequencies. These resonant devices consist of electrodes on a piezoelectric substrate as was simulated in the FEM model. In the experiment, only one of the two IDTs was loaded at its resonance frequency and, thus, only one of them showed the

characteristic microstructural damage formation. Furthermore, only the lower or the upper flank of the bandpass did shift as result of the damage formation. Therefore, for a comparison of the frequency shift of one of the IDTs with the frequency shift of the FEM model the reported frequency shift of the bandpass needs to be approximately doubled. Instead, the relative frequency shift of the FEM data was reduced by a factor of two (slashed open circles in Fig. 5.16). The range between the original and the reduced data of the FEM model are comparable to the experimental data.

The damage density in the case of the experimental data represents the measured extrusion density, while the damage density in the case of the FEM simulation represents the number of damage sites which consist of a void/extrusion pair. Unfortunately, there are no experimental data available which analyses the correlation between the extrusion and void density quantitatively. However *in situ* observations in chapter 3 showed that an extrusion is often surrounded by several voids, which typically originate at the sidewall of the electrode and extend then towards the middle of the electrode. As these observations were made by the use of top view SEM micrographs only voids reaching the surface were detected, which implies that the number of voids could have been even higher. On the other hand, the experimentally observed voids typically extend only a third or half of the entire width of an electrode and, thus, are not as severe as the geometry of a void in our simulation. From the FEM simulations (Fig. 5.10), we know that two voids extending halfway from the sidewall towards the middle of the electrode decrease the eigenfrequency approximately to the same amount as one void extending through the whole electrode. Thus, we define a typical damage site as one extrusion with two to three voids with a combined length of the electrode width. This is more or less in agreement with the observations described in chapter 3.

Furthermore, parameters like the fixing height (Fig. 5.14) or the void width (Fig. 5.12) have a significant impact on the eigenfrequency of the FE model. Increasing the fixing height for example would lead to a steeper slope of the eigenfrequency versus the defect density in Fig. 5.16, since both types of extrusions in the combined models lead to a negative frequency shift. Decreasing the fixing height of the extrusions in contrast would lead to a smaller slope of the frequency shift progression. Beside the fixing height of the extrusion also the void width has an impact on frequency shift. Compared to experimental findings (chapter 3), the simulated voids of the FE model are wider than in reality, which is in the case of the FE model determined by the element size. A decrease of the void width would also decrease the volume of the extrusions, since the volume has to be constant. Thus a decrease of the void width would lead to a more crack-like behavior, as is plotted in Fig. 5.15 since the shift of the

mass from the void to the extrusions would play a minor role. But not only the electrode geometry has an impact on the resonance frequency of the FE model. The limited substrate thickness, which was chosen to reduce computation time, increases the stiffness of the substrate and decreases the volume ratio between electrode and substrate. Nevertheless the intrusion depth of the surface wave is in the range of the wave length of 4 μm [4] and a further increase in substrate thickness changes the absolute eigenfrequency of the device for less than one percent. Thus for this comparison the influence of the substrate thickness can be neglected.

Considering all these factors, the agreement between experiment and simulation shown in Fig. 5.16 is reasonable. Since in reality all kind of extrusions, e. g. grain-like or high-aspect ratio extrusions, are present on the surface of an SAW device, the comparison for the two types of extrusions in Fig. 5.16 shows the regime were the experimental data can be expected. As was mentioned above, the frequency shift of the FE model has to be divided by two to be comparable to experimental data. Since the main proportion of extruded volume generally is located in grain-like extrusions, the FE results divided by two (semi-solid circles in Fig. 5.16) show a close correlation compared the experimental data.
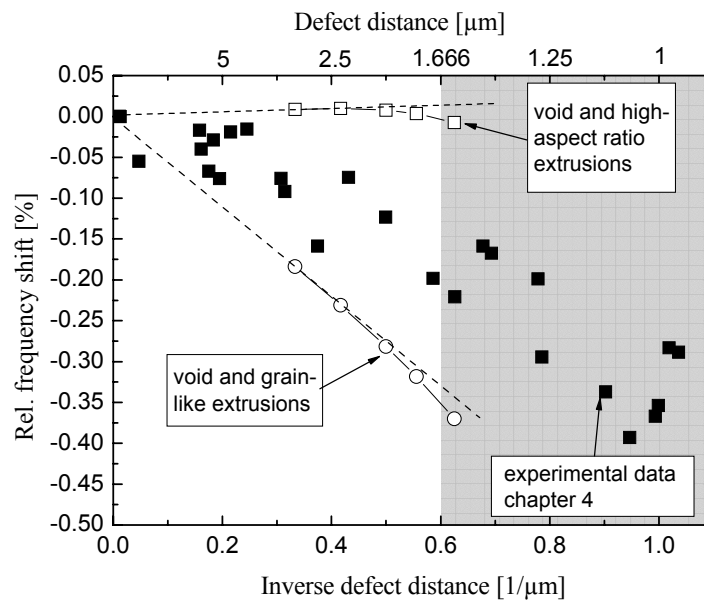
Fig. 5.16:   Comparison between calculated and experimental data. The frequency shift of the test devices from chapter 4 was multiplied by the factor of two, since the measured data results from the middle frequency shift of the band pass. As damage density of the test devices, the measured extrusion density was plotted, while in the case of the FE model the void density was plotted.

In particular the deviation from the linear behavior for damage densities larger than $0.6/\mu m$ (Fig. 5.15), which corresponds to a damage distance of roughly 1.7 µm can be seen in both sets of data. The deviation is due to the fact that neighboring damage start influencing each other when their separating distance becomes too small.

5.5 Conclusions

The present FE analysis of the characteristic damage structure in metal electrodes of SAW devices showed, that the frequency shift resulting from the damage formation in the metallization depends on a complex set of parameters. The differentiation of these parameters in this study provides the general trends:

- Void formation leads to a decrease of the effective stiffness of the electrode material. The reduced stiffness leads to a decrease of the eigenfrequency of the model.

- The shift of the centre of gravity due to void and extrusion formation plays a significant role. Parameters like the fixing height of the extrusions and the site of void formation in the metallization can lead to a significant frequency shift. In principle mass changes would have even a stronger influence on the eigenfrequency. However they do not occur during damage formation since all processes are mass conservative.

- Extrusions behave like vibrating beams and locally can lead to a significant positive or negative phase shift. This leads to a broadening of the resonance frequency in SAW devices.

- The comparison with experimental data shows that the device degradation due to the geometrical changes induced by ultra high-cycle fatigue can be simulated by the presented FEM model.

6 Discussion of possible mechanisms

6.1 Model description

In the previous chapters it was shown that the cyclic stress in the metallization induced by surface waves can have a purely deviatoric character and a cycle time of less than one nanosecond. Therefore we concluded that diffusion mechanisms are not fast enough to interact with the stress induced by the surface wave. But the similarities of characteristic damage structures to electromigration [11, 12] or thermal hillock formation [14] suggest the picture of a diffusion based mass transport at the grain boundaries, driven by a hydrostatic stress gradient between the inside and the outside of the material. Assuming that this general picture is appropriate, the question arises how a cyclic deviatoric stress induces hydrostatic stresses.

As qualitatively discussed in chapter 3 and calculated in chapter 5, it is conceivable that a gradient in the stress amplitude exists within individual grains. For instance, the cyclic shear stress component σ_{yz}, decreases from the substrate/electrode interface to the electrode surface. Therefore, dislocations may move during one half cycle from a location of high cyclic stress to one of low cyclic stress if the glide plane reaches over a range of z-values. Fig. 6.1 a illustrates this configuration for a simplified stress state of an electrode on a perfectly rigid substrate (see chapter 5.3.1). In such a case, the shear stress amplitude depends only on the height z (see Fig. 6.1 a and b). The inclined glide plane reaches from the substrate to a certain height, which is determined by the angle of the glide plane relative to the substrate and the width of the grain. A dislocation vibrates due to the cyclic load by the surface waves and deflects back and forth on the glide plane (Fig. 6.1 c). Since the shear stress that acts on the dislocation depends on the position of the dislocation, different stresses act on the dislocation at the points of maximum deflection. As a result, the amount of deflection of the dislocation up and down is different as schematically indicated in Fig. 6.1 c. For the configuration shown, the deflection is larger in the downwards direction, and the cyclic stress gradient (6.1 b) leads to a stepwise movement towards the interface and the grain boundary. This stepwise movement of the dislocation can be compared to a diffusion process with a frequency term (in

this case the load frequency by the surface wave) and a jump probability, which is mainly determined by the stress gradient the dislocation feels on the glide plane. This stress gradient is governed by the stress amplitude of the surface wave, the stress gradient in the metallization, the angle of the inclined glide plane and the grain size.
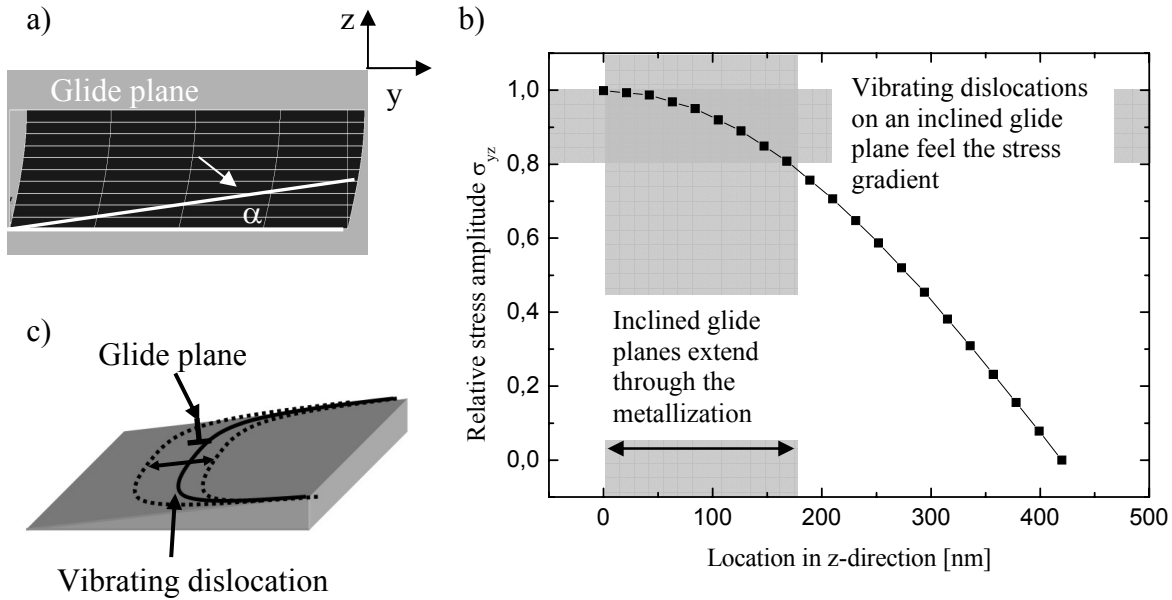
Fig. 6.1   a) The small figure shows a FEM simulation of an 420 nm thin electrode on a perfectly rigid substrate (see chapter 5.3.1) at the maximum deflection. The white line illustrates an inclined glide plane. b) Stress amplitude versus the height of the metallization which was calculated by the FEM model. The grey bars highlight the height which the inclined glide plane extends through and the corresponding range of stress amplitude. c) A dislocation vibrating due to the cyclic load 'feels' different stresses at its maximum deflection points.

Through the process of stepwise dislocation glide more or less parallel to the interface, dislocations passing through the grain boundaries induce compressive and tensile stresses at the grain boundaries GB1 and GB2 (Fig. 6.2), respectively. As an example we can calculate the stress σ_n normal to GB1 and GB2 caused by one dislocation passing through the grain. For a 400 nm thin metallization the stress σ_n which is normal to GB1 and GB2 is given by:

$$\sigma_n = \underbrace{\frac{b \cdot n_{\text{dislocations}}}{d_{\text{grain}}}}_{\textit{plastic strain}} \cdot E = \frac{2 \cdot 10^{-10}\,\text{m} \cdot 1}{4 \cdot 10^{-7}\,\text{m}} \cdot 70\,\text{GPa} = 35\,\text{MPa} \qquad (6.1)$$

where d_{grain} is assumed to be equal to the film thickness, b is the Burgers vector with a length of $2 \cdot 10^{-10}$ m and n is the number of dislocations.

Therefore a single dislocation passing through a grain induces 35 MPa of compressive stress at GB1 and 35 MPa tensile stress in GB2. The resulting stress gradient in the grain between these two grain boundaries inhibits further dislocation nucleation and glide from the same dislocation source.
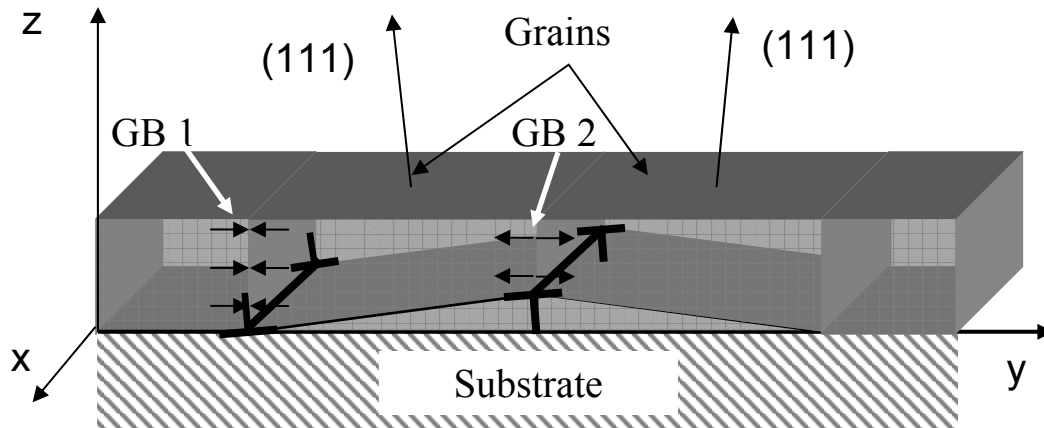
Fig. 6.2:   The schematics shows the miss orientation of the (111)-planes in the grains in SAW electrodes. For a better imagination, the illustration of the miss orientation is slightly exaggerated. Dislocations emitted from grain boundaries are stimulated to vibrate with the external cyclic shear stress. The cyclic stress gradient leads to a stepwise movement of the dislocation in direction to GB1. The dislocation movement induces compressive stresses at GB1 and tensile stresses at GB2.

Further, it is argued that the compressive and tensile stresses induced by the cyclic shear stress of the acoustic wave at the grain boundaries GB1 and GB2 leads to stress induced diffusional fluxes (Fig. 6.3). Thus there are two possible diffusion mechanisms that may occur:

- Diffusion of atoms around the grain (see Fig. 6.3) lead to dislocation climb at the GB1 and GB2, as atoms diffuse from GB1 to GB2 and vacancies in the opposite direction. As a result, the dislocation would eventually vanish, and the electrode would remain undamaged.

- The second feasible path for atoms to relax the compressive stress at GB1 is through the surface of the electrode in form of an extrusion. The stress gradient for this path is much higher than the one for the back flux around the grain. In the same manner, vacancies that reach the surface at GB2 reduce tensile stresses and lead to grooving and void formation.
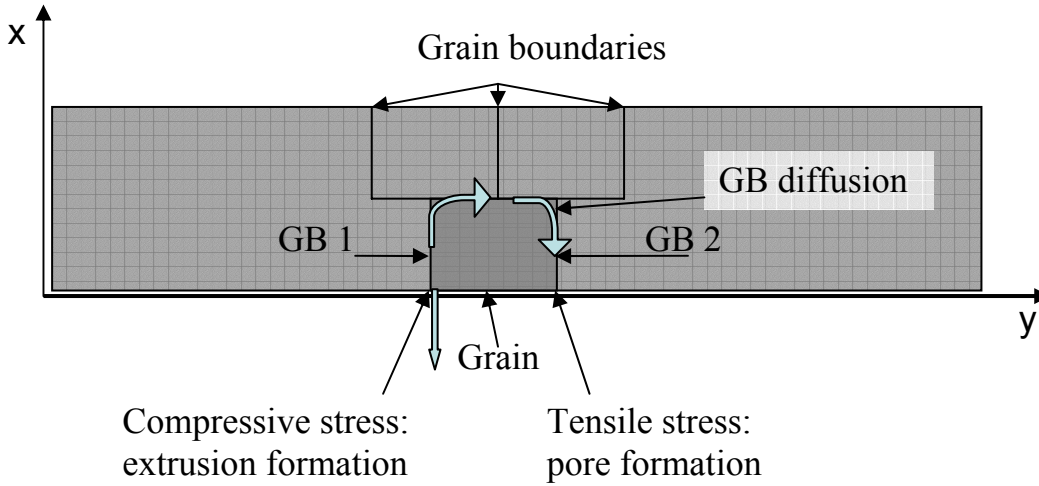
Fig. 6.3:   Schematics shows a characteristic microstructural configuration from bottom view. The tensile and compressive stresses lead to extrusion and void formation and/or back flux through the grain boundaries.

For the normal stress σ_n at GB1 we take the calculated value for one dislocation, assuming that from the used power of 158 mW a maximum stress amplitude σ_{yz} of 50 MPa results in the electrodes [7]. Assuming that the grain boundary where the extrusion grows out of, is a source for vacancies, the dislocation annihilation process is controlled by the dislocation climb velocity, which can be estimated to be [71]:

$$v_{\text{climb}} = \frac{D_{gb} \cdot b^3 \cdot \sigma_n}{k \cdot T \cdot b} \approx 3.7 \cdot 10^{-7} \, \frac{m}{s} = 370 \, \frac{nm}{s} \qquad (6.2)$$

For a numerical analysis we assumed a Burgers vector of $b = 2 \cdot 10^{-10}$ m, a normal stress of $\sigma_n = 35$ MPa, a preexponential factor for grain boundary diffusion of $D_{gb}{}^0 = 2 \cdot 10^{-6}$ m^2/s, an activation energy for the grain boundary diffusion $Q_{gb} = 0.62$ eV [52] and a temperature $T = 341$ K. As volume diffusion is rather slow at room temperature, we can neglect this diffusion path (preexponential factor $D_{Vol}{}^0 = 1.7 \cdot 10^{-4}$ m^2/s, activation energy of volume diffusion $Q_{Vol} = 1.47$ eV [72]). Assuming, that the dislocation has a width of a burgers vector b an a length of the grainsize d_{grain}, the volume rate by the climbing process is 30000 nm^3/s.

This result can be compared to the experimental findings for the extrusion growth in chapter 3. The extrusion (arrow G) in the Fig. 3.5 has roughly a width and height of 150 nm and a length of about 800 nm, which is a volume of $V_{extr.} = 1.8 \cdot 10^7$ nm^3. Therefore the dislocation climb process would need 600 s to deliver the extrusion volume. In the *in-situ*

experiment, the growth of the extrusion took roughly the same amount of time which shows that even though this is a rough estimate, the model provides results in the right regime.

In Fig. 6.4, the model is schematically illustrated, where the sinks and sources for atoms or vacancies at GB1, GB2 and the extrusions are represented by containers with a certain number of atoms. The atom flux between these containers is determined by the active mechanism. As was described above, different mechanisms are active between GB1 and GB2 two, namely the stepwise dislocation movement, induced by the cyclic mechanical stress gradient and the material back flux based on grain boundary diffusion induced by the tensile and compressive stresses at GB1 and GB2. The third path of an atom flux from GB1 is the diffusion to the surface of the electrode where extrusions can grow. Other grain boundaries which can also act as atom sinks like they are shown in Fig. 6.3 are neglected.
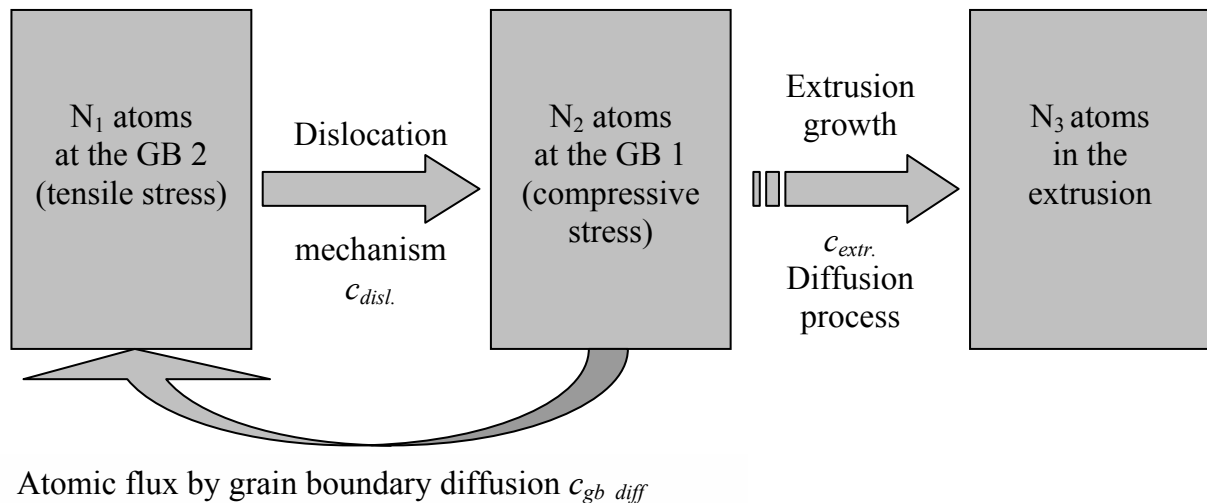
Fig. 6.4: Abstraction of sources and sinks (GB1, GB2 and extrusions from Fig. 6.3) are illustrated as containers, while the possible mass transport paths are expressed as arrows.

6.2 Microstructure and reliability

In the chapters 3 to 5, it has been shown that the reliability of SAW test devices is determined by the void and extrusion formation in the metallization due to the cyclic mechanical shear stress. The formation of this damage can be explained by the presented model. The gradient of the cyclic shear stress amplitude leads to the formation of tensile and compressive stresses at the grain boundaries, which induces a stress driven material flux at the grain boundaries. Compressive stresses lead to the formation of extrusions, while at sites of tensile stresses void formation results from the accumulation of vacancies. Based on the presented model, it will be discussed how grain size, grain orientation and the grain boundary diffusion coefficient influence the reliability of SAW devices.

6.2.1 Grain size

The grain size determines the flow stress of the metallization [27], the height over which an inclined glide plane extends in the metallization and the diffusion distance. In the case of a reduction of grain size, the pinning point distance decreases, which increases the stress needed for the deflection of the dislocation segment in y-direction (Fig. 6.1 c). For the same cyclic stress amplitude the dislocation motion is reduced in smaller grains. Also, the total stress difference, the dislocation feels on an inclined glide plane (Fig. 6.1 b), gets smaller as the height, the glide plane extends through, is reduced. Thus the compressive and tensile stresses which build up at the grain boundary GB1 and GB2 are reduced. Due to the shorter diffusion distance, the back flux as well as atomic flux to the extrusion is enhanced.

If Al is used as electrode material, an oxide layer is present at the surface. This means, that analogue to the Blech experiments for electromigration [48] a critical stress has to be built up to crack the natural oxide. Since the stress at the grain boundary depends on the grain size, only the part of the grains in the metallization which are big enough can participate in the extrusion and void formation process which are highlighted by the grey area in Fig. 6.6 a. A shift of the mean grain size to smaller values, decreases the number of grains contributing to the damage formation.

Therefore, the reduction of the grain size has a positive influence on reliability in two ways: on the one hand, a higher stress amplitude is needed to move the dislocations through the grain and on the other hand, the backflux is increased, since the length of the diffusion path is decreased.

6.2.2 Texture

As was described in the previous part of this chapter, the grain orientation determines the incline angle of the glide plane and the orientation of the burgers vector relative to the induced cyclic shear stress, as well as the diffusivity at the grain boundary [73]. A better texture reduces the number of grains with glide planes of high incline angles as can be seen in Fig. 6.5 b. Therefore, the glide plane reaches through a smaller height in the grain, which leads to a decrease of the stress difference between starting and end point of the glide plane and to a decrease of the induced stress at the grain boundaries GB1 and GB2. From the reduced stress at the grain boundary results a lower extrusion growth rate. Aside from the dislocation mechanisms, a better grain orientation leads also to a lower grain boundary misfit, which decreases the grain boundary diffusivity [73] and thus decreases also the extrusion growth rate.

An improvement of the texture has a similar effect on the dislocation mechanism as a decrease in grain size as in both cases, the stress difference on the active glide plane is decreased. The assumption, that a critical stress is needed to start the growth process of an extrusion at the grain boundary, leads to the case that with a decrease of the standard deviation of the grain orientation distribution as is shown in Fig. 6.5 b, the number of grains which can contribute to the damage formation (gray area in Fig. 6.5 b) is reduced. Therefore, a perfect (111) texture would completely inhibit damage formation in an Al metallization.

Thus, a sharper texture leads to an overall increase in reliability as in the case of Al a higher stress amplitude is needed to build up a critical stress at the grain boundary to nucleate extrusions. This conclusion from our model is in agreement with literature [22], where it was shown, that the use of epitaxially grown Al films in SAW devices leads to a 100 times higher lifetime compared to polycrystalline films.
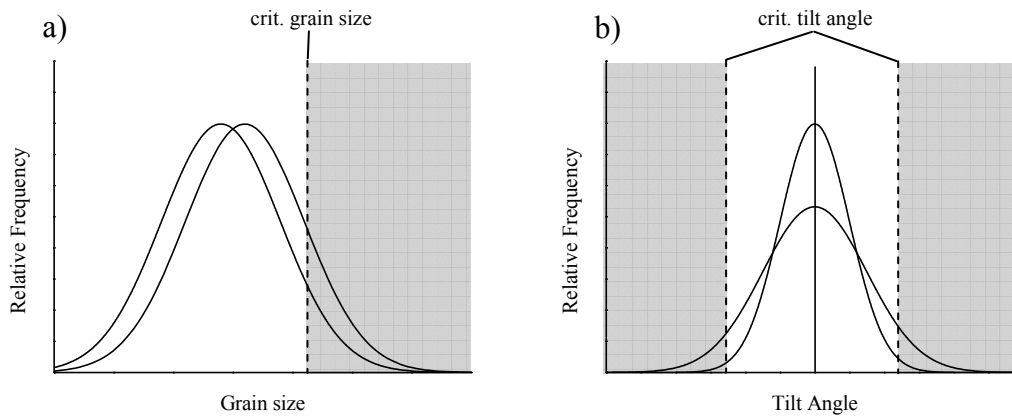
Fig. 6.5:   a) A smaller mean grain sizes leads to a shift of the grain size distribution function, which reduces the number of grains bigger than the critical grain size which is highlighted by a grey background. b) Sharper textures have a smaller standard deviation of the grain orientation distribution function, which reduces the number of grains which have a high tilt angle. The grey area in the plot highlights the area where the angles of the grains are higher than a critical value.

6.2.3 Grain boundary diffusivity

Since our model proposes, that grain boundary diffusion is the bottleneck of the damage formation in SAW devices, the diffusivity at the grain boundaries plays a major role concerning the reliability of SAW devices. The grain boundary diffusivity in pure materials can only be reduced by a reduction of the misfit of the grain boundaries, which is, from a technological point of view, hard to achieve [21, 22]. The easier way to reduce material transport at grain boundaries, is the use of alloying elements. Alloying elements are extensively used in high-power SAW devices for mobile applications to increase reliability (e.g. Cu [18], Ti [19] or W [20]). At least from Cu it is well known from electromigration experiments, that alloying it to Al reduces the grain boundary diffusivity [47]. As it was pointed out in chapter 2.7, the comparison of experiments with SAW devices and electromigration revealed similar impacts of the alloying of Cu to Al-based metallizations on the measured activation energies and lifetime, which is also consistent with our model.

7   Summary

Surface Acoustic Wave (SAW) test devices were used to study fatigue in pure Al thin films at ultra high frequencies in the GHz regime. In SAW devices a standing acoustic wave on the surface of the piezoelectric substrate induces a cyclic mechanical stress in the metallization, which leads to a characteristic damage structure accompanied by significant device degradation. By the use of these devices for fatigue experiments cycle numbers of up to 10^{15} cycles can be reached in a reasonable time.

For the experiments at ultra high frequencies, two different designs of SAW test devices were used: a 2-port design was used to study the fatigue behavior of continuous Al thin films and a Ladder-type design was used to study fatigue in small scale Al electrodes with a width of roughly 1 μm. In both cases, the resonance frequency of the test devices was approximately 900 MHz. The device performance degradation was monitored during the test by the measurement of the resonance frequency shift of the test devices. The 420 nm thick films were vapor deposited onto a piezoelectric single-crystalline 42° rotated Y-cut $LiTaO_3$ substrate and patterned by a lift-off process. The microstructure was stabilized by an annealing step in air at 540 K. The resulting microstructure had a preferred (111) out-of-plane orientation and the mean grain size was slightly smaller than the film thickness.

The cyclic mechanical stress induced by the surface waves leads to void formation at the grain boundaries accompanied by material extrusions out of the surface of the Al metallization on a short time scale of some hundred seconds. Extrusions were observed to appear as two different types: *high aspect ratio extrusions* with a height equal to their width and significant higher lengths grow out of the grain boundaries while *grain like extrusions* result from grains growing out of the surface of the metallization. The void and extrusion formation preferably takes place at sites of high cyclic stresses, which are strongly localized due to the short wavelength (roughly 4μm) of the surface wave.

By the use of Focused Ion Beam (FIB), Scanning Electron (SEM) and Atomic Force microscopy (AFM), the extrusion density at the surface of the continuous and patterned Al thin film could be analyzed quantitatively. The microstructural analyses revealed significant grain growth during fatigue testing. This grain growth showed a strong correlation to the

frequency shift of the device. Aside from the grain size, the observed extrusion density at the surface of the metallization increases linearly with the shift of the measured resonance frequency of the SAW test devices. This correlation was found to result from the void formation which reduces the effective stiffness of the metallization. For the Ladder-type devices with the patterned Al thin film an analytical model of Xia and Hutchinson [65] could be applied which describes stress relaxation by parallel cracks in thin films. For small crack densities the model predicts a linear connection between damage density and stiffness of a metallization.

Although the linear connection between damage density and the resonance frequency of the device was explained, the comparison with experimental data shows significant differences due to the complex geometry and stress state in SAW test devices. Therefore a detailed Finite Element (FEM) study was performed to gain a deeper understanding how the observed voids and extrusions influence the eigenfrequency of the electrode/substrate system which is equivalent to the resonance frequency of the SAW test device. This study showed that aside from the stiffness decrease the shift of the mass from the voids in the inside of the electrodes to the extrusions at the side of the electrodes has an additional influence on the resonance frequency of the device.

At stress amplitudes as low as 14 MPa the Al thin films reached up to 10^{14} cycles to failure and did not show a fatigue limit, which was expected since fcc-metals do not show a fatigue limit.

Aside from the shift of the resonance frequency, the degradation of the metallization can also lead to short circuits, since extrusions can bridge the gap between neighboring electrodes in the SAW test devices. Therefore, the distribution of the extrusion lengths was analyzed, which revealed that the probability of a short circuit depends exponentially on the width of the gap between the electrodes, as well as on the extrusion density which is equivalent to the frequency shift.

Based on the experimental observations and FEM simulations, a qualitative model was developed which explains the observed damage structure of voids and extrusions at the grain boundary. It is assumed that the dislocations vibrate at the resonance frequency of the SAW device. Due to the gradient of the stress amplitude, dislocations on glide planes at an inclined angle relative to the substrate have different deflection amplitudes in back and forth direction, which leads to a stepwise shift. Thus, neighboring grains "drift" into or out of each other. This induces a normal compressive or tensile stresses at the grain boundary leading to the formation of voids or extrusions.

8   Appendix

8.1 *In situ* experiments (L-type test devices)

| Time [s] | Frequency shift [MHz] | Half height extrusions | | Grain like extrusions | | Total | Estimated Extr. Vol. [%] |
		mean extr. length [nm]	mean Extr. Width [nm]	mean extr. length [nm]	mean Extr. Width [nm]	Num. extr.	equiv. to porosity
0	0	71	271	69	134	268	0.33
5	-0.06	0	0	0	0	0	0.00
15	0.09	79	84	9	171	3	0.01
35	0.08	83	84	9	177	5	0.01
75	0.09	85	487	89	178	26	0.06
105	0.10	101	391	84	168	43	0.09
135	0.08	103	382	88	165	63	0.13
165	0.04	104	401	90	181	82	0.20
195	0.12	104	401	90	181	82	0.20
225	0.10	104	382	91	177	108	0.25
255	0.09	105	375	93	175	127	0.30
285	0.14	106	368	95	172	137	0.32
345	0.20	105	374	97	171	144	0.35
405	0.22	106	379	97	171	145	0.35

Table 8.1:   Experimental parameters were P_{mean} = 22dBm (equal to 158 mW), T = 301 K (Fig. 3.7 and 3.8). Half height and grain like extrusions were measured from SEM images. Estimated extrusion volume was calculated from the measured area of each extrusion times its height (half height or full height of the metallization).

| Time [s] | Frequency shift [MHz] | Half height extrusions | | Grain like extrusions | | Total | Estimated Extr. Vol. [%] |
		mean extr. length [nm]	mean Extr. Width [nm]	mean extr. length [nm]	mean Extr. Width [nm]	Num. extr.	equiv. to porosity
0	0.00	135	316	86	251	186	0.29
3	0.13	136	243	82	88	16	0.03
21	0.09	139	308	83	248	54	0.10
57	0.12	135	274	84	283	94	0.21
93	0.15	137	292	95	302	107	0.26
141	0.21	139	309	100	311	129	0.32
189	0.22	137	334	103	339	175	0.47
285	0.30	138	341	104	339	223	0.60
429	0.34	139	353	105	347	262	0.75
621	0.40	141	362	105	347	299	0.90
1005	0.47	143	374	106	355	323	1.04
1581	0.59	144	376	106	355	330	1.11
2349	0.65	145	382	106	355	338	1.17

Table 8.2:   Experimental parameters was P_{mean} = 22 dBm (equal to 158 mW), T = 321 K (Fig. 3.7 and 3.8). Half height and grain like extrusions were measured from SEM images. Estimated extrusion volume was calculated from the measured area of each extrusion times its height (half height or full height of the metallization).

| Time [s] | Frequency shift [MHz] | Half height extrusions | | Grain like extrusions | | Total | Estimated Extr. Vol. [%] |
		mean extr. length [nm]	mean Extr. Width [nm]	mean extr. length [nm]	mean Extr. Width [nm]	Num. extr.	equiv. to porosity
0	0.00	108	245	126	131	55	0.14
3	0.09	86	139	106	112	14	0.02
6	0.05	87	168	106	112	20	0.03
9	0.05	84	193	107	118	27	0.04
12	0.05	84	193	107	118	28	0.05
15	0.07	84	193	116	117	28	0.05
18	0.03	84	193	116	117	28	0.05
24	0.07	84	189	116	117	32	0.05
30	0.08	89	207	121	117	37	0.08
36	0.07	88	207	121	117	38	0.08
42	0.11	90	211	121	114	39	0.08
48	0.12	90	216	117	114	43	0.09
60	0.11	102	228	116	152	53	0.12
84	0.13	90	254	116	151	73	0.18
108	0.13	89	264	123	148	78	0.20
132	0.14	93	272	115	140	85	0.22
156	0.16	94	273	115	145	90	0.25
204	0.19	93	286	114	148	104	0.29
252	0.21	96	285	119	147	122	0.36
300	0.26	105	298	119	148	142	0.47
396	0.36	106	307	125	146	181	0.64
492	0.38	111	310	117	148	203	0.76
588	0.45	115	311	131	145	228	0.87
780	0.47	118	310	127	146	239	0.96
972	0.52	123	318	119	145	251	1.05
1164	0.53	127	344	119	147	328	1.49
1548	0.57	131	345	125	139	387	1.79
2316	0.72	131	347	124	139	391	1.83
3084	0.82	131	348	123	138	392	1.82

Table 8.3: Experimental parameters was P_{mean} = 22dBm (equal to 158 mW), T = 341 K (Fig. 3.7 and 3.8). Half height and grain like extrusions were measured from SEM images. Estimated extrusion volume was calculated from the measured area of each extrusion times its height (half height or full height of the metallization).

8.2 Frequency shift versus damage density in continuous Al films (2-port test devices)

Chip	Temp. [K]	Time [h]	Cycle num.	Power [mW]	Freq. Shift [MHz]	Extr. Dens. [1/μm]
E85-W2 16	358	1	3.24E+12	1	-1.86	0.27
E85-W2 45	303	1	3.24E+12	1.7	-0.15	0.09
E85-W2 46	358	1	3.24E+12	2.8	-4.11	0.46
E85-W2 75	303	1	3.24E+12	3	-0.54	0.15
E85-W2 76	358	2	6.48E+12	1.2	-3	0.23
E85-W2 106	358	2	6.48E+12	2.7	-5.31	0.42
E85-W2 165	303	2	6.48E+12	1.6	-0.33	0.07
E85-W2 166	358	4	1.30E+13	1.3	-3.75	0.31
E85-W2 195	303	2	6.48E+12	2.9	-0.81	0.15
E85-W2 196	358	4	1.30E+13	2.5	-9.09	0.48
E85-W2 225	303	4	1.30E+13	1.6	-0.6	0.13
E85-W2 226	358	8	2.59E+13	1.2	-4.26	0.27

Table 8.4:   Experimental parameters and resulting frequency shift (Fig. 4.4). Extrusion density was measured by AFM.

8.3 Fatigue life time of continuous Al films at 900 MHz (2-port test devices)

Chip	Temp. [K]	Time [h]	Cycle num.	P_{mean} [mW]	Freq. Shift [MHz]
E85-W2 45	303	1	3.24E+12	1.5490	-0.1500
E85-W2 165	303	2	6.48E+12	1.5740	-0.3300
E85-W2 225	303	4	1.296E+13	1.6280	-0.6000
E85-W2 315	303	8	2.592E+13	1.5260	-1.0200
E85-W2 375	303	16	5.184E+13	1.8150	-1.7400
E85-W2 465	303	32	1.0368E+14	1.6930	-2.6400

Table 8.5:   Frequency shift versus cycle number at P_{mean} = 1.6 mW in continuous Al films.

Chip	Temp. [K]	Time [h]	Cycle num.	Pmean [mW]	Freq. Shift [MHz]
E85-W2 75	303	1	3.24E+12	2.8930	-0.5400
E85-W2 195	303	2	6.48E+12	3.0110	-0.8100
E85-W2 255	303	4	1.296E+13	2.9660	-1.5300
E85-W2 345	303	8	2.592E+13	3.1450	-2.4000
E85-W2 405	303	16	5.184E+13	3.3240	-3.5400
E85-W2 495	303	32	1.0368E+14	2.2910	-4.2900

Table 8.6:   Frequency shift versus cycle number at P_{mean} = 3.3 mW in continuous Al films.
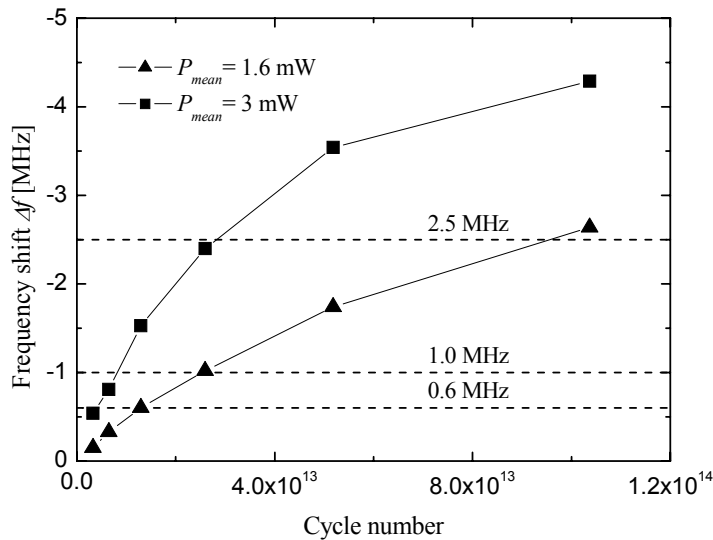
Fig. 8.1:   Frequency shift versus cycle number of continuous Al films. Horizontal dashed lines mark the fatigue limits (0.6, 1.0 and 2.5 MHz frequency shift). From the plot the fatigue life times were estimated (Tab. 4.1).

8.4 Grain size analysis of fatigued Al films (L-type test devices)

Chip	Frequency shift [MHz]	Temperatur [K]	P_{mean} [mW]	t [h]	Cycle num.	num. Grains	av. area per grain [μm^2]	av. grain size [μm]
E85-W2 589	-0.7	303	44.36	8	2.4E+13	220	0.20	0.50
E85-W2 737	-0.4	303	42.62	2	6.1E+12	250	0.17	0.47
E85-W2 740	-0.8	303	43.95	16	4.9E+13	216	0.20	0.50
E85-W2 588	0.0	303	9.52	8	2.4E+13	435	0.10	0.36
Chip								
E85-W3 124	-0.2	333	11.83	2	6.1E+12	358	0.12	0.40
E85-W3 274	-0.5	333	30.96	2	6.1E+12	247	0.18	0.48
E85-W3 139	-1.2	333	31.49	16	4.9E+13	193	0.23	0.54
E85-W3 137	-1.7	333	49.57	8	2.4E+13	178	0.25	0.56
Chip								
undamaged	-	-	-	-		644	0.08	0.32
E85-W2 438	-0.7	358	30.56	2	6.1E+12	194	0.22	0.53
E85-W2 439	-1.4	358	39.41	2	6.1E+12	165	0.26	0.58
E85-W2 440	-1.7	358	58.26	2	6.1E+12	166	0.26	0.57
E85-W3 440	-2.6	358	55.51	16	4.9E+13	175	0.25	0.57

Table 8.7:   Grain size analysis of Al electrodes in L-type devices (Fig. 4.8).
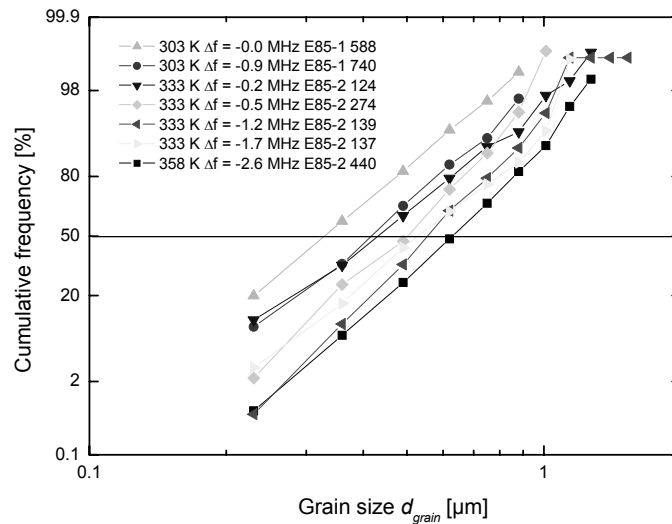
Fig. 8.2:   Grain size distribution of damaged patterned Al films (Tab. 4.1).

8.5 *Ex situ* experiments with patterned Al films (L-type test devices)

electrode num.	Extr. Density [1/µm]	Mean extr. Length
1	0.06	150.4
2	0.00	0
3	0.00	0
4	0.06	136.7
5	0.17	136.7
6	0.06	109.4
7	0.06	205.1
8	0.23	147
9	0.46	155.5
10	0.29	207.8
11	0.58	162.7
12	0.64	146.7
13	0.41	142.6
14	0.81	167
15	1.16	153.8
16	0.93	170
17	1.10	158.9
18	1.22	162
19	0.58	154.6
20	1.22	158.5
21	0.81	168.3
22	1.22	119.2
23	1.04	142.4
24	2.03	165.6
25	1.62	157.2
26	1.62	185
27	1.39	185.1
28	1.39	195.4
29	1.22	175.1
30	1.68	170.2
31	1.62	174.8
32	1.10	154
33	1.28	188.3
34	1.22	194
35	1.33	233.6
36	1.57	180.8
37	0.93	169.2
38	1.45	160.2
39	2.09	189.1
40	1.57	180.8
41	1.86	205.5
42	2.20	169.8
43	1.86	158.5
44	2.03	180.8
45	2.26	155.3
46	1.62	159.7
47	1.74	196.8
48	1.68	198.9
49	1.51	245
50	1.97	182.5
51	2.09	173.9
52	1.39	202.2
53	1.04	199.7
55	1.33	143.8
56	1.51	170.9
57	1.91	166.5
58	1.04	165.6
59	1.10	169.1
60	2.03	206.2
61	1.45	165.1
62	1.68	169.2
63	1.28	198.2
64	1.04	202.8
65	1.86	152.5
66	1.80	176.4
67	1.39	225
68	1.39	175.4
69	1.16	220.8
70	1.28	178.4
71	1.68	164.5
72	2.20	191
73	1.68	212.6
74	1.04	198.2
75	1.62	188
76	1.04	150.4
77	1.68	158.9
78	1.51	197.2
79	1.39	197.6
80	2.38	173.4
81	1.80	177.3
82	1.68	158.4
83	1.28	134.8
84	2.38	158.6
85	1.28	161
86	1.33	173
87	1.16	155.8
88	1.10	163.3
89	1.22	192.7
90	1.62	157.7
91	0.87	174.1
92	1.10	127.4
93	1.51	141.4
94	0.87	168.6
95	0.70	134.4
96	0.35	173.2
97	0.75	138.8
98	0.70	160
99	0.00	0
100	0.00	0
101	0.35	200
102	0.17	184.9
103	0.00	0
104	0.00	0
105	0.06	170.9
106	0.00	0
107	0.00	0
108	0.00	0

Table 8.8:   Extrusion density and mean length versus electrode number in x-direction of Cu containing Al electrodes in an L-type device (Fig. 4.9).

Table 8.9 - 8.12: Experimental parameters and measurement data, 420 nm Al on LiTaO$_3$

Chip	Temp. [K]	Time [h]	cycle num.	Pmean [mW]	Pstart [mW]	Frequenzshift [MHz]
136	358	2	6.1E+12	1.41	1.4	0.0
137	358	8	2.4E+13	2.92	2.8	0.1
274	303	1	3.1E+12	3.26	3.1	0.0
275	303	8	2.4E+13	1.28	1.2	0.1
286	358	2	6.1E+12	3.22	3.3	0.0
424	303	2	6.1E+12	1.34	1.3	-0.1
425	303	8	2.4E+13	3.08	3.0	-0.1
290	358	2	6.1E+12	49.77	47.0	-1.5
438	358	2	6.1E+12	30.56	31.0	-0.7
439	358	2	6.1E+12	39.41	38.0	-1.4
440	358	2	6.1E+12	58.26	57.0	-1.7
587	358	2	6.1E+12	20.71	20.0	-0.3
740	303	16	4.9E+13	43.95	41.0	-0.8
739	303	16	4.9E+13	10.71	11.0	-0.2
738	303	8	2.4E+13	26.68	27.0	-0.3
737	303	2	6.1E+12	42.62	40.0	-0.4
722	303	2	6.1E+12	25.45	25.0	-0.1
590	303	16	4.9E+13	27.24	26.0	-0.7
589	303	8	2.4E+13	44.36	42.0	-0.8
588	303	8	2.4E+13	9.52	8.0	0.0

Table 8.9:   Wafer number E85-W2: Experimental parameters and frequency shift (Fig. 4.10, 4.11).

Chip	num. Extr.	av. Extr.l. [nm]	cum. Extr.l. [nm]	av. Extr.w. [nm]	cum. Extr.w. [nm]	num. grain Extr.
136	440	521	131228	252	162600	311
137	589	321	68343	218	81391	260
274	590	178	44737	247	56863	317
275	722	60	10033	151	11309	192
286	737	156	31285	195	30451	196
424	738	119	23786	209	29599	249
425	739	30	9354	269	6849	163
290	702	238	166271	284	198901	276
438	476	234	109160	291	137144	206
439	634	219	137947	295	186420	284
440	665	252	131228	311	162600	224
587	303	222	66810	315	93445	143
740	547	238	81411	245	84431	
739	113	269	9354	163	6849	7
738	216	209	23786	249	29599	48
737	221	195	31285	196	30451	45
722	111	151	10033	192	11309	24
590	263	247	44737	317	56863	82
589	412	218	68343	260	81391	135
588	9	241	2277	193	1556	1

Table 8.10:   Wafer number E85-W2: Microstructural analysis (Fig. 4.10, 4.11).

Chip	Temp. [K]	Time [h]	cycle num.	Pmean [mW]	Pstart [mW]	Frequenzshift [MHz]
124	333	2	6.1E+12	11.8300	12.0000	-0.2
125	333	2	6.1E+12	49.1100	50.0000	-0.9
136	333	8	2.4E+13	41.8200	42.0000	0.0
137	333	8	2.4E+13	49.5700	48.0000	-1.7
138	333	16	4.9E+13	12.6300	12.0000	0.1
139	333	16	4.9E+13	31.4900	31.0000	-1.2
140	333	16	4.9E+13	50.9700	49.0000	-1.8
274	333	2	6.1E+12	30.9600	30.0000	-0.5
275	333	8	2.4E+13	11.9100	12.0000	-0.3
438	358	8	2.4E+13	33.8900	34.0000	-1.3
439	358	16	4.9E+13	12.9600	13.0000	-0.1
440	358	16	4.9E+13	55.5100	53.0000	-2.6
574	358	2	6.1E+12	12.9300	13.0000	-0.1
575	358	2	6.1E+12	33.9700	35.0000	-0.7
586	358	2	6.1E+12	52.9900	53.0000	-1.2
587	358	8	2.4E+13	13.2200	13.0000	0.3
589	358	16	4.9E+13	35.9300	36.0000	-1.6

Table 8.11: Wafer number E85-W3: Experimental parameters and frequency shift (Fig. 4.10, 4.11).

Chip	num. Extr.	av. Extr.l. [nm]	cum. Extr.l. [nm]	av. Extr.w. [nm]	cum. Extr.w. [nm]	num. grain Extr.
124	33	225	7039	219	6736	11
125	440	185	80928	271	118648	225
136	8	112	1006	135	1082	1
137	885	187	165489	271	238858	422
138	129	174	21487	288	37101	72
139	728	196	142121	291	212249	349
140	907	202	182793	283	255759	405
274	351	187	65340	225	78548	123
275	123	195	23527	246	31700	46
438	552	243	134055	362	198977	285
439	172	240	41498	409	71548	105
440	895	232	207394	326	291478	404
574	151	175	26359	232	35712	52
575	487	203	97510	281	134464	209
586	716	195	139103	267	191356	303
587	137	211	29665	325	45273	72
589	698	221	152972	286	199336	309

Table 8.12: Wafer number E85-W3: Microstructural analysis (Fig. 4.10, 4.11).
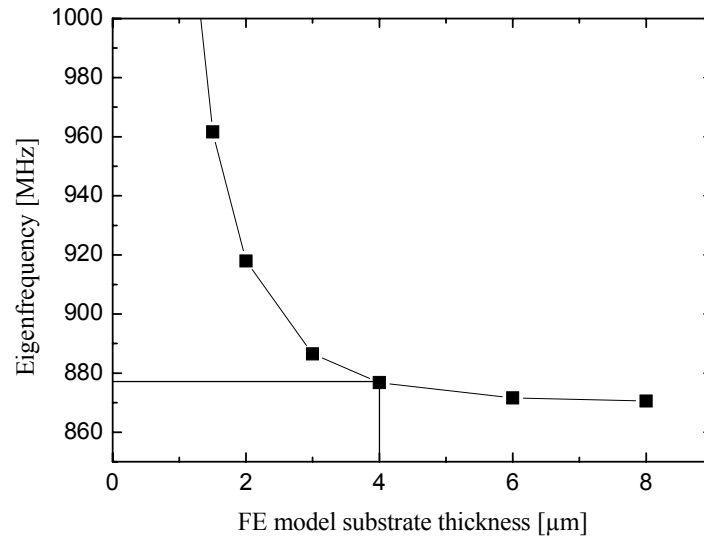
8.6 FEM calculations

Fig. 8.3:   Eigenfrequency of the FE model versus substrate thickness. The line marks the used substrate thickness of 4 µm. Doubling the substrate thickness to 8 µm decreases the eigenfrequency for less than one percent.

9 References

[1] T. H. Courtney: "Mechanical behaviour of materials". McGraw-Hill, New York, USA, ISBN 0-07-116171-6, pp. 566-629 (2000).

[2] S. Suresh, "Fatigue of materials", Cambridge University Press, Sec. Ed., ISBN 521-57847-7 (2001).

[3] Gartner in: http://www.heise.de/newsticker/meldung/45396 (27.7.2004).

[4] J. I. Latham, W. R.Shreve, N. J. Tolar, P. B. Ghate, "Improved metallization for Surface Acoustic Wave devices", Thin Solid Films, **64,** pp. 9-15 (1979).

[5] R., M., White, F., W., Voltmer, "Direct piezoelectric coupling to surface elastic waves", Appl. Phys. Let. **7**, pp. 314-316 (1965)

[6] F. Kubat, W.Ruile, L. Reindl, "P-matrix based calculations of the potential and kinetic power in resonating SAW-structures" IEEE: Ultras. Symp. Proc., Munich, Germany, 329-332 (2002)

[7] F. Kubat, W. Ruile, U. Rösler, C. C. Ruppel, L. M. Reindl, "Calculation of the SAW-induced stress distributions in an electrode of a SAW-device on LiTaO$_3$" to be published in: IEEE: Ultras. Symp. Proc. (2004)

[8] F. Kubat, W. Ruile, T. Hesjedal, J.Stotz, U.Rösler, L.Reindl, "Distribution of the dynamic strain and stress components within a layered film of a SAW resonator on LiTaO$_3$" IEEE: Ultras. Symp. Proc., Hawaii, USA, pp. 1149-1152 (2003)

[9] G. Raml, W. Ruile, A. Springer, R. Weigel, "Characterization of acoustomigration with on-wafer measurement system" IEEE: Ultras. Symp. Proc., Atlanta, GA, USA, pp. 153-156 (2001)

[10] N. Shibagaki, K. Asai, T. Tabuchi, T. Hirashima, M. Hikita, "Acoustically-Induced Migration of Thin Film Electrodes in SAW-Resonator-Coupled Filters", IEEE: Ultras. Symp. Proc. 1, New York, NY, USA, pp. 439-443 (1991)

[11] I., A. Blech, E., S. Meieran, "Electromigration in Thin Al Films" J. Appl. Phys., **40** (2), pp. 248-485 (1969)

[12] R. Rosenberg, "Value D_0Z^* for grain boundary electromigration in aluminium films" Appl. Phys. Let., **16**, pp. 27-29 (1970)

[13] E. Philofsky, K. Ravi, E. Hall, J. Black, "Surface reconstruction of aluminium metallization – a new potential wearout mechanism" IEEE: 9th Annual Proc. Reliability Physics, New York, NY, USA, pp. 120-128 (1971)

[14] D. Kim, B. Heiland, W. D. Nix, E. Arzt, M. D. Deal, J. D. Plummer, "Microstructure of thermal hillocks on blanket Al thin films" Thin Solid Films, **371,** pp. 278-282 (2000)

[15] H. Schmidt, S. Menzel, M. Weihnacht, R. Kunze, "Investigation of SAW-induced acoustomigration effects in Cu- and Al-based metallizations" IEEE: Proc. Of Ultras. Symp., Atlanta, USA, pp. 97-100 (2001)

[16] S. Menzel, H. Schmidt, M. Weihnacht, K. Wetzig, "Damaging of metallization layers by high power surface acoustic wave fields" International Workshop on Stress-Induced Phenomena in Metallization. In: S. Baker, M. A. Korhonen, E. Arzt, P. S. Ho (Eds.): Stress-Induced Phenomena in Metallization, AIP Conference Proceedings, Ithaca, USA, **612,** pp. 133-141 (2002)

[17] N. Hosaka, A. Yuhara, H. Watanabe, J. Yamada, M. Kajiyama, "A study of Al-Alloy Electrodes for High Power SAW Filters" Jpn. J. Appl. Phys., Suppl., **27-1**, pp. 175-177 (1988)

[18] N. Kimura, M. Nakano, K. Sato, "Power durability of Al-W alloy electrodes used in RF-band surface acoustic wave filters" Jpn. J. Appl. Phys., **37,** 1017-1020 (1998)

[19] N. Kimura, M. Nakano, M. Nakazawa, K. Sato, "The power durability of 900 MHz band double-mode-type surface acoustic wave filters and improvement in power durability of Al-Cu thin film electrodes by Cu atom segregation" Jpn. J. Appl. Phys., **36,** pp. 3101-3106 (1997)

[20] Y. Ota, A. Yuhara, "Study on power durability of Ti-containing Al surface acoustic wave electrodes, using interdigitated interdigital transducer filters" Jpn. J. Appl. Phys., **34,** pp. 2693-2697 (1995)

[21] A. Sakurai, H. Nakanishi, Y. Yoshino, "Epitaxially grown aluminum film on rotated Y-cut lithium niobate for high-power surface acoustic wave devices" Jpn. J. Appl. Phys., **34,** pp. 2674-2677 (1995)

[22] A. Sakurai, Y. Yoshino, H. Ieki, "Epitaxially grown aluminum film on 36 degrees - related Y-cut lithium tantalate for high-power surface acoustic wave devices" Jpn. J. Appl. Phys., **33**, pp. 3015-3017 (1994)

[23] T. Nishihara, H.Uchishiba, O. Ikata, Y. Satoh, "Improved power durability of surface acoustic wave filters for an antenna duplexers " Jpn. J. Appl. Phys., **34,** pp. 2688-2692 (1995)

[24] R. Takayama, H. Nakanishi, T. Sakuragawa, T. Kawasaki, K. Nomura, "High power durable electrodes for GHz band SAW duplexers" IEEE: Ultras. Symp. Proc., San-Juan, Puerto Rico, pp. 9-13 (2000)

[25] R. Takayama, M. Furukawa, Y. Murashima, T. Sakuragawa, N. Yuda, K. Nomura, "High power SAW filter with new Al-Sc-Cu/Ti/Al-Sc-Cu/Ti electrodes" IEEE: Ultras. Symp. Proc., Sendai, Japan, pp. 5-8 (1998)

[26] N. Kimura, M. Nakano, K. Sato, "High power-durable RF-band SAW filters using single-crystal Al/Ti electrodes grown on 64 degrees Y-X LiNbO/sub 3/ substrates" Electronics Lett., **34,** pp. 131-132 (1998)

[27] W. D. Nix, "Mechanical Properties of Thin Films" Metall. Trans. A, **20 A** pp. 2217-2245 (1989)

[28] E. Arzt, "Size effects in materials due to microstructural and dimensional constraints: a comparative review", Acta Mat. **46** pp. 5611-5626 (1998)

[29] B. Blanckenhagen, E. Arzt and P. Gumbsch, "Discrete dislocation simulation of plastic deformation in metal thin films" Acta Mat., **52** pp. 773-784 (2004)

[30] T. J. Balk, G. Dehm, E. Arzt, "Parallel glide: unexpected dislocation motion parallel to the substrate in ultrathin copper films" Acta Mat, **51** pp. 4471-4485 (2003)

[31] O. Kraft, R. Schwaiger, P. Wellner, "Fatigue in thin films: lifetime and damage formation" Mat. Sci. and Eng. A, **319-321** pp. 919-923 (2001)

[32] R. Schwaiger, "Fatigue Behaviour of Sub-Micron Silver and Copper Films" PhD Thesis, University of Stuttgart, Germany p. 80 (2001)

[33] R. Schwaiger, O. Kraft, "Size effects in the fatigue behavior of thin Ag films" Acta Mat. **51,** pp. 195-206 (2003)

[34] R. Moenig, private communication (2004)

[35] C. Laird, P. Charsley, "Ultrasonic Fatigue" in J. M. Wells (Ed.): "Ultrasonic fatigue: Proceedings of the First International Conference on Fatigue and Corrosion Fatigue Up to Ultrasonic Frequencies" Trans. of the Metall. Soc. of AIME, ISBN: 0-89520-397-9 (1982)

[36] S. E. Stanzl-Tschegg: "Ultrasonic Fatigue" in: Lütjering, G., Nowack, H. (eds.): "Proc. of 6th Int. Fatigue Congress, Fatigue ´96", 6-10 May, Berlin, Germany, pp. 1887-1898 (1996)

[37] R. J. Morrissey, D. L. McDowell, T. Nicholas, "Frequency and stress ratio effects in high cycle fatigue of Ti-6Al-4V" Int. J. of Fatigue, **21,** pp. 679-685 (1999)

[38] L. D. Roth, L. E. Willertz, T. R. Leax: "On the Fatigue of Copper up to Ultrasonic Frequencies" in J. M. Wells (Ed.) "Ultrasonic fatigue: Proceedings of the First International Conference on Fatigue and Corrosion Fatigue Up to Ultrasonic Frequencies" Trans. of the Metall. Soc. of AIME, ISBN: 0-89520-397-9, pp. 265-282 (1982)

[39] S. E. Stanzl-Tschegg, H. Mayer, "Fatigue and fatigue crack growth of aluminium alloys at very high numbers of cycles" Int. J. of Fatigue, **23,** pp. 231-237 (2001)

[40] Mayer, H., M. Papakyriacou, R. Rippan, S. E. Stanzl-Tschegg, "Influence of loading frequency on the high cycle fatigue properties of AlZnMgCu1.5 aluminium alloy" Mat. Sci. and Eng. A, **314,** pp. 48-54 (2001)

[41] Landoldt-Börnstein, "Numerical data and functional relationships in science and technology", **II 5**, pp. 236-238 (1967)

[42] G. Gremaud: "Dislocation – point defect interactions" in: R. Schaller, G. Fantozzi, G. Gremaud (Eds.), "Mechanical Spectroscopy Q^{-1} 2001" Trans Tech Publications Ltd, Switzerland, ISBN 0-87849-876-1, pp. 178-275 (2001)

[43] A. S. Nowick, B. S. Berry, "Anelastic Relaxation in Crystalline Solids" Academic Press, New York and London, ISBN 0-12-522650-0, pp. 413-414 (1972)

[44] V., K. Lücke, "Dislocation Damping in Cu at kHz- and MHz-Frequencies" Proc. of the 5th Int. Conf. on Internal Friction and Ultrasonic Attenuation in Cryst. solids. Springer-Verlag. Part II, Berlin, Germany, pp. 281- (1975)

[45] J. A. Eiras, "Influence of plastic deformation on the velocity and ultrasonic attenuation of copper single crystals" J. All. Comp., **310,** 68-71 (2000)

[46] K. Akune, M. Mondino, B Vittoz, "Internal Friction of Gold Single Crystals in the Megacycle Range" Proc. 5th Int. Conf. Int. Fric. Ultras. Atten. Cryst. Solids, Springer-Verlag. Part II, Berlin, Germany, 211-220 (1975)

[47] R. Spolenak, O. Kraft, E. Arzt, "Effects of alloying on electromigration" Microelec. Reliab., **38,** 1015-1020 (1998)

[48] I., A., Blech, "Electromigration in thin aluminum films on titanium nitride", J. Appl. Phys., **47**, pp. 1203-1208 (1976)

[49] W. Ruile, G. Raml, A. Springer, R. Weigel, "A Novel Test Device to Characterize SAW Acoustomigration" IEEE: Ultras. Symp. Proc., San Juan, Puerto Rico, pp. 275-278 (2000)

[50] I. Ames, F. M. D'Heurle, R. E. Horstmann, "Reduction of Electromigration in Aluminum Films by Copper Doping" IBM J. Res. Develop., **14,** pp. 89-91 (1970)

[51] P. G. Shewmon, "Diffusion in solids" McGraw Hill Book Company ISBN: 0-87339-105-5, p. 42 (1962)

[52] Landolt-Börnstein, "Numerical data and functional relationships in science and technology" Springer-Verlag, Berlin-Heidelberg-New York, New Series III / **26**, p. 640 (1990)

[53] K. Taki, Y. Shimizu, "Material constants of $LiTaO_3$ determined from surface acoustic wave velocities" Jpn. J. Appl. Phys., **33,** pp. 2976-2978 (1994)

[54] http://www.coretech.com.cn/LITAO3.HTM (27.7.2004)

[55] P.B. Ghate, J.C. Blaire, C.R Fuller, Thin solid films, **45,** pp. 69-84 (1977)

[56] H. Mughrabi, "The cyclic hardening and saturation behaviour of copper single crystals" Mat. Sci. and Eng., **33,** pp. 207-223 (1978)

[57] C. L. Muhlstein, R. T. Howe and R. O. Ritchie "Fatigue of polycrystalline silicon for microelectromechanical system applications: crack growth and stability under resonant loading conditions" Mech. Mat., **36,** pp. 13-33 (2004)

[58] C. L. Muhlstein, E. A. Stach and R. O. Ritchie, "A reaction-layer mechanism for the delayed failure of micron-scale polycrystalline silicon structural films subjected to high-cycle fatigue loading" Acta Mat., **50,** pp. 3579-3595 (2002)

[59] H. Kahn, R. Ballarini, A. H. Heuer, "Dynamic fatigue of silicon" Current Oponion in Solid state & Material Science *in press* (2004)

[60] T. Nishihara, H.Uchishiba, O. Ikata, Y. Satoh, "Improved Power Durability of Surface Acoustic Wave Filters for an Antenna Duplexer" Jpn. J. Appl. Phys., **34,** pp. 2688-2692 (1995)

[61] R. Spolenak, L. Sauter, C. Eberl, "Reversible orientation – biased grain growth in thin metal films induced by a focused ion beam", submitted to Phys. Rev. B (2004)

[62] A. W. Thomson, W. A. Backofen "The effect of grain size on fatigue" Acta Met., **19,** pp. 597-606 (1971)

[63] S. Suresh, "Fatigue of materials" Cambridge University Press, Sec. Ed., ISBN: 0-521-57847-7, pp. 227-228 (2001)

[64] Y. Ebata, S. Mitobe, "A Numerical Method for Stress Analysis in a SAW Resonator" IEEE: Ultras. Symp. Proc., Sendai, Japan, pp. 257-260 (1998)

[65] Z. C. Xia, J. W. Hutchinson, "Crack patterns in thin films" J. Mech. Phys. Sol., **48,** pp. 1107-1131 (2000)

[66] D. Weiss, "Deformation mechanisms in pure and alloyed copper films" PhD thesis, University of Stuttgart, pp. 95-96 (2000)

[67] N. Ramakrishnan, V.S. Arunachalam, "Effective elastic moduli of porous solids" J. Mat. Sci., **25,** pp. 3930-3937 (1990)

[68] J. C. Wang, "Young's modulus of porous materials" J. Mat. Sci., **19,** pp. 809-814 (1984)

[69] "Modal Analysis", online handbook "Ansys 7.0 documentation", provided with the software product Ansys 7.0.

[70] M. F. Ashby, "Materials selection in mechanical design - Second Edition" Butterworth Heinemann ISBN 0-7506-4357-9, pp. 398-399 (1999)

[71] G. Gottstein, "Physikalische Grundlagen in der Metallkunde" 2. Aufl. Springer-Verlag ISBN: 3-540-41961-6, p. 271 (2001)

[72] Landolt Börnstein, "Zahlenwerte und Funktionen" 6. Aufl., Bd.II/5 b , Springer-Verlag, Berlin-Heidelberg-New York, p. 19 (1968)

[73] P. G. Shewmon, "Diffusion in solids" McGraw Hill Book Company ISBN: 0-87339-105-5, pp. 172-173 (1962)

10 Deutsche Zusammenfassung:

Ermüdung in dünnen Al-Schichten bei ultra hohen Frequenzen

10.1 Motivation und Literaturüberblick

Die Untersuchung von Ermüdung in metallischen Werkstoffen hat eine lange Tradition in der Materialwissenschaft. Das Ziel dieser Forschungsrichtung ist es, die Zuverlässigkeit von Bauteilen unter zyklischer mechanischer Belastung zu verbessern. Es ist allgemein bekannt [1, 2], dass bei zyklischer Belastung schon eine wesentlich niedrigere Spannungsamplitude als die Fließspannung zum Versagen von Metallen führt. Durch die dynamische Belastung kann es zu lokalen plastischen Verformungen kommen, die beispielsweise zur Nukleierung von Rissen führen können. Die Größenskalen in denen Ermüdungserscheinungen auftreten reichen von mehreren Metern (Flugzeugflügel oder -rümpfe) bis hinab in den Bereich von unter einem Mikrometer (MEMS). Das Frequenzspektrum in dem zyklische Verformung auftritt umfasst Größenordnungen von einigen Hz bis GHz. In der vorliegenden Arbeit wurde die Ermüdung in dünnen Al-Schichten bei ultra hohen Frequenzen in Oberflächenwellen-Bauteilen (OFW; engl. Surface Acoustic Wave - SAW) untersucht.

OFW-Bauteile werden seit Mitte 80er Jahre als Frequenzfilter in Video- und TV-Produkten eingesetzt. Seit der Mitte der 90er Jahre werden sie typischerweise auch in drahtlosen Anwendungen wie in Mobiltelefonen, Bluetooth- oder drahtlosen Netz-werkadaptern verwendet. Berücksichtig man, dass im Jahr 2003 weltweit ca. 520 Mio. Mobiltelefone verkauft wurden [3], ist es offensichtlich, dass die Zuverlässigkeit dieser Bauteile heutzutage eine hohe Relevanz hat. In diesen OFW-Frequenzfiltern werden elektro-magnetische Signale in eine akustische Welle an der Oberfläche des piezoelektrischen Substrates umgewandelt [5]. Diese akustische Welle kann zu einer Schädigung in der Metallisierung führen [4], die als Elektrodenmaterial an der Oberfläche des Substrates genutzt wird. Die Schädigung in der Metallisierung wird von einer Frequenzverschiebung des Filterbauteils begleitet.

Obwohl intensive Zuverlässigkeitsprüfungen dieser Applikationen industrieller Standard sind, ist kaum etwas über die Ermüdungsmechanismen bei ultra hohen Frequenzen bekannt.

Da zukünftige Kommunikationstechnologien mehr Bandbreite und Mobilität erfordern, wird eine weitere Erhöhung der Übertragungsfrequenz und eine Abnahme der Frequenzfilter-dimensionen benötigt. Dies führt zu einer stetigen Zunahme der akustischen Energiedichte in der Metallisierung und zu einer zunehmenden Bedeutung des Wissens um die zugrunde liegenden Schädigungsmechanismen.

Die Schädigung durch Oberflächenwellen wurde zuerst von Latham et al. [4] beobachtet (Abb. 2.3 a), die nach der Belastung an der Oberfläche der Metallisierung Dendriten-ähnliche Auswüchse fanden. Neben diesen Extrusionen fanden Shibagaki et al. [10] korrespondierende Poren (Abb. 2.3 b). Die beobachtete Schädigung zeigt dabei eine starke Ähnlichkeit zu Schädigungsstrukturen, die bei Elektromigrationsexperimenten [11, 12] (Abb. 2.4) oder thermomechanischer Ermüdung [13] auftreten. Dieser Befund steht im Kontrast zu Schädigungsstrukturen an dünnen Cu- und Ag-Filmen, die bei niedrigen Frequenzen ermüdet wurden [31, 32]. Die hier gefundenen Schädigungsstrukturen zeigen plattenartige Extrusionen an der Oberfläche, die auf einen reinen Schermechanismus hindeuten (Abb. 2.6). Die mikrostrukturelle Schädigung in der Metallisierung der OFW-Bauteile führt zu messbaren Veränderungen der Filtereigenschaften. Es kommt zu irreversiblen Verschiebungen der Resonanzfrequenz der OFW-Teststrukturen [4], Kurzschlüssen durch Extrusionen [17] (Abb. 2.5) sowie zu einer Zunahme der Einfügedämpfung (Abfall der Signalamplitude zwischen Eingang und Ausgang am Bauteil) durch die abnehmende Leitfähigkeit der Metallisierung [10]. Um diesen Problemen entgegenzuwirken, werden den Al-Metallisierungen verschiedene Legierungselemente zugesetzt [18 - 20], einkristalline Schichten hergestellt [21, 22] oder Multilagenschichten angewandt [23 - 26].

Querschnitte der Metallisierung in OFW-Teststrukturen zeigen, dass die Poren meist nicht durch die ganze Metallisierung reichen und dass Tripelpunkte mögliche Nukleationsstellen für diese Extrusionen sein können [15]. Menzel et al. führen die zugrunde liegenden Prozesse die zu dieser Schädigung führen auf Korngrenzendiffusion zurück [16], eine Erklärung für diesen Schädigungsmechanismus bei ultra hohen Frequenzen kann die Literatur allerdings bisher nicht bieten. Außerdem wurde in der Literatur bisher kein Verfahren veröffentlicht, mit der die beschriebenen mikrostrukturellen Schädigungen quantitativ gemessen werden kann um sie mit den Filtereigenschaften zu korrelieren.

In der vorliegenden Arbeit wurden OFW-Teststrukturen dazu benutzt, die Ermüdung von dünnen Al-Schichten (420 nm) auf einkristallinen, piezoelektrischen $LiTaO_3$ Substraten zu untersuchen. Qualitative Untersuchungen der Schädigung sollen eine Klassifizierung der auftretenden Defekte ermöglichen und erste Hinweise auf die zugrunde liegenden

Mechanismen liefern (Kapitel 3 und 4). Anhand spezieller *in situ*-Untersuchungen in einem Rasterelektronenmikroskop (REM) wird die Schädigungsbildung untersucht (Kapitel 3). Quantitative Untersuchungen der Schädigung nach der Belastung mittels Rasterionen- (FIB), Rasterelektronen- und Rasterkraftmikroskopie konzentrieren sich auf die Korrelation zwischen der Defektdichte und der Frequenzverschiebung und Ausfallwahrscheinlichkeit der Teststrukturen (Kapitel 4). Finite Elemente (FEM) Simulationen sollen ein tieferes Verständnis für den Spannungszustand und den Einfluss der einzelnen Defekte ermöglichen (Kapitel 5). Schlussendlich soll ein qualitatives Modell präsentiert werden, welches die beobachtete Schädigungsbildung durch die akustischen Wellen erklärt (Kapitel 6).

10.2 Experimentelles

Das Prinzip von OFW-Bauteilen basiert auf der Wandlung eines hochfrequenten elektromagnetischen Signals in eine akustische Welle [5]. Dies wird erreicht indem man zwei ineinander verschränkte Elektrodenkammstrukturen (interdigital transducer - IDT; Abb. 2.1 a) auf einem piezoelektrischen, einkristallinen Substratmaterial aufbringt. Durch das Anlegen einer elektrischen Wechselspannung an den beiden Kammstrukturen induziert das elektrische Feld zwischen den Elektroden in dem darunter liegenden Piezokristall eine akustische Welle (Abb. 2.1 b). Durch den Einsatz von Reflektoren an beiden Enden des IDTs kann man einen Resonanzkörper aufbauen, in dem sich bei der entsprechenden Frequenz eine stehende Oberflächenwelle ausbilden kann. Durch diese stehende Welle an der Oberfläche des Substrats werden Spannungen in die darüber liegende Metallisierung eingetragen, die einerseits aus Massenträgheitskräften und aus der zyklischen Bewegung der Elektroden in y-Richtung resultieren und andererseits durch die wellenförmige Verzerrung des Substrats an der Grenzfläche in die Metallisierung eingeprägt werden [6, 7].

Für die Experimente wurden zwei unterschiedliche Bauformen von OFW-Testbauteilen genutzt (Abb. 2.1): 2-Tor Teststrukturen (Abb. 4.2 a) wurden für die Ermüdungsuntersuchung von kontinuierlichen dünnen Al-Schichten verwendet und L-Typ Teststrukturen (Abb. 4.2 b) für die Untersuchung an Leiterbahnstrukturen. Die Teststrukturen beider Bauformen hatten eine Resonanzfrequenz von ca. 900 MHz. Die Ermüdung der Testbauteile wurde anhand der Verschiebung dieser Resonanzfrequenz gemessen. Die Metallisierung bestand aus einer 420 nm dicken Al-Schicht und wurde durch einen Aufdampfprozess auf dem piezo-elektrischen, einkristallinen $LiTaO_3$-Substrat abgeschieden. Die Strukturierung wurde mittels

eines lithografischen Prozesses durchgeführt. Die Mikrostruktur der Al-Schicht wurde durch eine Auslagerung an Luft bei einer Temperatur von 540 K stabilisiert. Die resultierende Mikrostruktur hatte eine bevorzugte (111) out-of-plane-Orientierung und eine mittlere Korngröße welche etwas kleiner war, als die Schichtdicke.

Eine schematische Darstellung der Messapparatur ist in Abb. 3.3 zu sehen (detaillierter Messaufbau siehe [9]). Durch einen Verstärker wird das Signal eines Synthesizers verstärkt und in das Testbauteil eingespeist. Ein bidirektionaler Koppler erlaubt es, die Leistung des Signals über ein Strommessgerät während der Belastung zu messen. Zusätzlich kann über einen Netzwerkanalysator der Frequenzverlauf (transfer-function S_{12}) der OFW-Testbauteile analysiert werden. Dieser Frequenzverlauf (Abb. 3.2) wird typischerweise benutzt, um die Filtereigenschaften zu charakterisieren. Um die Frequenzverschiebung aufgrund von Temperaturänderungen oder Schädigung der Metallisierung messen zu können, wird relativ zum Maximum bei -3 oder -6 dB die Verschiebung dieser Kurve bestimmt.

Die mikrostrukturelle Schädigung wurde mittels REM, FIB und AFM untersucht. Im Fall der quantitativen Schädigungsanalyse der strukturierten Al-Schichten wurde mittels REM und FIB die projizierte Größe und die Anzahl der Extrusionen an der Seite der Elektroden gemessen. Im Falle der kontinuierlichen Schichten wurde die Anzahl der Extrusionen mittels AFM bestimmt. Die Korngrößenbestimmung wurde mithilfe eines FIB vorgenommen.

10.3 Ergebnisse und Diskussion

Die zyklische mechanische Spannung durch die Oberflächenwelle führt zu Bildung von Poren an der Korngrenze, begleitet von der Bildung von Extrusionen an der Oberfläche der Metallisierung. *In situ* Versuche haben gezeigt, dass diese Materialschädigung innerhalb von einigen hundert Sekunden stattfindet (Abb. 3.5, 3.6). Unabhängig davon, ob es sich um eine kontinuierliche (Abb. 4.3) oder eine strukturierte (Abb. 4.5) Metallisierung handelte, konnten anhand der qualitativen Schädigungsanalyse zwei verschiedene Typen von Extrusionen unterschieden werden: Zum einen fanden sich Extrusionen mit einem hohen Aspektverhältnis, bei denen Höhe und Breite signifikant kleiner waren als deren Länge. Diese Extrusionen wurden nur an Korngrenzen gefunden. Zum anderen fanden sich kornähnliche Extrusionen, die durch das Wachstum von Körnern aus der Oberfläche entstanden waren.

Die Mikrostrukturanalyse zeigte weiterhin, dass es während der Ermüdung zu einem signifikanten Kornwachstum kommt, das eine starke Korrelation zur Frequenzverschiebung

der Teststrukturen aufweist (Abb. 4.7, 4.8). Ein anfänglicher Anstieg der mittleren Korngröße geht für Frequenzverschiebungen von mehr als 1 MHz in ein Plateau über. Dies lässt sich auf die starke Porenbildung an den Korngrenzen zurückführen, die ein weiteres Wachstum der Körner verhindert. Da kein Einfluss der experimentellen Parameter wie Temperatur, eingebrachte elektrische Leistung oder Belastungsdauer auf diesen Verlauf gefunden wurde, kann man daraus folgern, dass der zugrunde liegende Mechanismus für das Kornwachstum und die Schädigungsbildung derselbe ist.

Die Poren- und Extrusionsbildung findet bevorzugt an Stellen von hohen zyklischen Spannungen statt, die durch die kurze Wellenlänge (ca. 4 μm) der stehenden Oberflächen-welle örtlich stark eingegrenzt sind. FEM-Berechnungen der strukturierten Al-Schichten zeigen, dass die höchsten zyklischen Spannungen an den unteren Kanten der Elektroden auftreten (Abb. 3.10), was mit dem Schädigungsbild (Abb. 4.5) übereinstimmt. Auch der Vergleich der Extrusionsanzahl an den einzelnen Elektroden innerhalb eines Filterbausteins zeigt aufgrund der inhomogenen Verteilung der akustischen Energie [64] die Übereinstimmung mit der Belastungsamplitude (Abb. 4.9). Zu den Reflektoren hin erzeugt die akustische Welle eine abnehmende Spannungsamplitude, während die Belastung im Inneren des IDTs einen konstanten Amplitudenverlauf hat. Während die Extrusionsanzahl mit dieser verteilung übereinstimmt ändert sich die mittlere Extrusionslänge nicht signifikant.

Die quantitative Untersuchung der Extrusionsdichte an der Oberfläche der kontinuierlichen sowie strukturierten Metallisierung hat ergeben, dass diese linear mit der Verschiebung der Resonanzfrequenz korreliert ist (Abb. 3.8, 4.11). Diese Korrelation wurde auf die Porenbildung zurückgeführt, die die Steifigkeit der Metallisierung reduziert und damit zu einer Abnahme der Oberflächenwellen-Geschwindigkeit führt. Dies hat wiederum eine Abnahme der Resonanzfrequenz der Teststruktur zur Folge. Auf diese Korrelation konnte ein Modell von Xia und Hutchinson angewandt werden, welches Spannungsrelaxation durch parallele Risse in dünnen Schichten beschreibt [65]. Für kleine Rissdichten sagt das Modell einen linearen Zusammenhang zwischen dem inversen Defektabstand und der relativen Steifigkeitsänderung der Metallisierung (Formel (4.4)) voraus. Unter der Annahme, dass die Extrusionsdichte und die Porendichte proportional zueinander sind und dass die Porendichte proportional zu dem im Modell angenommenen inversen Defektabstand ist, ergibt sich daraus ein linearer Zusammenhang zwischen der relativen Steifigkeitsänderung und der Extrusionsdichte. Da für kleine relative Frequenzverschiebungen eine direkte Korrelation zur relativen Steifigkeitsänderung besteht (Abb. 5.7), kann damit der lineare Zusammenhang zwischen der Extrusionsdichte und der Frequenzverschiebung erklärt werden. Obwohl

dadurch der generelle Zusammenhang zwischen Defektdichte und Resonanzfrequenz einer OFW-Teststruktur gezeigt werden konnte, weist der Vergleich mit experimentellen Ergebnissen signifikante Unterschiede in der Größe der Effekte auf. Dies wird auf die komplexe Geometrie und den Spannungszustand zurückgeführt.

Um ein tieferes Verständnis für den Einfluss der Poren und Extrusionen auf die Eigenfrequenz eines Elektroden-Substrat-Systems zu entwickeln, wurden detaillierte Finite-Elemente-Simulationen eingesetzt. Hierzu wurde eine Eigenfrequenzanalyse an einem Elektroden-Substrat-Modell durchgeführt, bei dem durch die Variation der Elektroden-geometrie der Einfluss der einzelnen Defekte untersucht wurde. Beim Einbringen von Rissen konnte gezeigt werden, dass die Spannung in einem Bereich von 1,5-fachen der Schichtdicke signifikant erniedrigt wird, diese allerdings nicht Null wird (Abb. 5.9). Die Änderung der Risslänge und Position in der Leiterbahn hat gezeigt, dass bei derselben Gesamtrisslänge einzelne Risse, die von der Seite der Leiterbahn in die Mitte laufen, dieselbe Frequenzverschiebung zur Folge haben, wie zwei Risse, die von entgegen gesetzten Seiten in die Leiterbahnmitte laufen (Abb. 5.10). Dagegen ist der Einfluss von Rissen, die von der Grenzfläche zum Substrat in die Leiterbahn laufen höher als der Einfluss von Rissen die von der Oberfläche aus in die Leiternbahn hineinwachsen (Abb.5.11). In der Realität finden sich allerdings keine Risse sondern Poren an den Korngrenzen der Leiterbahnen. Die Simulation von Poren als auch von Extrusionen als einzelne Defekte erzeugen in dem FEM Modell auch immer eine Massenzu- oder -abnahme, was im realen System nie der Fall ist, da sich hier das Volumen der Poren und Extrusionen ausgleicht. Daher kann man diese beiden Fälle mit dem hypothetischen Fall der Dichteänderung der Metallisierung vergleichen. Hier zeigt sich, dass der Einfluss der Extrusionen meist weniger signifikant ist als der Einfluss der Poren. Dies resultiert aus der Tatsache, dass mit dem Einbringen einer Pore neben der Massenabnahme der Leiterbahn auch gleichzeitig die Steifigkeit der Schicht wie im Fall eines Risses abnimmt (Abb. 5.12). Allerdings gilt ebenfalls wie in den noch folgenden Fällen, dass die Geometrie und Position der Extrusionen einen entscheidenden Einfluss auf die Eigenfrequenz des untersuchten FEM-Modells haben. Die Variation der Extrusionslänge zeigt, dass der Einfluss der Extrusionen stark variiert, da die Extrusionen bei bestimmten Längen in Eigenresonanz geraten und damit einen sehr starken Einfluss auf das Gesamtmodell haben (Abb. 5.13). Der Einfluss der Extrusionen auf die Eigenfrequenz des FEM Modells kann dann sowohl eine positive als auch negative Verschiebung erzeugen. Die Variation der Fixierungshöhe der Extrusion an der Seitenwand der Leiterbahn hat ergeben, dass mit zunehmender Fixierungshöhe der Einfluss der Extrusion auf die Eigenfrequenz des Modells stark zunimmt

(Abb. 5.14). Dies resultiert aus dem Grund, dass die Extrusion einen umso weiteren Weg zurücklegen muss je weiter oben sie an der Leiterbahn befestigt ist, da die Auslenkung der Leiterbahn mit der Höhe zunimmt. Um nun einen Vergleich der FE Simulation mit experimentellen Werten zu ermöglichen, wurde die Frequenzverschiebung der verschiedenen Defekte (Riss, Pore, Pore + Extrusion mit hohem Aspektverhältnis, Pore + kornähnliche Extrusion) gegen deren inversen Defektabstand, die äquivalent zur Defektdichte ist, abgetragen (Abb. 5.15). In allen Fällen zeigt sich für geringe Defektdichten eine lineare Korrelation. Vergleicht man die Wirkung der einzelnen Fälle miteinander, so zeigt sich, dass die stärkste Verschiebung der relativen Eigenfrequenz im Falle der Kombination einer Pore mit kornähnlichen Extrusionen auftritt. Die Verlagerung der Masse von der Mitte der Leiterbahn nach außen in die Extrusionen führt verglichen mit einem einfachen Riss zu einer zusätzlichen Frequenzverschiebung was sich mit den Simulationen der Extrusionslängen-änderung deckt. Bei sehr kleinen Aspektverhältnissen der Extrusionslänge zur Extrusionsbreite und -höhe erzeugen Extrusionen eine negative Frequenzverschiebung. Die geringste Frequenzverschiebung findet sich im Fall der Kombination einer Pore mit Extrusionen mit hohem Aspektverhältnis. Auch hier gilt, dass die Geometrie der Extrusion eine kritische Einflussgröße hat. Die gewählten Extrusionen haben dabei nur eine geringe negative Frequenzverschiebung zur Folge, die den Einfluss der Pore nur leicht abschwächt. Diese erzeugt zwar dieselbe Steifigkeitsabnahme wie sie im Fall eines Risses auftritt, was allerdings durch die Massenabnahme der Elektrode überdeckt wird. Dadurch erzeugt eine Pore in dem untersuchten FEM-Modell eine positive Frequenzverschiebung. In allen Simulationen kann man auch eine Abweichung von der linearen Abhängigkeit der Frequenzverschiebung für höhere Defektdichten feststellen. Dies resultiert aus der Überlagerung des Einflusses benachbarter Schädigungen. Ein Vergleich der FEM-Simulationen mit den experimentellen Daten (Kapitel 4) zeigt, dass die Frequenzverschiebung in einem vergleichbaren Bereich liegen. Auch wenn in den realen Bauteilen nicht nur Extrusionen mit einer Länge sondern mit einer Verteilung von unterschiedlichen Längen und Aspektverhältnissen auftreten, zeigt dieser Vergleich sehr deutlich, dass die simulierten Systeme eine gute Übereinstimmung liefern. Außerdem hat sich gezeigt, dass neben der Steifigkeitsabnahme durch die Porenbildung auch die Verschiebung des Schwerpunkts durch den Massentransport in den geschädigten Elektroden einen signifikanten Einfluss auf die Eigenfrequenz der Elektroden hat.

Lebensdaueruntersuchungen bei ultra hohen Frequenzen haben ergeben, dass die dünnen Al-Schichten bei Spannungsamplituden von nur 14 MPa das Ausfallkriterium erst nach 10^{14}

Zyklen erreichen. Dabei wurde bei den Al-Schichten kein Ermüdungslimit gefunden, wie man es von einem kfz-Material erwartet (Tab. 4.1). Ein Vergleich mit dünnen Kupferschichten bei sehr viel höheren Spannungsamplituden hat gezeigt, dass die gefundenen Lebensdauern bei einer Extrapolation über ca. 10^6 Zyklen im erwarteten Bereich liegen.

Neben der Verschiebung der Resonanzfrequenz führt die Schädigungsbildung auch zu Kurzschlüssen in OFW-Teststrukturen, da sehr lange Extrusionen die Distanz zwischen benachbarten Elektronen überbrücken können. Eine Analyse der Extrusionslängenverteilung hat gezeigt, dass es sich dabei um eine Log-Normalverteilung handelt (Abb. 4.12). Extrapoliert man diese Verteilung zu höheren Extrusionslängen, kann man die Wahrscheinlichkeit bestimmen, bei der eine Extrusion den Abstand zwischen den Elektroden überbrücken kann (Tab. 4.2). Unter der Annahme, dass die Länge einer Extrusion unabhängig vom Rest der Extrusionen ist, kann man damit die Kurzschlusswahrscheinlichkeit in einem Bauteil berechnen (Formel 4.9).

Basierend auf den experimentellen Ergebnissen und den Berechnung des Spannungszustandes mittels FEM-Simulationen wurde ein Modell entwickelt, das die gefundene Schädigungsstruktur in Form von Poren und Extrusionen an den Korngrenzen erklärt. Es wird angenommen, dass die zyklische Spannung durch die Oberflächenwelle dazu führt, dass die Versetzungen mit der Resonanzfrequenz der OFW-Struktur schwingen. Aufgrund des Gradienten der Spannungsamplitude (Abb. 6.1 b) ist die Schwingungsamplitude der Versetzungen auf Gleitebenen, die zur Substratoberfläche verkippt sind (Abb. 6.1 a), unterschiedlich. Dies führt dazu, dass sich die Versetzungen schrittweise in eine Richtung bewegen (Abb. 6.1 c). Dadurch können sich einzelne Körner aufeinander zu- oder wegbewegen, was Druck- und Zugspannungen an den Korngrenzen induziert (Abb. 6.2). Eine genauere Betrachtung der mikrostrukturellen Änderungen zeigt, dass es zur Verschiebung und Rotation der Körner relativ zueinander kommt (Abb. 3.11). Es wird angenommen, dass diese Verschiebungen zu Druck- und Zugspannungen an den Korngrenzen führen. Diese Spannungen können durch Kletterprozesse von Versetzungen an den Korngrenzen relaxieren, was die Bildung von Extrusionen und Poren zur Folge hat. Eine Abschätzung des Materialflusses durch Kletterprozesse zeigt eine gute Übereinstimmung der möglichen Extrusionswachstumsgeschwindigkeit mit der experimentell beobachteten.